UNDERSTANDING STAR FORMATION AT EARLY STAGES IN THE FILAMENTARY ERA

BY

I-JEN LEE

DISSERTATION

Submitted in partial fulfillment of the requirements
for the degree of Doctor of Philosophy in Astronomy
in the Graduate College of the
University of Illinois at Urbana-Champaign, 2013

Urbana, Illinois

Doctoral Committee:

Associate Professor Leslie Looney, Chair
Professor Emeritus Richard Crutcher
Professor Telemachos Mouschovias
Associate Professor Tony Wong

Abstract

This thesis presents a study of star formation at early stages in the filamentary era with a special focus on massive star and cluster formation. We first investigate the importance of filamentary structures in star formation and propose an observationally driven scenario for the evolution of filamentary structures from large-scale molecular clouds to small-scale circumstellar envelopes. In addition, as theories of star formation have gradually shifted from individual, isolated objects to the formation of clusters over the decade, we study the environment in the protocluster IRAS 05345+3157 to better understand the initial conditions for cluster formation. With CS(2-1) observations using the Combined Array for Research in Millimeter-wave Astronomy (CARMA) observatory, we have identified seven dense gas cores in this region and discussed the role of initial turbulence. The gas cores require an external pressure of 10^8 K cm^{-3} to be bound to form possible seeds for future protostars.

Furthermore, to understand massive star formation, we study the structure and kinematics of nine starless cores in Orion. As two main models about massive star formation, the turbulent core model and the competitive accretion model, predict different level of fragmentation in massive starless cores, our results from high angular resolution observations with CS(2-1) using CARMA show three to five fragments associated with each core, in a broad consistency with the models involving turbulent fragmentation. The number of fragments suggest that magnetic fields may be playing a role in suppressing the fragmentation. Also, the spectral data from the IRAM CS(2-1) observations of several cores show consistency with a picture of converging flows along a filament toward the core center; these flows may be important in massive and cluster formation. Our result does not fully support either the turbulent core scenario or the competitive accretion scenario.

Finally, we present the first results from the CARMA Large Area Star Formation Survey (CLASSy) toward Serpens Main, NGC 1333, and Barnard 1. The project provides an unique

opportunity to study cold, dense gas structure at millimeter wavelengths from 1500 AU to a few parsecs. The data reveal some exciting properties in morphological and kinematic structures for the first time, and will be unveiling more underlying physics in the star formation process in the future.

To My Father and Mother.

Acknowledgments

I would like to express my greatest gratitute to my advisor Professor Leslie Looney. I thank Leslie for his restless discussions and insightful comments about science, useful and pleasant conversations, and numerous revisions on my proposals and papers. I thank Leslie for accepting me as his student, for helping making some sense of the confusion, and for allowing me to learn and grow at my own pace. I thank him for always responding quickly to paper drafts and emails even when he is in sabbatical. I thank him for being such a kind and honest person, so that I truely know when I have done a good or bad job. Finally, I thank him for his hospitality and generosity in preparing the yearly abundant dinner on Thanksgiving, and also to allow me to stay with his family when I visited NRAO, Charlottesville. The support and help I received from Leslie are beyond words, and are deeply appreciated.

I would like to thank my thesis committee members, Professor Richard Crutcher, Professor Telemachos Mouschovias, and Professor Tony Wong, who offered guidance and support to this thesis. I appreciate their valuable comments and feedback throughout the years. I would also like to thank Professor You-Hua Chu, who admitted me to the graduate school which made this thesis possible.

This thesis would not have been possible without the support of my collaborators. I would like to thank Doug Johnstone for turning an original scientific idea established in a conference to a research topic, which later became an enjoyable collaboration, and for all the theoretical insights from him throughout the collaboration. I would like to thank John Tobin, who always provides valuable comments and insights to all the projects/proposals we collaborate together. Thanks to John for always being a sounding board to my ideas and questions. I would like to thank Zhi-Yun Li, for useful discussions about turbulence and massive star formation, and for shaping up some of the paper drafts. Finally, many thanks to Randolf Klein, Scott Schnee, and Shiya Wang, for the

great support and help they offered to improve this thesis.

I would to thank the LAI group at Illinois, who equipped me with the knowledge of interferometry. In particular, many thanks to Woojin Kwon, David Rebolledo, and Manuel Fernandez-Lopez, who are always willing to discuss and offering help when I have immediate research questions or confusions. I would like to thank CARMA for financial support. I would like to thank several people who have inspired me in different aspects about being a scientist along the way: Jin Koda, Fumi Egusa, Josh Dolence, Jonathan Seale, and Shiya Wang.

I would not have accomplished this thesis without the love and support from dear family and friends. I would like to thank the friends from the Class 2007: Hotaka Shiokawa, David Rebolledo, Kuo-Chuan Pan, Nachiketa Chakraborty, and Yiran Wang, for being such terrific friends, for all the fun time and encouragements, and for being all together in ups and downs. I would like to thank Hsiang-Yi Yang, Amy Lien, Nick Indriolo, Rosie Chen, Ian Stephens, Nick Hakobian, Brett Hayes, and Hsin-Fang Chiang, for lighting up my days, and for their wonderful friendship. Also, I would like to thank Hsin-Yen Wang, Birdy Fong, Tito Tang, Pash Yang, and Tzu-Jung Lin, who care about me from the bottom of their hearts, and who are always there for me.

Finally, I would like to thank my family, to whom this thesis is dedicated to. To my father, who educated me to pursue my own dreams and encouraged me to become who I want to be. To my mother, whose understanding and listening have been my strength to study abroad. To my grandmothers, whose encouragements always deeply warm my heart. To my siblings, for numerous fun conversations which release my stress. Finally, to my dear husband, Hotaka Shiokawa, for being such a wonderful person in the world who inspires me in every way, and for being my best friend in my life. Thank you for being never reluctant to show love and support, tenderness and kindness, encouragements and patience. Thank you for always being beside me through the years in happiness and difficulties, and for loving me as I am.

And I thank God, for all of the above.

Table of Contents

List of Tables

List of Figures

Chapter 1

Introduction

Stars are ubiquitous and important in the Universe. Stellar radiation is the dominating source in galaxies which determines the luminosity of galaxies. By turning interstellar gas and dust into stellar material, the formation process of stars shapes the structures of the interstellar medium and affects galaxy evolution. Also, through nuclear fusion, the necessary elements to form life and habitable environments are produced in stars. Finally, stellar systems and their formation have profound impacts on the formation of planetary systems.

As stars play such a key role in astronomical systems, understanding star formation is crucial. A rough division in the studies of star formation contains two main conceptual categories: low mass vs. massive stars and isolated vs. clusters. Low-mass stars have masses below ~ 3 $M_\odot$, and massive stars have masses larger than 8 $M_\odot$. The formation of massive stars, however, has fundamental differences from that of low-mass stars. For example, massive stars tend to be discovered in clusters (Lada & Lada, 2003), in contrary to low-mass stars often found in isolation (Evans, 1999). One of the classic examples for massive stars in clusters is the Orion Nebula Cluster (ONC), which contains four OB stars in the Trapezium system and a total of 3600 stars (Hillenbrand, 1997). Moreover, a standard scenario for low-mass star formation featuring Class 0/I/II/III phases has been established over decades (see review by Evans, 1999), and whether massive star formation is a scaled-up version of low-mass star formation or it involves other dynamical processes is still an issue under debate. In particular, one of the major problems in massive star formation is the radiation pressure in the accretion phase for stars with masses > 20 $M_\odot$, in which the stronger radiation from accretion hinders further accretion process (Jijina & Adams, 1996; Yorke & Sonnhalter, 2002). The solution to this problem includes large accretion rates (McKee & Tan, 2003) and/or accretion via disks (Krumholz et al., 2005a).

This thesis mainly focuses on the formation of massive stars and clustered environments at very

early stages. Millimeter wavelengths are the best suited for such stages since it probes emission from cold gas and dust. In particular, this thesis discusses the implications of filamentary structures on star formation, as a changing paradigm in star formation from spherical to filamentary is forming.

1.1 Early Stages of Massive Star and Protocluster Formation

1.1.1 Observational Results

Massive stars play an important role in several astrophysical areas. By injecting enormous energy into the ambient environment, massive outflows and stellar winds generated during their formation shape galactic structures and provide stellar feedback into interstellar medium (e.g., Zinnecker & Yorke, 2007). By exploding from core collapse, supernovae leave behind neutron stars or black holes, key astronomical sources in cosmology and high-energy astrophysics. Moreover, heavy metals produced in massive stars affect the metallicity in ISM and have further influences on galaxy evolution and the stellar population.

Although massive stars are important, there have been two main difficulties in observing them. One of them is that massive stars are rare. The standard stellar initial mass function (IMF) from Kroupa (2001) shows a three-part power-law: $dN_*/d\ln m_* \propto m^{-\alpha}$ with $\alpha = 1.3$ for $0.5 < m_*/M_\odot < 50$, $\alpha = 0.3$ for $0.08 < m_*/M_\odot < 0.5$, and $\alpha = -0.7$ for $0.01 < m_*/M_\odot < 0.08$. The IMF implies that the number of low-mass stars is significantly larger than that of massive stars. Indeed, only one massive star with 64-128 $M_\odot$ would be found in a group of 975 stars with 0.5-2 $M_\odot$ based on the logarithmic relation. The other main difficulty is the that most of the massive star-forming regions are distant ($\sim$ few kpc away). The large distances imply high extinction from dust which make identification of massive star-forming regions challenging.

Despite these difficulties, observations toward massive star-forming regions have progressed using infrared and millimeter-wavelength instruments. A conceptual sequence proposed for the evolution of massive stars (Beuther et al., 2007a) is: High-Mass Starless Cores (HMSCs) $\rightarrow$ High-Mass Cores harboring/accreting Low/Intermediate-Mass Protostars $\rightarrow$ High-Mass Protostellar Objects (HMPOs) $\rightarrow$ Final Stars. In the last decade, observations of massive star formation have been extensively carried out toward High-Mass Protostellar Objects (HMPOs) including hypercompact and ultracompact HII regions (e.g., Churchwell et al., 1990; Cesaroni et al., 1991; Henning et al.,

1992; Hunter et al., 1997; Hatchell et al., 1998; Beuther et al., 2002; Garay et al., 2003; Zhang et al., 2005; Seale et al., 2009; Urquhart et al., 2011). These objects have re-processed the UV radiation from central embedded sources and re-emitted from envelopes at infrared to far-infrared wavelengths; therefore, many of the identifications toward HMPOs benefit from infrared observations such as the IRAS all sky survey. HMPOs are characterized to be small (sizes < 0.1 pc), dense ($> 10^6$ cm^{-3}), bright ($> 10^4$ L$_\odot$), and warm (> 100 K) (Cesaroni et al., 1994; Sridharan et al., 2002; Molinari et al., 1998). Several protoclusters are identified also using infrared sources as the lighthouse and following up with millimeter instruments (e.g., Hunter et al., 2004; Klein et al., 2005; Wang et al., 2010).

Infrared Dark Clouds identified with Spitzer/GLIMPSE (Benjamin et al., 2003; Fazio et al., 2004) provided the opportunity to probe the earliest stages toward massive clumps that contain HMSCs prior to the formation of embedded heating sources. Simon et al. (2006) presented a catalog of $\sim$ 10000 IRDCs identified using 8.3 μm images with the Midcourse Space Experiment satellite in the 5 kpc galactic molecular ring. The IRDCs are seen in absorption against the background emission at mid-IR. These sources are expected to consist of cold dust and gas emitting at (sub)mm wavelengths and are IR-quiet as they have not heated the surrounding envelopes yet. Studies of IRDCs at submillimeter and millimeter wavelengths showed that they are massive (a few 100 M$_\odot$ to a few 1000 M$_\odot$), cold ($<$25 K), dense ($> 10^5$ cm^{-3}), and have high column densities ($\sim 10^{23} - 10^{25}$ cm^{-2}) and sizes < 0.5 pc (Carey et al., 1998, 2000; Garay et al., 2004; Schneider et al., 2010). The IRDCs are suggested to be at the onset of massive star formation and the precursors of protoclusters (e.g., Rathborne et al., 2006).

Recent high-angular resolution observations using interferometers toward IRDCs have been carried out to study the structures in detail (Swift, 2009; Zhang et al., 2009; Bontemps et al., 2010; Pillai et al., 2011; Wang et al., 2011; Palau et al., 2013). In particular, Bontemps et al. (2010) observed six most massive, IR-quiet dense cores in Cygnus-X using PdBI and found a total of 23 fragments associated with these cores. Indeed, all of these observations with high angular resolution suggested fragmentation inside massive clumps. No signs for the existence of HMSCs have been observationally claimed.

1.1.2 Theory

Molecular clouds, especially giant molecular clouds ($\sim 20-100$ pc in size, 10^4-10^6 $M_\odot$ in mass, 10 - 15 K in temperature), are the birth places of massive clumps and cores. With the low temperature and high density, the masses are estimated to be an order of magnitude larger than the Jeans mass if only thermal pressure counteracts gravity, and they should be collapsing and forming stars efficiently, which is not the case. Mechanisms other than thermal pressure must exist to support molecular clouds and regulate star formation. Magnetic fields (Mouschovias & Spitzer, 1976; Basu & Mouschovias, 1995) and turbulence (see review by Mac Low & Klessen, 2004) are suggested to play such a role, and are extensively observed in molecular clouds (Larson, 1981; Crutcher, 2012).

As star formation is a complicated interplay between magnetic fields, turbulence, and gravity, two main theoretical views toward the formation and evolution of molecular clouds and that of massive stars have been proposed: the quasi-static view and the dynamical view. In the quasi-static view, molecular clouds are in quasi-static equilibrium and they evolve on several free-fall timescales (Blitz & Shu, 1980). The formation of massive stars is also a process in quasi-static equilibrium proposed in the "turbulent core model" (McKee & Tan, 2003), as the core is supported by turbulence. High accretion rates are achieved in this model as a result of a high level of turbulent support, and turbulence needs to be replenished frequently to maintain the equilibrium. The model essentially describes the formation of massive stars as "monolithic collapse" which resembles low-mass star formation. The model predicts the existence of massive starless cores with a low level of fragmentation.

Alternatively, the dynamical view suggests that molecular clouds are quickly evolving entities; they are transient features and they are less likely to reach an equilibrium state (Ballesteros-Paredes et al., 1999; Elmegreen, 2000). At large scales, turbulent converging flows create filamentary structures via shock dissipation (e.g., Padoan et al., 2001); at small scales, density fluctuations are generated at the stagnation of flows due to turbulent fragmentation (Padoan & Nordlund, 2002). These density fluctuations are further taken over by gravity and collapse into Jeans mass objects (Jappsen et al., 2005). The formation of massive stars is approached by the "competitive accretion model" (Bonnell et al., 2004; Bonnell & Bate, 2006) with the stars sitting in the center of the potential well accreting more gas and becoming massive. The formation process is tightly linked

with the dynamics of the environment. The formation of clusters is also naturally explained by this competitive accretion model. The model predicts a high level of fragmentation in massive cores (e.g., Dobbs et al., 2005).

1.2 Star Formation in the Filamentary Era

Filamentary structures are ubiquitous and have been long observed in star-forming complexes (e.g., Hatchell et al., 2005; Gutermuth et al., 2008; Lombardi et al., 2006; Enoch et al., 2007; Myers, 2009). For example, the Orion-A region is associated with the Integral-Shaped filament that spans a spatial region of $\sim$ 6 pc (e.g., Johnstone & Bally, 1999; Nutter & Ward-Thompson, 2007). Also, the Taurus molecular cloud consists of several filamentary structures (e.g., Kenyon et al., 2008). With the Herschel Space Telescope revealing striking filamentary structures in molecular clouds (André et al., 2010; Arzoumanian et al., 2011; Hill et al., 2011), the importance of filamentary structures in star formation is even more emphasized. Moreover, several recent observational studies identified star-forming flows along filaments (Hacar & Tafalla, 2011; Kirk et al., 2013), demonstrating the kinematic role of filamentary structures in star formation.

Indeed, a changing paradigm in star formation from spherical collapse to filamentary is forming. Over the decades, sphericity has been assumed in the standard "inside-out collapse model" proposed by Shu (1977) in star formation. However, Tobin et al. (2010) unveiled complex, filamentary structures in the circumstellar envelopes of 22 Class 0 sources seen in the Spitzer 8 μm absorption images. These structures challenge the standard view of star formation that assumes sphericity.

Theoretically, the formation of large-scale filamentary structures in molecular clouds has been extensively discussed and the main drive for such structures appear to be supersonic turbulence (see review by Mac Low & Klessen, 2004; Hennebelle & Falgarone, 2012). However, the effects of filamentary structures at $<$ 0.1 pc scale in the collapsing phase are both theoretically and observationally less understood (Smith et al., 2011, 2012).

1.3 Outline of the Thesis

In this thesis, I aim for addressing these main questions:

- What are the initial conditions for protocluster formation?
- What is the mechanism for massive star formation (the turbulent core model vs. competitive accretion model)?
- What is the role of filamentary structures in the prestellar phase of massive star/protocluster formation?

In Chapter 2, we propose an evolutionary sequence focusing on filamentary structures and address the gap between large and small scale structures. In Chapter 3, we present the study toward the intermediate to massive star-forming region I05345+3157 to investigate initial conditions for protocluster formation. In Chapter 4, we present the fragmentation and kinematics of nine starless cores in Orion. The study of fragmentation provides insight to discern between the two main theories for massive star formation, and the study of kinematics addresses the role of filamentary structures in massive star/protocluster formation. In Chapter 5, we present the observations from the CARMA Large Area Star-forming Survey. These data provides an unique opportunity to study the star formation process from few thousand AUs to few parsecs.

Chapter 2

Filamentary Star Formation: Observing the Evolution toward Flattened Envelopes

This chapter is published in Lee et al. (2012)[1].

2.1 Introduction

It is becoming clear that filamentary structures (few parsecs to 10 parsecs in length and typically 0.1 pc in width) in molecular clouds are common and need to be understood. One clear example is the Integral-Shaped Filament region in the north of Orion-A, comprising OMC 1-4, where prestellar cores and protostars are forming (e.g., Chini et al., 1997; Johnstone & Bally, 1999; Aso et al., 2000; Nutter & Ward-Thompson, 2007; Ikeda et al., 2007; Takahashi et al., 2008). Taurus also consists of several large filaments, each with ongoing star-forming activity (e.g., Mizuno et al., 1995; Onishi et al., 1998; Kenyon et al., 2008). The large-scale filaments are even more evident in recent observations from the *Herschel Space Observatory* (e.g., André et al., 2010; Men'shchikov et al., 2010; Arzoumanian et al., 2011; Hill et al., 2011), and these observations further suggest a tight connection between the formation of dense cores and gravitationally unstable filaments. While the mechanisms for forming these filamentary structures are still under debate (e.g., Mac Low & Klessen, 2004; Heitsch et al., 2008; Nakamura & Li, 2008; Myers, 2009, 2011; Pon et al., 2011), an observationally derived process has been suggested: first, the filamentary structures at large scales form, possibly as a result of magnetic-hydrodynamic (MHD) turbulence in the ISM, and secondly, the prestellar cores form from the fragments of a subset of filaments through gravitational instability.

As the role of large-scale filaments in molecular clouds has received significant attention, a number of the latest observations have unveiled filamentary structure at smaller scales ($\sim$ few tenths

[1]This chapter is previously published in *The Astrophysical Journal* as "Filamentary Star Formation: Observing the Evolution toward Flattened Envelopes", Lee, Katherine, Looney, Leslie, Johnstone, Doug, Tobin, John, 2012, ApJ, 761, 171 and is reproduced here with permission of the American Astronomical Society.

of parsecs in length and 100ths of parsecs in width). For instance, Hacar & Tafalla (2011) have observed four subsonic, velocity-coherent filaments in L1517 ($\simeq$0.5 pc in length) that are possibly condensed out from the more turbulent natal cloud and lead to the quasi-static fragmentation of cores. In addition, Pineda et al. (2011) probed the Barnard-5 star-forming core with high angular resolution and discovered filamentary structures with $\sim$ 0.1 parsecs in length. The filaments in Barnard-5 are possibly the result of fragmentation in a coherent region where subsonic motions dominate, and are likely to form stars via future gravitational collapse.

In addition to the filamentary structures in molecular clouds at the early stage of star formation, typical length of few parsecs and width of 0.1 pc, small-scale filamentary structures, typical length of few thousand AU to 0.1 pc and width of few hundred to few thousand AU, have also been observed in the envelopes around Class 0 protostars (Tobin et al., 2010). These filamentary structures in the protostellar envelopes are mostly irregular and non-axisymmetric in morphology, suggesting the initial non-equilibrium from the prestellar stage. The filamentary structure presented near the Class 0 source is reminiscent of the large *Herschel* observed structures, although the size scales of the two are distinct and the properties are presumably different.

The relationship between the large-scale filaments in molecular clouds and small filamentary envelopes around young protostars still requires further investigation. Several numerical simulations have shown that large-scale filaments in molecular clouds are prone to fragmentation leading to prestellar cores (e.g., Inutsuka & Miyama, 1997; Hartmann, 2002), and filaments are possibly the most favorable mode for fragmentation (Pon et al., 2011, 2012). Moreover, studies have also demonstrated that filamentary geometries at large scales have a significant impact on the geometries and symmetries of the subsequently collapsing cores (Smith et al., 2011).

These observations and numerical simulations deliver a clear message: filamentary structures from large to small scales are clearly playing an important role to the star formation process. In this paper, we suggest an observational evolution between filaments at the large scale and filaments on the small scale. The proposed scenario suggests that the small-scale filamentary structure (few thousand AU) in protostellar envelopes originate from the filamentary structure (0.1 pc) embedded in the larger envelopes of starless cores instead of being produced by the protostellar collapse. We will further show why the filamentary structures in starless cores have not been observed to date.

2.2 Evolution of Protostellar Structure

It has been well known that dust emission maps of Class 0 sources show very spherical emission (e.g., Looney et al., 2000; Shirley et al., 2000; Motte & André, 2001). Although molecular surveys of dense cores showed non-spherical structures (e.g., Myers et al., 1991), these non-symmetric structures were often considered to be material not directly involved in the star formation process, i.e. part of the larger-scale molecular cloud or clump, so these components were rarely used in the observational modeling of these sources. Instead many authors assumed that the spherical dust emission indicated spherical collapse (e.g., Shu, 1977; Terebey et al., 1984) and used this symmetry to derive envelope properties and place constraints on any embedded disk components (e.g. Keene & Masson, 1990; Looney et al., 2003a; Harvey et al., 2003; Jørgensen et al., 2009). However, recent studies have shown the envelope structures to be more complex.

2.2.1 Changing the Paradigm for the Inner Envelope of Class 0 Protostars

The ability to use 8 μm absorption against PAH emission background allows the decoupling of the dust density and temperature for the first time in Class 0 sources (e.g., Looney et al., 2007; Tobin et al., 2010). With these measurements, it was realized that the dense portions of the envelope are complex, filamentary, and often non-axisymmetric structures ($\sim$ 1000 AU to 0.1 pc). Figure 2.1 illustrates the diversity of structures seen in the Tobin sample. IRAS 16253-2429 is what one would expect to see in a spherical envelope case. The 8 μm absorption is not a good tracer at the central source or in the outflow cavity, since in both cases there is emission in addition to the background. In stark contrast, L673 is a clear example of the main point of Tobin et al. (2010), which is that flattened, filamentary, and non-axisymmetric envelopes are the typical envelope structure.

How does this result reconcile with interferometric dust emission observations which show spherical emission in these sources (e.g., Looney et al., 2000)? It is important to remember that dust emission depends on both dust density and temperature. With flattened or non-axisymmetric envelopes and/or outflow cavities in young sources, the heating will be inhomogeneous; the lower density material near the central source is heated more, leading to temperature and density gradients, and the dust emission will appear more spherical even if the dust distribution is not. A good example, shown in Figure 2.2 from Chiang et al. (2010), is the source L1157. Although there

is a flattened and filamentary envelope detected in both N_2H^+ and the 8 μm absorption (also seen in Figure 2.6), the dust emission is very spherical and typical of a Class 0 protostar. Chiang et al. (2012) constructed a model that has a flattened geometry similar to the N_2H^+ and 8 μm absorption features and yet still predicts the observed spherical dust continuum when non-spherical, self-consistent temperature solutions are used.

However, with enough sensitivity the filamentary structures can still be seen in dust emission. Figure 2.3 is the dust emission toward L1157 with the Submillimeter Array (SMA) at $\lambda = 1.3$ mm (Tobin et al. 2012, in prep). In this case, they detected the extension along the flattened envelope and even an extension along the outflow (also see Stephens et al. 2012, in prep). The extension along the outflow illustrates how the heating is facilitated by lower density material (in this case in the outflow cavity). In other words, the heating in these sources are not uniform, which can lead to a distortion in the structure suggested by only the dust continuum.

Indeed, when comparing the observations of L673 and L1157 with the traditional view of spherical star formation, we need to change the cartoons of star formation. Figure 2.4 demonstrates our suggestion of moving from spherical star formation structures to filamentary star formation structures in Class 0 protostars to be more consistent with observations. The left panel presents the traditional model assuming sphericity that has impacted our theoretical understanding for decades. In this model, protostellar collapse is axisymmetric and spherical based on a singular isothermal sphere (Shu, 1977), With the inclusion of rotation (Terebey et al., 1984), the density structure is slightly flattened and mostly remains spherical beyond the centrifugal radius. On the other hand, the right panel in Figure 2.4 shows the axisymmetric and filamentary envelopes that are often seen in our Class 0 observations (e.g., Tobin et al., 2010). The filamentary envelopes with higher density are forming inside the ambient cloud at lower density.

The change from spherical view of star formation to filamentary view certainly has important consequences, as several analysis techniques are based on the assumption of sphericity. For example, for a single beam measurement of the region the spherical assumption will significantly underestimate the mean density of the dense material. Alternatively, low sensitivity interferometric maps will concentrate on the peak and likely miss the large structure and thus the shape. In addition, blue-skewed spectra have been extensively observed with optically thick molecular lines in starless cores. The interpretation of the blue asymmetry, together with optically thin lines peaking in the

absorption dip, has been spherical collapse. Moreover, the modeling of spectral energy distributions (SEDs) (e.g., Whitney et al., 2003; Robitaille et al., 2006) extensively used in Class 0 and Class I sources is based on spherical/axisymmetric models. As non-spherical envelopes are more common, spherical models may not provide accurate descriptions of protostellar properties, so extra caution needs to be applied.

2.2.2 Observationally-Driven Scenario for Filamentary Collapse

Filamentary structures appear to be ubiquitous from large molecular clouds to small scale circumstellar envelopes. These filamentary structures are also observed to be tightly connected to the star formation process, as prestellar cores and young protostars are located within these filaments. From these observations, we propose an observationally derived scenario of filamentary collapse in star formation that is summarized in Figure 2.5. As shown in the cartoon, there are approximately five steps in our observational-based picture of the filamentary collapse process. Among the five steps, Step I, II, IV and V are from observations, and Step III is a prediction of high-density filamentary structures in starless cores, to connect Step II and IV.

In Step I, molecular clouds are formed as filaments with a few parsecs to 10 parsecs in length and a characteristic width of 0.1 pc (Schneider & Elmegreen, 1979; Bally et al., 1987; Johnstone & Bally, 1999; André et al., 2010). These large-scale filaments are probably turbulent and prone to fragmentation, leading to subsequent velocity-coherent, higher density filaments (few tenths of parsecs in length) that are considered as the birthplaces of prestellar cores (Inutsuka & Miyama, 1997; Hartmann, 2002; Pon et al., 2011). In Step II, the fragmented filaments collapse along the long and short axis while feeding material along the filament (e.g., Hacar & Tafalla, 2011), enhancing the mass in a location and forming a higher density oblate (or prolate) starless core as observed with single-dish observations (Curry, 2002; Jones & Basu, 2002; Tassis, 2007; Tassis et al., 2009). The core formation may be related to the flows from large-scale motions along the larger filaments and is kinematically coupled with the parental cloud (Hacar & Tafalla, 2011). This would form a higher density filamentary structure embedded inside of the starless core as seen in Step III. This substructure is the kinematic descendant of the flow along the larger filament and the origin of the filamentary envelopes seen in the Class 0 objects. As the collapse continues in Step IV, material infalls along the smaller filament (Tobin et al., 2012b) and the oblate (or prolate) starless core

continues to collapse into a centrally condensed envelope of a Class 0 protostar. A Class 0 source is created ($\sim$ 5000 AU in size), while the large scale filamentary structure ($\sim$ 1000 AU to 0.1 pc) remains behind containing an appreciable fraction of the total mass of the envelope plus source. In Step V, the Class 0 source evolves to a Class I source with a protostellar disk and the larger structure dissipates.

Although this scenario fits together, there is one serious problem with our proposed evolution of filaments in star formation: no one has detected the substructure (e.g. filamentary structure) predicted in Step III in starless cores to date. Unfortunately, there is some difficulty in detecting these structures. One could use molecular line tracers such as N_2H^+ or NH_3, which often correspond to the 8 μm absorption (e.g., Chiang et al., 2010; Tobin et al., 2011a). However in starless cores, N_2H^+ could still have chemical effects such as depletion (e.g., Bergin et al., 2002), although several studies showed Tafalla et al. (2002) less depletion for N_2H^+ than other molecules. Since the depletion usually ocurrs at the center of the core, the filament could appear fragmented in the map depending on the size of the central depletion. In addition, the molecular distribution could originate from chemistry and not well-trace the dense material. Thus, to confirm detection of substructure, we must rely on dust continuum emission. Dust emission at millimeter wavelengths presumably is more appropriate than 8 μm extinction because of the low optical depth. 8 μm extinction shows detection in the outer regions only if the background signal to noise is high enough.

In order to resolve the structures, we must have resolution of $\sim$5 arcsec, which implies interferometers. For example, Schnee et al. (2010) performed dust continuum observations at 3 mm toward 11 starless cores in Perseus with CARMA. Although two sources were detected, they were later reclassified as protostellar objects (Enoch et al., 2010; Schnee et al., 2012), implying only non-detections of sub-structure of starless cores, contrary to our suggested evolutionary sequence. Our explanation is that the sub-structure was not detected due to a lack of sensitivity. In the following section, we investigate that possibility and place constraints on the underlying filamentary structure based on Schnee et al. (2010) results.

2.3 Synthetic Observations

To examine the likelihood of our proposed structures in starless cores, we make synthetic observations with CARMA, directly comparing to the observations of Schnee et al. (2010), and ALMA, using the flattened envelope around L1157 as a model. The result will show that the expected structures are below CARMA D array's detection threshold at 3mm, but they should be detectable with CARMA D and E array observations at 3mm, CARMA E array at 1mm, and ALMA 1mm observations. This implies that there is not yet a disagreement between our observational-based proposed evolutionary scheme in Step III for low-mass star formation and current observations, and an exciting observational future is suggested.

2.3.1 CARMA observations

We simulate CARMA imaging with parameters used by Schnee et al. (2010): heterogeneous array (six 10-meter antennas and nine 6-meter antennas) imaging with the CARMA-D array configuration at 3 mm continuum. We use the Miriad tasks *uvgen*, *demos* and *uvmodel*, based on Wright (2010) without the 3.5-meter telescopes. To find the detection limit of such a structure, we also simulate CARMA D+E array observations at 3 mm and CARMA E array at 1 mm. Baselines range from $3k\lambda$ to $38k\lambda$ for the D array at 3 mm, $2k\lambda$ to $19k\lambda$ for the E array at 3 mm, and $5k\lambda$ to $47k\lambda$ for the E array at 1 mm. The observing rest frequency is centered at 90 GHz for 3 mm observations and 230 GHz for 1 mm observations with a total bandwidth of 4 GHz for continuum observations. The total observing time on the target is 6 hours for each synthetic observation (for the one with CARMA D+E array, the observing time is three hours for the D array and three hours for the E array). In the analysis (Sect 2.3.3), we perform a small mosaic (standard seven-pointings) around the source to capture all the extended structure. Table 2.1 summarizes the synthesized beam sizes and noise levels for the simulated CARMA observations.

2.3.2 ALMA observations

We used the task *sim_observe* and *sim_analyze* in the package *casapy* to perform the simulated observations with ALMA. The angular resolution is requested to be $1.2''$ in the simulation to observe detailed structures, and a small mosaic is applied to capture all possible structure. The

observing time for each mosaic pointing is 100 s, and the total observing time is 2 hours. The observing frequency is centered at 90 GHz with the bandwidth of 8 GHz for continuum observations. Thermal noise is added with a typical precipitable water vapor of 2.8 mm. The clean threshold is set to 1.5 times the noise rms, and the pixel size is set to 0.12 arcsecs.

2.3.3 Modeling and Results

As decribed in Step III and IV in Figure 2.5, the flattened protostellar envelopes around Class 0 sources are speculated to be highly connected to the filamentary structure at the previous stage, the prestellar phase. Therefore, the envelopes around Class 0 sources best describe the morphology of the high-density filamentary structures in Step III. To simulate the structure in Step III, we modify the flattened envelope in the Class 0 source L1157 by the physical conditions expected at the prestellar stage, in order to examine if CARMA and ALMA are able to detect filamentary structure at the prestellar stage. Figure 2.6(a) shows the extinction map of L1157 from the Spitzer 8μm observation (Looney et al., 2007). We chose L1157 to model as it has an obvious filamentary envelope structure seen in the 8μm absorption against the background emission, and the symmetric structure can be approximated with a radial density power-law (Looney et al., 2007). The spatial scale of the filamentary envelope is 0.1 pc, too large for a circumstellar disk or a pseudo disk (e.g., Galli & Shu, 1993). The L1157 dark cloud is located $\sim$ 250 parsecs[2] away with an edge-on view concealing the Class 0 source embedded in the flattened envelope nearly perpendicular to a large powerful outflow from the north to the south. The distance to L1157 is approximately the same as Perseus (also at $\sim$ 250 pc) and thus remains an excellent proxy for Perseus when comparing with Schnee et al. (2010). If the proposed scenario of filamentary collapse is correct, the flattened envelope is expected to be related to the filamentary structures on larger scales, and thus this source is suitable for modeling the transient phase in the prestellar stages with appropriate physical conditions.

To better concentrate on the filamentary envelope, we removed the emission from the outflow and the scattered light from the central object. We then filled the inner regions with the averaged value from the envelopes on the two sides, as shown in Figure 2.6(b). The total mass calculated from

[2]The L1157 cloud is estimated to have a similar galactic latitude as the absorbing clouds with 200 pc and 300 pc in Cepheus (Kun, 1998) and therefore we adopted a distance of 250 pc in this paper. In comparison, Kirk et al. (2009) adopted a distance of 325 pc for the region around L1157.

the extinction increased by about 10% by filling the inner region with this method. The extinction map was compared toward background stars measured in the near-IR to an optical-depth image generated with or without the zodiacal correction (Tobin et al., 2010).

We next generated the brightness map at millimeter wavelengths (at 3 mm in our model) by assuming that L1157 is optically thin at 3 mm. We first calculated the mass contained in each pixel from the extinction map,

$$M = d\Omega \times D^2 \times \left(1.496 \times 10^{13} \times \frac{\mathrm{cm}}{\mathrm{AU}}\right)^2 \times \frac{\tau}{\kappa_{8\mu m}},$$

where $d\Omega$ is the pixel solid angle $(1.2'')^2$, D is the distance in parsecs (250 pc for L1157) and $\kappa_{8\mu m}$ is the dust plus gas opacity at $8\mu m$. The 3 mm flux in each pixel is then determined from the mass, opacity, and temperature,

$$F = \frac{M \times B_\nu(T) \times \kappa_{3mm}}{D^2},$$

where $B_\nu(T)$ is the Planck function and κ_{3mm} is the dust plus gas opacity at 3mm.

We used 0.00169 cm^2 g^{-1} for κ_{3mm} by assuming 100 for the gas to dust ratio (e.g., Schnee et al., 2010). The temperature was assumed to be a constant at 10 K for starless cores (e.g., Schnee et al., 2009). After obtaining the brightness map at 3 mm, we simulated the CARMA D array observations with our model. Since the opacity in the infrared is poorly constrained, we generated models with varying values for $\kappa_{8\mu m}$, which also modifies the derived mass in the flattened envelope structure. The equation above indicates that the observed millimeter brightness decreases with increasing $\kappa_{8\mu m}$, since less mass is required to produce the IR extinction. In the left panel of Figure 2.7, we show that with an expected value of $\sim$ 10.96 cm^2 g^{-1} for $\kappa_{8\mu m}$ (Tobin et al., 2010; Butler & Tan, 2009) toward L1157, the CARMA-D array is not able to detect the filamentary structures at the prestellar stage. For the structures to be clearly detcted (the right panel of Figure 2.7), the dust opacity at 8 μm would have to be an unphysically small value.

To fully explore CARMA's capability, we performed the synthetic observation with CARMA D+E array at 3 mm since the E array is more compact and sensitive to emission at larger scales than the D array. The total observing time is six hours (three hours with the D array and three hours with the E array). The value for $\kappa_{8\mu m}$ used is 10.96 cm^2 g^{-1} to compare with the result from

the D array only, since it produces the weakest emission (contains the least mass). As shown in Figure 2.8, the filamentary structure is detected with a similar noise level (0.28 mJy/beam) as the D array (0.3 mJy/beam), although only the structures with stronger emissions close to the center could be seen and the structures are not in detail. The detection suggests that the non-detection with the D array is due to a combination of spatial resolution and sensitivity. Furthermore, we shift the observation from 3 mm to 1 mm assuming that the dust opacity is 0.9 cm^2 g^{-1} at 1 mm (Ossenkopf & Henning, 1994) and $\kappa_{8\mu m}$ is still 10.96 cm^2 g^{-1}. Again, CARMA E array is able to show detection on the structure as shown in Figure 2.9, as the brightness increases toward the short wavelengths.

We further ran the synthetic observations with ALMA also for the case of $\kappa_{8\mu m} = 10.96$ cm^2 g^{-1}. Figure 2.10 shows the result from the synthetic observation (the contours are plotted by percentages of the peak flux instead of the noise levels due to the artificial effects from resolving-out large structures). As can be clearly seen, ALMA is able to detect most of the structure in the flattened envelope. Comparing the results from CARMA and ALMA for $\kappa_{8\mu m} = 10.96$ cm^2 g^{-1}, ALMA's unprecedented sensitivity greatly improves the appearance of filamentary structures and should provide a powerful tool for uncovering any hidden filamentary profiles at the starless/prestellar stage. Located in the southern hemisphere, ALMA is not able to look at L1157; these results are, however, indicative of the ALMA observations with other starless cores.

2.4 Conclusion

In this paper, we posit an observationally derived scenario for filament-driven star formation that incorporates the evolution of star-forming cores with filaments into filamentary envelopes from large to small scales. Molecular clouds are formed as filaments (few parsecs to 10 parsecs) and then fragment to smaller filaments (few tenths of parsecs), which eventually collapse to form triaxial starless cores. As collapse continues the material infalls along the filament into a centrally condensed filamentary envelope of a spherical Class 0 source, which keeps evolving to a Class I source with a protoplanetary disk.

If such a scenario is correct, the filamentary structures at the prestellar stage should exist. The only reason that they have not yet been detected is sensitivity to large-scale emission in the surveys.

They are possible to detect with CARMA D+E array at 3 mm due to more appropriate resolution and CARMA E array at 1 mm as a result from the higher brightness at 1 mm; however, ALMA is even more capable of clearly detecting detailed structures of the filamentary envelopes. In fact, the very high sensitivity of ALMA will allow for much shorter integrations (less than two hours for L1157-like prestellar cores) and thus we will be able to conduct quick and efficient surveys of the geometry of the envelopes around starless cores. The scenario proposed scenario can be immediately tested by observations with the current instruments.

Table 2.1: Synthesized beam sizes and noise levels for the synthetic observations

	CARMA D array 3 mm	CARMA D+E array 3 mm	CARMA E array 1 mm
L1157 modeling (Sect 2.3.3)	$5.14'' \times 4.76''$ 0.3 mJy beam^{-1}	$7.92'' \times 7.23''$ 0.15 mJy beam^{-1}	$4.21'' \times 3.65''$ 0.35 mJy beam^{-1}

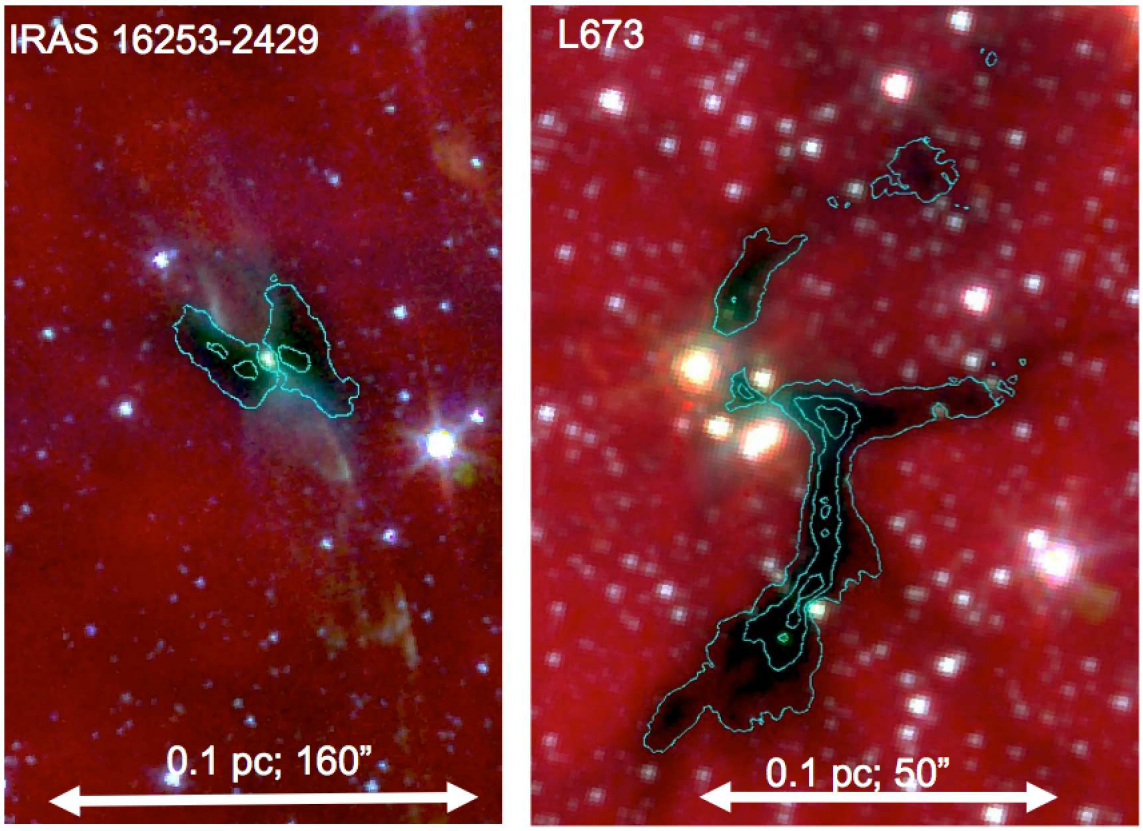

Figure 2.1: Example of the envelopes detected with Spitzer 8 micron imaging from Tobin et al. (2010). The images are from *Spitzer* 8.0 μm observations.

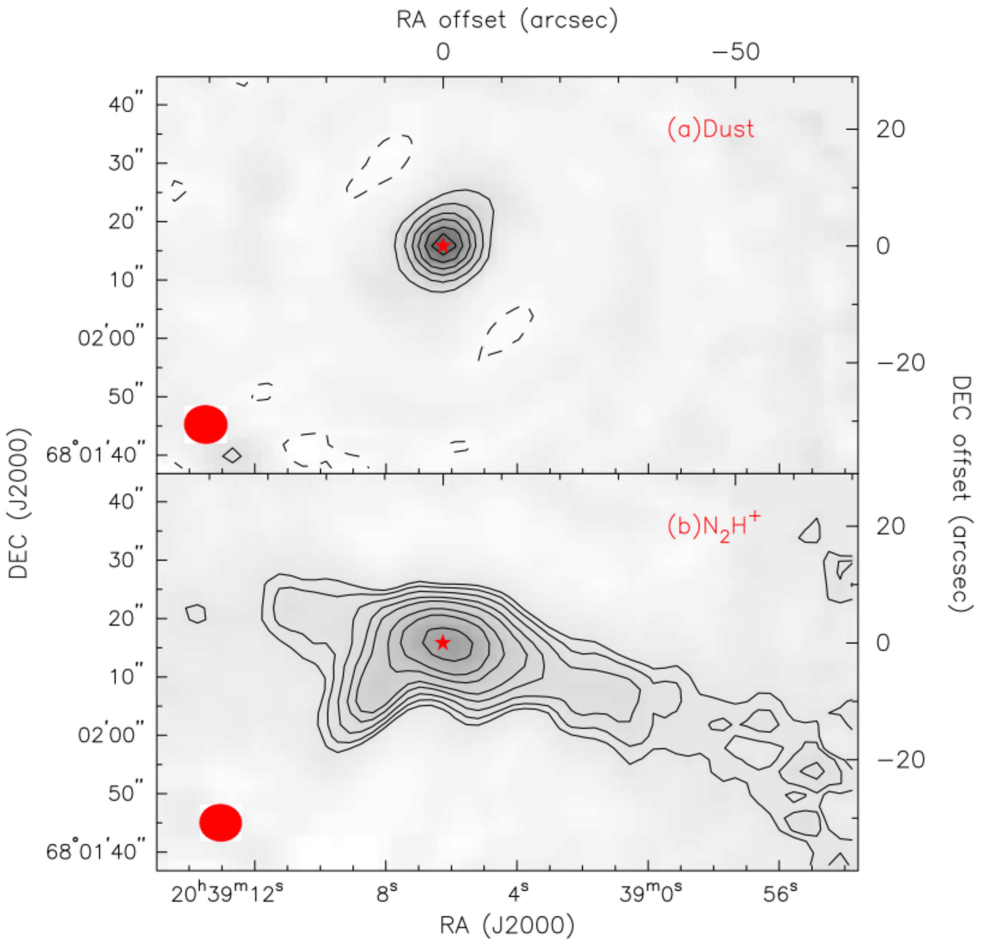

Figure 2.2: Example of dust and N2H+ differences from Chiang et al. (2010). However, both emission was fit in a simple density model.

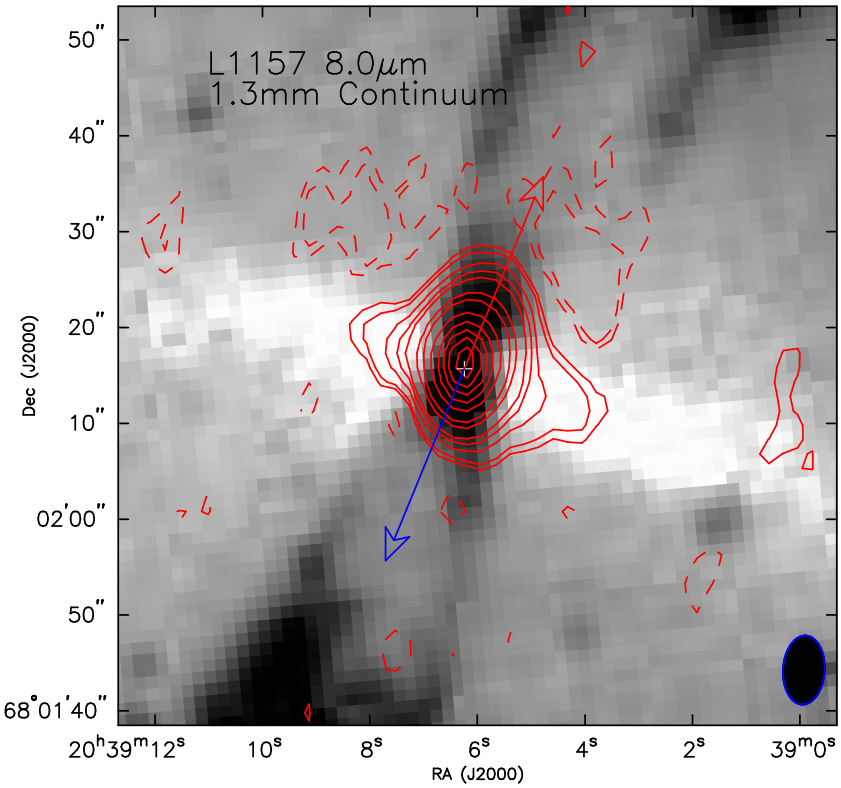

Figure 2.3: With higher sensitivity, SMA observations detect the extension of the flattened envelope and the increased heating along the outflow cavity. The blue and red arrows indicate the outflow directions of the blue-shifted and red-shifted component, respectively. The beam size is in the bottom-right corner. The contours are $\pm 2, \pm 3, 6, 9, 12, 22, 30, 50\sigma$, where $\sigma = 2.16$ mJy beam^{-1}.

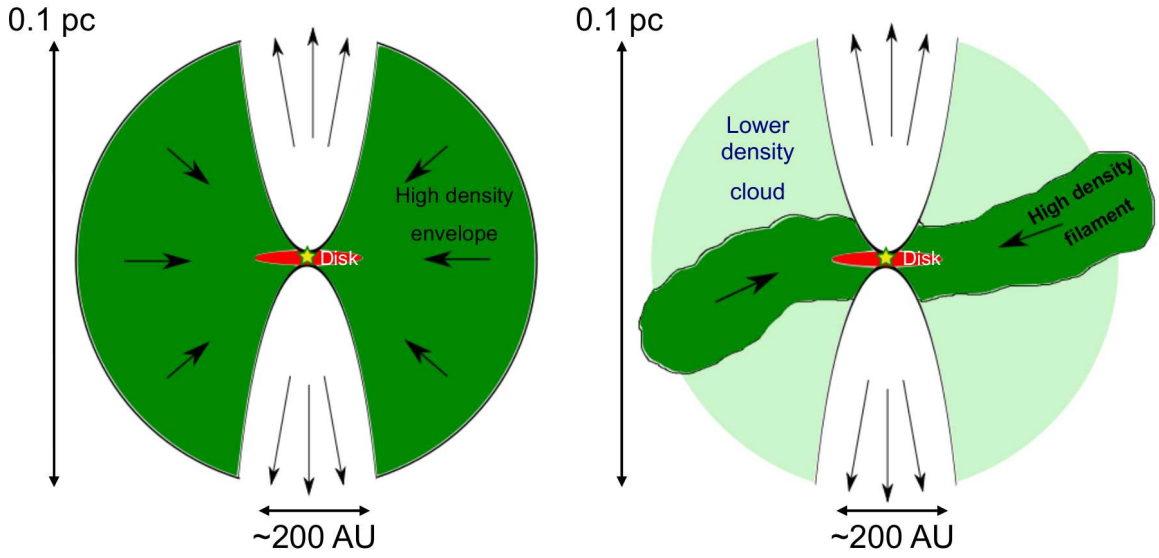

Figure 2.4: Schematic view showing the changing view of star formation from spherical collapse (left panel) to filamentary collapse (right panel). Note that the size scales are exaggerated to better illustrate the structures.

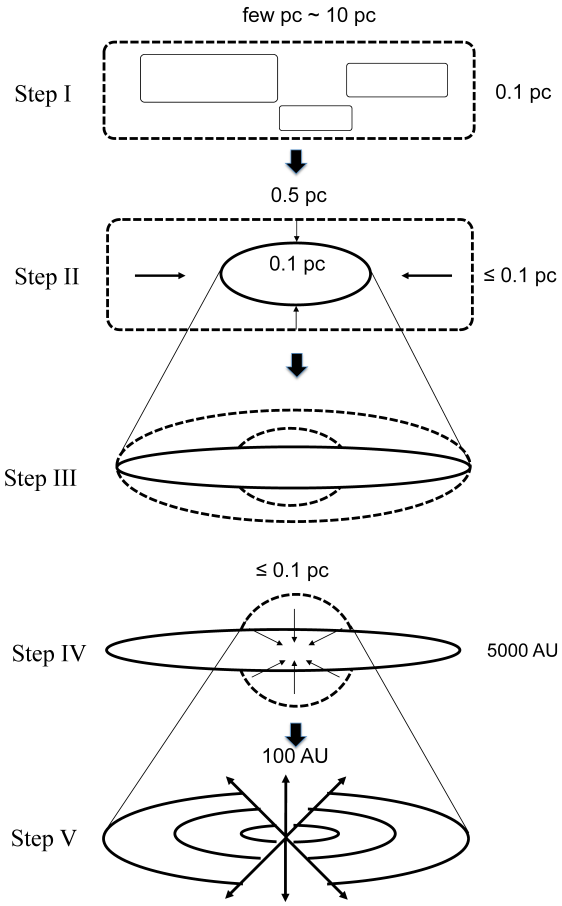

Figure 2.5: Illustration of filamentary collapse in five Steps. In Step I, molecular clouds are formed with filamentary shapes (few parsecs in length and 0.1 pc in width) that are prone to fragmentation. In Step II, the subsequently-fragmented filaments (few tenth of parsecs in length) collapse and form prolate or oblate starless cores (0.1 pc in size). In Step III, embedded in the starless core is a filamentary structure of higher density that arises from the flow along the the large-scale filament axis. In Step IV, the starless core continues to infall into a centrally condensed envelope of a Class 0 protostar ($\sim$ 5000 AU). In Step V, the Class 0 source evolves to a Class I source with a protostellar disk (few hundred AUs) and outflow (the arrows). The orientation of the protostellar disk depends on the detailed kinematics of collapse and is not necessarily along the filament as shown in this cartoon. Note in each step the structures with lower density are indicated with dashed lines.

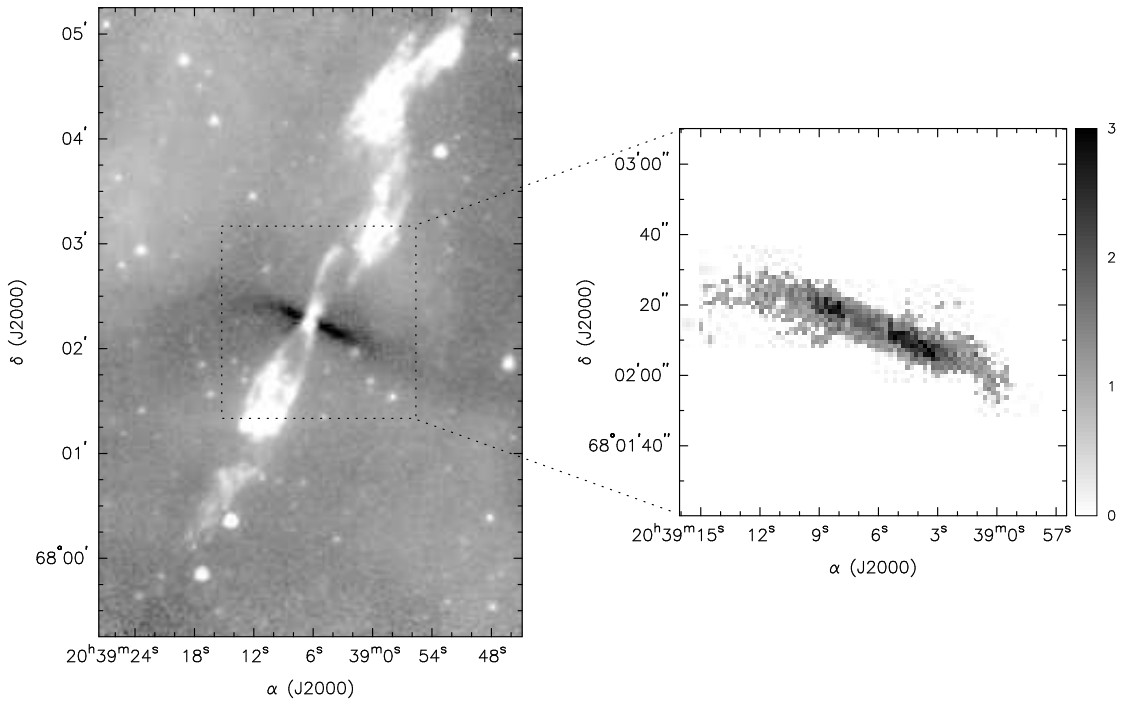

Figure 2.6: (a): the left panel. It is the extinction map of L1157 from the Spitzer 8 μm observation. A flattened envelope is seen in absorption against the background emission around the central Class 0 object with the outflow nearly perpendicular to it. (b): the right panel. The emission from the outflow and the scattered light from the central object are removed. The central part is filled with the average of the envelopes on the two sides. The color scale shows optical depth.

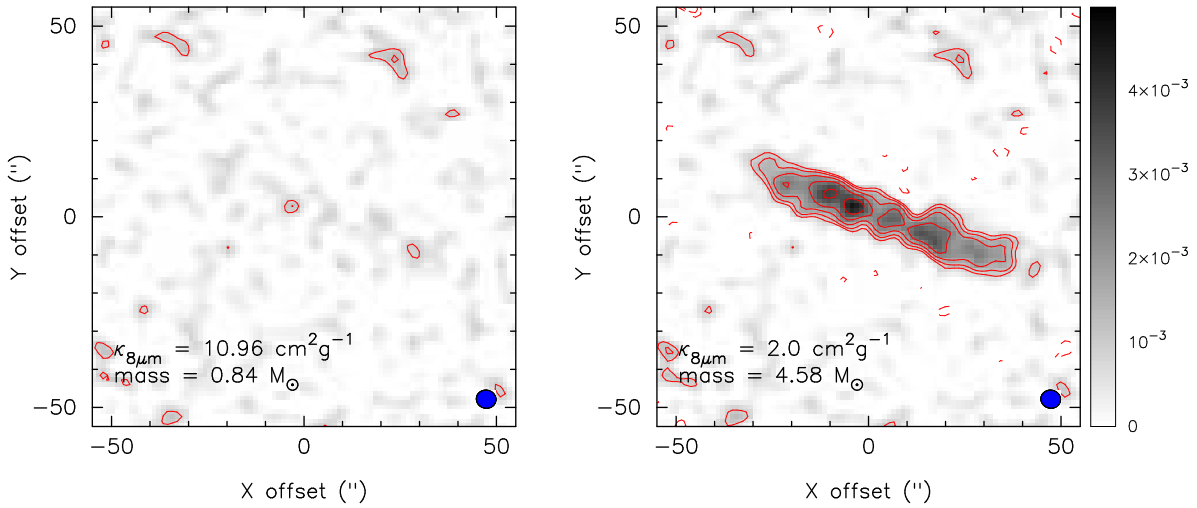

Figure 2.7: Simulated observations with CARMA D array at 3 mm for six hours with different values of $\kappa_{8\mu m}$. The center is positioned at $20^h39^m05.2^s$ (RA) and $68°02'15.3''$ (Dec) (J2000). The synthesized beam size is 5.14″by 4.76 ″shown on the bottom-right corner. The noise level σ is 0.3 mJy/beam, and the contours are $\pm3, \pm4.2, \pm6, \pm8.5, \pm12, \pm17, \pm24, \pm34 \times \sigma$ (in step of $\sqrt{2}\sigma$). The color scale shows flux in Jy/beam. With the reasonable value for $\kappa_{8\mu m}$ (10.96 cm^2 g^{-1}) in the left panel, no structures are detected. For the structures to be clearly detected (the right panel), $\kappa_{8\mu m}$ needs to be an almost impossibly small value (2.0 cm^2 g^{-1}).

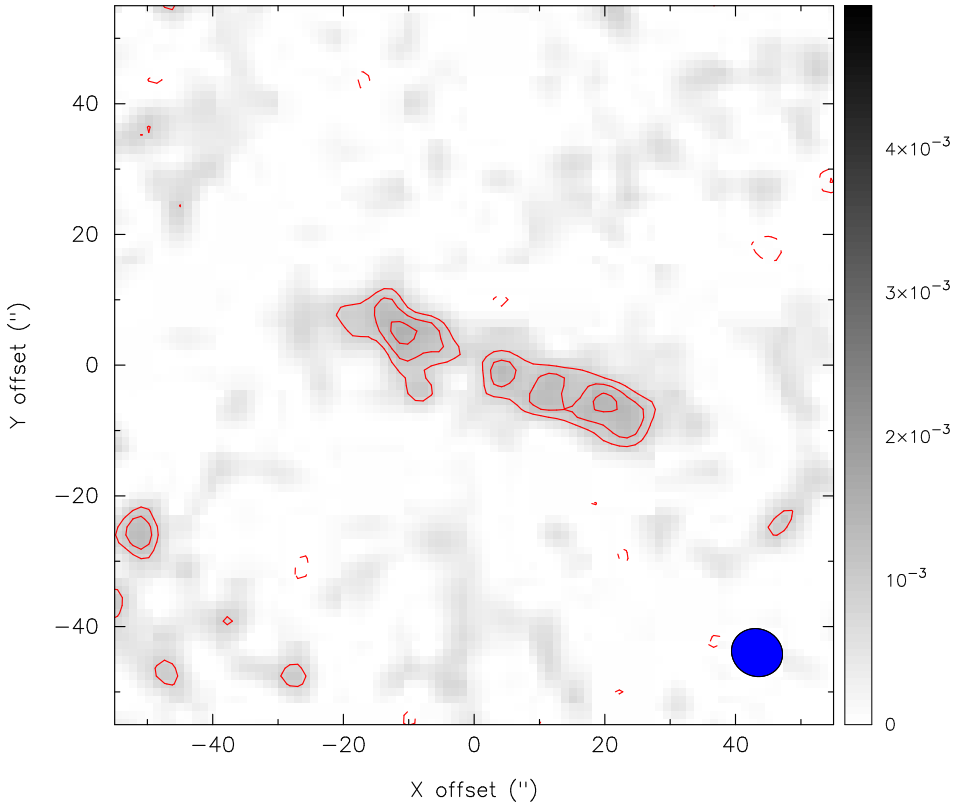

Figure 2.8: Simulated observations with CARMA D+E array at 3 mm for six hours in total (three hours for the D array and three hours for the E array). The value for $\kappa_{8\mu m}$ is 10.96 cm^2 g^{-1}. The center is positioned at $20^h39^m05.2^s$ (RA) and $68°02'15.3''$ (Dec) (J2000). The synthesized beam size is $7.92''$by $7.23''$shown on the bottom-right corner. The noise level σ is 0.28 mJy/beam, and the contours are $\pm3, \pm4, \pm5, \pm6, \pm7, \pm8, \pm9, \pm10 \times \sigma$. The color scale shows flux in Jy/beam.

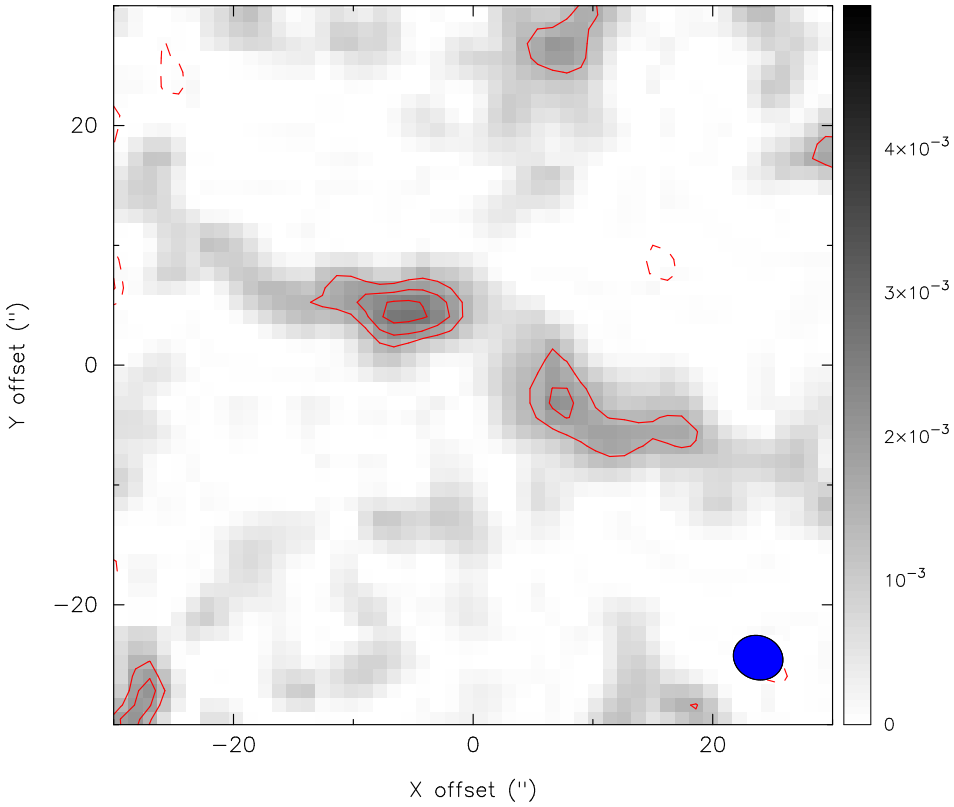

Figure 2.9: Simulated observations with CARMA E array at 1 mm for six hours in total. The value for $\kappa_{8\mu m}$ is 10.96 cm^2 g^{-1}. The center is positioned at $20^h39^m05.2^s$ (RA) and $68°02'15.3''$ (Dec) (J2000). The synthesized beam size is $4.21''$by $3.65''$shown on the bottom-right corner. The noise level σ is 0.49 mJy/beam, and the contours are $\pm3, \pm4, \pm5, \pm6, \pm7, \pm8, \pm9, \pm10 \times \sigma$. The color scale shows flux in Jy/beam.

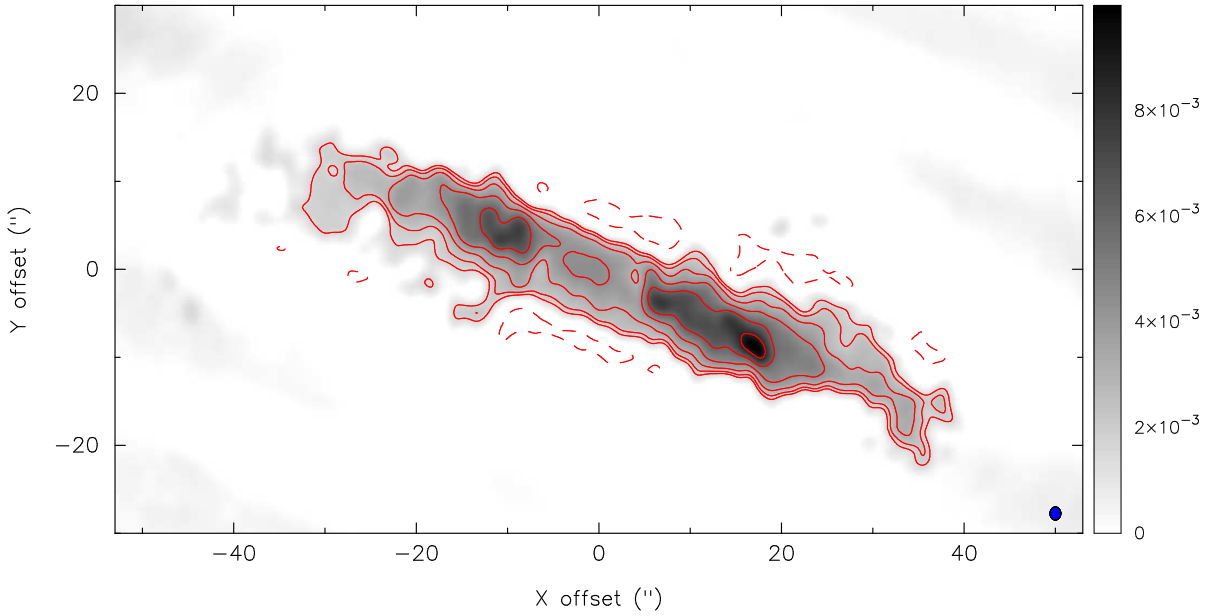

Figure 2.10: Simulated observations with ALMA for $\kappa_{8\mu m} = 10.96$ cm^2 g^{-1}. The noise level σ is 0.15 mJy beam^{-1}. The contours indicate $\pm 10, \pm 15, \pm 20, \pm 25, \pm 30, \pm 40, \pm 50, \pm 60 \times \sigma$. The color scale shows flux in Jy/beam. The synthesized beam size is $1.2''$ shown on the bottom-right corner.

Chapter 3

Massive Star-formation around IRAS 05345+3157: The Dense Gas

This chapter was published in Lee et al. (2011)[1].

3.1 Introduction

Despite the well-known fact that most stars form in clusters (e.g., Lada & Lada, 2003), little is known about the detailed formation process of massive stars or star clusters. In contrast to the well-studied mechanisms for low mass star formation, the difficulty for massive star formation is mainly due to a massive star's high radiative power. The strong radiation hinders infalling material in the envelope from further accreting onto the central source. Two major theories have been proposed to solve the puzzle. Accretion can still be accomplished through a high accretion rate generated by the turbulent environment (McKee & Tan, 2003) and also through disks (e.g. Krumholz et al., 2005a) with outflows that greatly reduce the radiative pressure (Krumholz et al., 2005b). On the other hand, massive stars could also form from competitive accretion or stellar mergers (Bonnell et al., 2001, 2004) in high stellar density regimes. The formation of star clusters can be due to fragmentation of molecular clouds (e.g., Bate & Bonnell, 2005), although Krumholz et al. (2007) concluded that the fragmentation of pre-stellar massive cores can be avoided through heating, allowing the formation of a massive star from one massive core. Only through a detailed investigation of the initial conditions in a protocluster system can we better address the problem of massive star formation.

Massive protostars have strong interactions with their ambient environment. They disperse their natal clouds through stellar winds and UV radiation (see the review by Zinnecker & Yorke, 2007). After such dynamical interactions, the ambient environment changes enormously and no

[1]This chapter is previously published in *The Monthly Notices of the Royal Astronomical Society* as "Massive star formation around IRAS 05345+3157 - I. The dense gas", Lee, Katherine, Leslie Looney W., Klein, Randolf, and Wang, Shiya, 2011, MNRAS, 415, 2790 and is reproduced here with permission of the Oxford Journals.

longer preserves the initial conditions from when massive protostars were first born. Therefore, in order to examine the very early conditions of the onset of massive star formation, identifying stellar objects at early evolutionary stages (e.g., Seale et al., 2009) in protoclusters appears to be very essential. Beuther et al. (2007a) suggested that the early evolution has four stages starting with High-Mass Starless Cores (HMSCs), which then accrete low and intermediate mass protostars, leading to High-Mass Protostellar Objects (HMPOs) and finally the (still deeply embedded) final star.

Here we report on the massive star-forming region around the FIR-bright IRAS source 05345+3157, hereafter I05345. The IRAS source is associated with an IR cluster surrounded by molecular gas at a distance of 1.8 kpc (Henning et al., 1992). HCO^+(2-1) emission east of I05345 presents complex and clumpy structures, suggesting that the source is on the verge of collapse through the contraction of local density peaks (Molinari et al., 2002). A massive outflow has been observed in CO(2-1) (Zhang et al., 2005; Fontani et al., 2009), a typical signature of young stellar objects. Klein et al. (2005) shows a ring of dust emission around the cluster I05345 in 850 μm continuum data. Two compact and massive dust clumps are located in the ring to the east of the cluster: I05345 #1 and #2, with the mass of 48 $M_\odot$ and 38 $M_\odot$, respectively. Futhermore, Fontani et al. (2008) and Fontani et al. (2009) concluded several objects at different evolutionary stages in this region with SMA and PdBI observations, including prestellar core candidates, young intermediate to high mass class 0 protostars, and an early-B ZAMS star. The same papers also revealed two condensations in N_2D^+(2-1) and the nature of the deuterated cores have been studied in detail.

The previous observations showed the possibility of active star formation in I05345. The main goal of this paper is to study star formation by investigating the dense gas in the I05345 environment. Our strategy uses the $CS(2-1)$ transition as a probe of gas cores to comprehensively study gas properties. We use the D array configuration of the Combined Array for Research in Millimeter-wave Astronomy (CARMA) to resolve-out large-scale structures and trace dense gas fragments ($\sim 10^5$ cm^{-3}) inside the cloud. In this paper we present $\sim 5''$ angular resolution data of $CS(2-1)$ and 2.7 mm continuum. In the companion paper by Klein et al. (2011) (hereafter paper II), we examine the infrared properties of the fragments. With the two papers, we obtain a general picture of star formation in I05345.

3.2 Observations

3.2.1 CARMA observations

Observations of the line transition CS $J = 2 \rightarrow 1$ ($\nu = 97.981$ GHz) toward the clumps I05345 #1 and #2 (Klein et al., 2005) were made with CARMA in 2008 June. The observations used CARMA D array at $\lambda = 2.7$ mm. The CS$(2-1)$ transition was placed in a correlator window of 8 MHz width and a velocity resolution of 0.37 km s^{-1}. Two 500 MHz bands were set up for continuum observations. The phase center was chosen between I05345 #1 and #2 at $RA = 05^{\rm h}37^{\rm m}52.6^{\rm s}$ and $DEC = +31°59'48.0''$ (J2000) using the local standard of rest velocity $V_{\rm LSR}$ of $-18.6\,{\rm km\,s^{-1}}$ (Schreyer et al., 1996). 0555+398 was used as the phase calibrator. 3C454.3 and Uranus were used for the bandpass calibration and the flux calibration, respectively. The system temperature ranged from 50 K to 300 K with 200 K (single sideband) being a representative value. The baselines ranged from 11 meters to 150 meters. The channel maps were generated with natural weighting, producing a synthesized beam of $5.7'' \times 4.2''$. The primary beam size of the CARMA combined array is $85''$at 98 GHz. The data reduction was done using the MIRIAD package (Sault et al., 1995). The amplitude calibration is estimated to be 10%, and the uncertainties discussed afterwards are only statistical not systematic.

3.3 Results

3.3.1 CS Zeroth Moment Map and Spectra

Figure 3.1 shows the velocity-integrated intensity map of CS$(2-1)$; the dashed circle is approximately the primary beam size of the 10-m antennas in CARMA ($\sim 69''$) at λ=2.7 mm. We identify seven cores with peak intensities above 5σ ($1\ \sigma \sim 0.25$ Jy beam^{-1} km s^{-1}) inside the primary beam of the integrated CS map . Due to the interferometric effect that introduces the negative components in the map, it is possible that the weak emission associated with core 2 is spurious. The boxes shown in the right panel of Figure 3.1 are used for deriving the parameters of the cores (see the paragraph below) and are drawn based on the 3σ detection.

For this study, we only focus on the cores inside the primary beam size of the 10-m OVRO dishes and neglect the emission outside the primary beam, which has a lower sensitivity and signal-

to-noise ratio. Core 1 is isolated in the south. Cores 3 and 4 are spatially close and entangled. In Table 3.1 the parameters of each core are specified, including the observed sizes (major axis a_0, minor axis b_0 and position angle P.A.$_0$), the deconvolved sizes (major axis a, minor axis b and position angle P.A.) and the equivalent radius R=$\sqrt{ab}/2$. The major and minor axes are derived by fitting a circular or elliptical Gaussian profile in the velocity-integrated map of CS. At the distance of 1.8 kpc, the sizes of these cores range from 0.05 pc to 0.08 pc (see Table 3.1), which is the typical size of transition groups from Hot Molecular Cores (HMCs) to Ultracompact HII regions (UCHIIs) (Beuther et al., 2007a) or of low-mass envelopes (e.g., Looney et al., 2000).

The spectra of the seven cores averaged over the boxes in Figure 3.1 are shown in Figure 3.2. Most of the spectra show a strong single-peaked emission, while the spectra of core 2 and 3 are double peaked. The spectra are fitted by Gaussian profiles as shown in Figure 3.2. Since the double peaks in the spectra of core 2 and core 3 may result from self-absorption (Sect. 3.4.1), we fit the profiles with one Gaussian emission and one Gaussian absorption line superimposed. Table 3.2 lists the fitting parameters for each core (amplitude, peak position of velocity, FWHM). Note that the spectrum of core 4 shows a red wing emission and that of clump 6 shows a blue wing emission above the fitted line. The line wings may be due to the outflow driven by core 3 (see Sect. 3.4.2).

3.3.2 Millimeter Continuum Data

Figure 3.3 shows the contours of the CS intensity map overlaid on the 2.7 mm continuum data from the same observation. There are three 2.7 mm continuum emission peaks in the map (MM1, MM2 and MM3). MM1 in the south is the brightest core (22.7 ± 7.2 mJy). MM2, the faintest (6.0 ± 1.4 mJy), is in the north accompanied by the brighter MM3 (13.8 ± 3.6 mJy). These sources are all unresolved.

Comparing the λ=2.7 mm observation with CS cores, we see that core 1 is associated with MM1 although the two peaks are shifted by about $3''$, smaller than the beam size. Core 3 coincides with MM3, while MM2 shows no CS emission (see below). There are no other 2.7 mm emission features associated with the rest of the CS cores.

MM3 and MM1 correspond to the clumps I05345 #1 and #2 for which Klein et al. (2005) derived masses of 48 $M_\odot$ and 38 $M_\odot$, respectively. Cores 2, 3 and 4 are all associated with the northern clump I05345 #1. In addition, the three cores C1, C2, and C3 in 225 GHz continuum

observation by Fontani et al. (2008) coincide with MM3, MM2, and MM1, respectively.

The cores MM1 and MM3 have been consistently detected in the (sub-)millimeter continuum and also in the FIR by Spitzer (see paper II for details). Figure 3.3 shows the Spitzer 24 μm image; the bright northern source corresponds to our core 3 and the southern source corresponds to core 1. It is peculiar that at 2.7 mm the northern source is the weaker one of the two while at all other wavelengths from 24 μm to 1.3 mm (the 225 GHz observation in Fontani et al. (2008)) the northern source is the dominant source. We speculate that there is extended emission that contributed to the single-dish observation by Klein et al. (2005), which is resolved out by the interferometer. Thus, the fluxes seen by the interferometer are smaller than expected from the single-dish observations, and one would expect that the effect is more pronounced for the larger core MM3.

MM2 shows no counterpart at 850 μm or in the FIR, but it does have a counterpart at 3.6 cm (Molinari et al., 2002); therefore, the continuum emission from core MM2 is likely dominated by free-free emission from an HII-region with only a fraction of the emission from warm dust.

3.3.3 Estimating the Core Mass

We present three approaches to roughly estimate the core masses. The first method is the LTE mass calculated from the integrated flux of the CS$(2-1)$ line transition. The second method is calculating the virial mass from the line width of CS spectra. The third method is based on the 2.7 mm continuum assuming dust emission and a dust-to-gas ratio.

LTE Mass

Following the standard rotation temperature - column density analysis (e.g., Turner, 1991), CS$(2-1)$ spectra can be used to derive the column density, and further the mass of the dense gas. Because the transition CS$(2-1)$ is not optically thin, a correction factor needs to be applied to the LTE mass derived from the assumption of an optically thin line. For an optically thin molecular line, by assuming all the transitions are excited by a single temperature T_{ex} (LTE) and negligible background continuum emission, the column density can be calculated from (e.g., Miao et al., 1995; Mehringer, 1995)

$$\begin{aligned}\mathrm{N}\ (cm^{-2}) =& 2.04\times10^{20}\times[\frac{1}{\theta_a\theta_b(arcsec^2)}]\\ &\times[\frac{Qe^{E_u(K)/T_{ex}}}{\nu^3(GHz^3)S\mu^2(debye^2)g_kg_I}]\\ &\times[\int I(Jy\ beam^{-1})dv(km\ s^{-1})]\ ,\end{aligned}$$

where θ_a and θ_b are the FWHM of the synthesized beam, Q is the partition function, $\mathrm{E_u}$ is the upper energy level of the transition, ν is the line rest frequency, S is the line strength, and μ^2 is the dipole moment, g_k and g_I are the usual K-level and reduced nuclear spin degeneracies. For our observation, θ_a=5.9″, θ_b=4.3″, Q=0.86$\mathrm{T_{ex}}$ (Rohlfs & Wilson, 2000), $\mathrm{E_u}$=7.05 K, ν=97.980968 GHz, S=2, μ=1.96 debye, and g_I=g_k=1. Here we assume an excitation temperature of 20 K for dense cores forming massive stars (see review by Zinnecker & Yorke, 2007). We note that the assumption of a single excitation temperature for Core 3 which shows a possible infall signature (Sect. 3.4.1) may be inaccurate since a gradient in the excitation temperature in an infalling source is expected (Evans, 1999). In the case of an optically thick molecular line, a correction factor C_τ should be applied (e.g., Goldsmith & Langer, 1999):

$$\mathrm{N_{total}} = C_\tau \mathrm{N} \text{ and}$$

$$C_\tau = \frac{\tau}{1-e^{-\tau}}\ ,$$

where τ is the optical depth and can be derived from

$$\tau = -\ln[1-\frac{T_{MB}}{J(T_{\mathrm{ex}})-J(2.73)}]$$

(Rohlfs & Wilson, 2000), where $\mathrm{T_{MB}}$ is the main beam brightness temperature and

$$J(T) = \frac{h\mu}{k}\frac{1}{e^{h\mu/kT}-1}.$$

Therefore, by assuming uniform densities, the LTE mass can be derived from

$$M = \mu m_H \frac{N}{X}(1.133abD^2)$$

where $\mu = 2.33$ is the mean molecular weight, m_H is hydrogen mass, D is the distance (1.8 kpc for I05345), X is the abundance ratio of CS to H_2, which is assumed to be 10^{-9} here (Rohlfs & Wilson, 2000), and a and b are the major axis and minor axis of a defined core. Furthermore, we calculated the number density of molecular hydrogen for these cores by assuming ellipsoidal cores and a, b and b for the three axes: $n_{H_2} = M_{LTE}/2M_H/(4\pi/3(a/2)(b/2)^2)$. The column density and number density of H_2 range from 2.7×10^{22} to 11.6×10^{22} cm^{-2}, and from 0.6×10^6 to 1.7×10^6 cm^{-3}, respectively. The LTE masses of the different cores range from ~ 2 M$_\odot$ to 15 M$_\odot$. Table 3 lists the integrated line intensity ($I_t = \int I dv$), the derived optical depth τ, the column density of CS (N_{CS}), the number density of H_2 and the results of LTE mass.

The smallest core mass that our observations are sensitive to is $\sim 1\,M_\odot$. This is the result of the same calculation as above assuming a flux equivalent to 3σ in integrated flux map. Fontani et al. (2009) observed their condensations N and S in N_2D^+ and N_2H^+ and expected them to be low-mass cores ($< 1\,M_\odot$) according to the observed deuterium fraction. Thus, it is not surprising that we don't detect their condensations N and S.

In the calculation of the LTE masses, a value of 10^{-9} for the CS(2-1) molecular abundance is assumed and the abundance is also assumed to be a constant. However, due to C-bearing molecules frozen onto dust grains at early stages of star formation, a central depletion of CS(2-1) is usually seen in prestellar cores (e.g. Tafalla et al., 2002; Stahler & Yen, 2010), and therefore the assumption of a constant abundance may lead to larger uncertainties in the calculation. Also, according to different models or calculations, the derived values for CS(2-1) abundance are various (e.g. Belloche et al., 2002; Pirogov et al., 2007). In most literatures, the abundance profile is described by a central depletion and a nearly constant value between 10^{-9} and 10^{-8} follows at outer parts of cores. Since the radii where the abundance drops is usually very close to the center of prestellar cores, we simplify the LTE mass estimation by only adopting the plateau part of the molecular abundance. The choice of 10^{-9} sets the upper limit for the calculation and the derived LTE masses could vary by about one order of magnitude depending on the chosen values for the abundance.

Virial Mass

By assuming the cores are in virial equilibrium, we can derive the virial mass using the line width of CS. We assume a standard isothermal density profile for the cores from Shu (1977), $\rho = \rho_0 r^{-2}$ (cf. Looney et al., 2003b). In this case, the virial mass can be derived from

$$M_{vir} \sim \frac{3R}{G} \frac{\Delta V^2}{8 \ln 2} ,$$

where ΔV is the FWHM of the observed molecular line (see Table 2). The derived virial mass for each core is listed in Table 3. For core 2 and 3 with the double-peak spectrum, we use the line width of the emission line to derive the virial masses.

Total Mass Estimation from Continuum Emission

Here we adopt the standard technique to estimate the total mass from the continuum emission, in our case the 2.7 mm continuum data for core 1 and 3 (remember that core 2 could have considerable free-free emission; Sect. 3.3.2). This method assumes that the continuum emission is from dust and a dust-to-gas ratio. By assuming optically thin emission and a single temperature (isothermal), the total mass (dust + gas) is

$$M = \frac{F_\nu D^2 R}{B_\nu(T_{dust})\kappa_\nu}$$

where F_ν is the flux density, D is the distance to the source, R is the gas-to-dust ratio, $B_\nu(T_{dust})$ is the Planck function at dust temperature T_{dust}, and κ_ν is the dust opacity. The flux density of core 1 is 22.7 ± 7.2 mJy and that of core 3 is 13.8 ± 3.6 mJy. For the dust opacity, assuming a gas density $\sim 10^6$ cm^{-3}, we adopt the extrapolated value of 0.29 cm^2 g^{-1} at λ=2.7 mm for prestellar core dust with thin ice mantles from Ossenkopf & Henning (1994). The extrapolation was done with a power law ($\kappa \propto \lambda^{-\beta}$) and a value of $\beta = 1.77$, obtained by fitting the respective κ-values in the FIR ($\lambda > 300\mu$m). Therefore, with the assumption of 20 K for the dust temperature and 100 for the gas-to-dust ratio, we derive the mass of $18 \pm 6\, M_\odot$ for core 1 and $11 \pm 3\, M_\odot$ for core 3. The derived masses depend much on the assumed values for the dust temperature, the opacity, and the dust-to-gas ratio. The error of the mass estimates given above only reflects the uncertainty in the flux measurement. Taking the uncertainties of the assumptions into account the estimate is good

within one order of magnitude. For example, if we would assume a rather high temperature of 47 K (Paper II) for core 3 the core mass would only be 7 $M_{\odot}$. If we would use the opacity for dust grains without ice mantels the mass would also drop to 7 $M_{\odot}$.

The calculation shows that the total mass from the LTE method and continuum emission of core 1 and core 3 are (5±1 $M_{\odot}$, 18±6 $M_{\odot}$) and (15±7 $M_{\odot}$, 11±3 $M_{\odot}$), respectively. Both methods have uncertainties. For example, the results depend on the assumptions of physical conditions and quantities, such as the excitation and dust temperature, wavelength dependence of the dust opacity etc. In CS(2-1) emission, core 3 is brighter than core 1, while it is opposite in the 2.7 mm continuum emission (see section 3.3.1 and 3.3.2). This result causes the larger LTE mass of core 3 and larger mass by assuming a dust-to-gas ratio of core 1. Other mid-infrared to FIR observations (see paper II) show a brighter core 3 than core 1, consistent with our CS(2-1) observation. Therefore, in the following discussion, we use the LTE mass to compare it with the virial mass, a method consistent with Saito et al. (2006).

3.4 Discussion

3.4.1 A Collapsing Core

Figure 3.4 shows two CS$(2-1)$ integrated intensity maps integrated over velocities of the blue and red components of the self-absorption spectrum of core 3. The boxes drawn in these two maps are the same box as in Fig 3.1. Both of the integrated intensities from the blue and red peak are in the same box.

Arguably, this result suggests that the double-peak structure comes from the same core at the limit of our resolution ($5''$), although we cannot eliminate the possibility of two cores along the line of sight. However, the Gaussian fits in Table 3.2 (emission + absorption) describe the line feature of core 3 considerably well and provide an explanation to the double-peaked spectrum as coming from one core and showing self-absorption. Moreover, the absorption is close to the systemic velocity (Fontani et al., 2009) strengthening the evidence for self-absorption. However, it is important to note that the negative components in the map are not causing the self-absorption dip as the negative components seen in Fig 3.1 are not relevant in the box of core 3. To be more specific, we carefully examined the channel maps and there are only few negative contours in the channel

where the deepest dip occurs (in the velocity of $\sim$ -17 km/s). Also, we mapped with short-spacing data removed and only very few negative contours remained, and the deep dip is still seen. As a result, the negative contours cannot be the main cause of the dip.

The double-peaked spectrum of core 3 shows one of the typical characteristics of gas infall motions: an optically thick transition (CS($2-1$) in our case) produces a blue-shifted, asymmetrical profile and central dip, with the blue-shifted line brighter than the red-shifted line (e.g., Zhou et al., 1993; Choi et al., 1995). This double-peaked feature is due to a temperature gradient and velocity gradient between each layer in a collapsing core (e.g., $v(r) \sim r^{-0.5}$ for the inside-out model) with a static envelope producing the central self-absorption dip. The blue-shifted line comes from the back side of the core and the red-shifted line from the front of the core. The lines with higher critical density and higher excitation temperature near the center will be obscured by the nearby lines with lower critical density and excitation temperature in the red peak, resulting in a stronger blue peak than red peak (Evans, 1999). In this case of I05345, optically thin lines peak in the dip of the self-absorbed lines. The absorption peaks approximately at the systemic velocity, also verified by optically thin tracers measured by Fontani et al. (2009).

Similar double-peaked profiles have been observed in CS($2-1$) for different objects (e.g., Choi et al., 1995; Tafalla et al., 1998; Belloche et al., 2002). However, the separation between the blue peak and the red peak in our observation is significantly larger ($\sim$ 3 km/s) than the separation in these studies ($\leq$ 1 km/s). This broad separation may arise from the larger infall velocity for intermediate mass to massive protostars (e.g. Xue & Wu, 2008). The absorption feature in the envelope may also affect the separation of the two peaks. In addition, similar double-peaked profiles can be produced by a rotating core (Pavlyuchenkov et al., 2008). Detailed fitting with radiative transfer models is necessary to better understand other dynamics effects (turbulence, rotation etc.) in double-peaked profiles (Belloche et al., 2002).

Although core 2 also shows two peaks in the spectrum, the nature of core 2 is less understood. The asymmetry in the spectrum of the two peaks is not significant, indicating that the gas is less likely to be infalling. The dip is close to the systemic velocity, suggesting that the double-peaked feature may be caused by the self-absorption, while the fidelity of core 2 may be affected by the interferometric effect.

3.4.2 Dynamics of Cores

Compared with the line widths for cores in other low-mass star forming regions (e.g., Onishi et al., 2002), we observe relatively large line widths from 1.5 km/s to 3.9 km/s for these seven cores. The isothermal sound speed for a region with a temperature 20 K is $\sim$ 0.27 km/s, much smaller than the observed line widths. Therefore, other non-thermal motions play a large role in the observed broad line widths. There are two possibilities for this non-thermal line-broadening (Saito et al., 2006). One possibility is that these cores formed from rather turbulent gas and still are turbulent. The other explanation is that the lines are broadened by interactions with the outflow or stellar wind from central protostars.

If initial large internal motions played a role in forming cores, higher density is necessary for a core to bind the system with gravitational energy. Saito et al. (2006) suggested such a possible correlation between line widths and the average H_2 density: the larger the line width, the higher the average density. Here we did not take the overall line widths of core 2 and 3 into consideration since their line widths may be affected and broadened by infall motions as discussed above. We see a weak trend (density vs. line widths) between core 1, 6 and 7. The line widths and average H_2 density of core 1, 6 and 7 are 2.63$\pm$0.01, 0.85$\pm$0.05, 1.58$\pm$0.01 km/s and (1.28$\pm$0.47)$\times 10^6$, (0.61$\pm$0.70)$\times 10^6$, $(1.04 \pm 0.26) \times 10^6$ cm^{-3}, respectively. However, considering the large uncertainties in the data, the positive trend is less obvious and it is not clear about the role of the initial turbulence to the formation of the cores in this region from our data.

Core 4 and 5 do not follow the relation between the averaged density and line widths. Fontani et al. (2009) detected an outflow oriented in the west-east direction possibly driven by the 226 GHz continuum source C1-b or C1-a, which corresponds to our core 3. The same paper also indicated that this outflow is probably interacting with the southern portion of the highly deuterated condensation N, which corresponds to our core 4, and causes the observed broad lines. Therefore, the line width of core 4 is more possibly influenced by the interaction with the outflow. The red-wing emission of core 4 and the blue-wing emission of core 6 may result from the red and blue lobes of the outflow. Nevertheless, it is less clear about the mechanism for core 5 to produce the observed spectrum.

However, it seems that the gravitational energy is not enough to bind the systems. The derived virial masses are noticeably larger than the LTE masses except for core 6 (see Table 3.3). Wang

et al. (2008) studied low to intermediate mass cores around MWC 1080 with CS(2-1) and obtained similar LTE masses (calculated from the same method as described in Section 3.3.1) and virial masses. Saito et al. (2006) also concluded that non-turbulent cores have a similar virial mass to LTE mass but that the virial masses are usually larger than the LTE masses for turbulent cores. The line width of core 6 is similar to that of non-turbulent cores ($\sim$ 0.90 km/s average) and the similarity between its virial and LTE mass indicates that this core is bound by gravitational energy. On the other hand, for cores with a larger virial mass than LTE mass, external pressure must be applied to maintain a bound core. The virial equilibrium with an external pressure (by neglecting magnetic fields and rotation) can be expressed as:

$$0 = 2U + \Omega - 4\pi R^3 P_{ex} \ ,$$

where U=$\frac{1}{2}M\sigma^2$ (σ: velocity dispersion) is the kinetic energy and $\Omega = -\frac{3}{5}\frac{GM^2}{R}$ is the gravitational energy. The results of P_{ex} is listed in Table 3.3. Except core 6, which is already gravitationally bound, other cores need an external pressure $P_{ex}/k \sim 10^8$ K cm^{-3} to help maintain the structure of the cores. With the choice of higher molecular abundance by one order of magnitude, the external pressure needed to maintain the cores would decrease to $\sim 10^7$ K cm^{-3}. Observations have shown that such pressure is observed in several massive star-forming regions (e.g., McKee & Tan, 2003, and references therein). Therefore, we suggest that these turbulent cores with larger kinetic energy may still be bound by the external pressure. In the case of I05345, the high external pressure may result from the nearby infrared cluster (Klein et al., 2005) which heats up the surrounding medium.

3.4.3 Implication for Massive Star Formation

We suggest that core 3 and core 1 are young stellar objects. They show many indicators of high-mass star formation. Since young stellar objects are surrounded by dust and gas, they are not able to be revealed by optical observations (and shorter wavelength observations) due to dust extinction. Consequently, YSOs are often identified by their IR emission excess. The detection in the Spitzer 24 μm band is often an indicator of YSOs (e.g., Caulet et al., 2008). We observed an infrared counterpart of core 3 and 1 in the Spitzer image (Paper II), implying that both cores contain warm dust, suggestive of a YSO candidate. In addition, the CS spectrum of core 3 shows the typical

signature of infalling gas motion — a double-peak feature with the stronger blue-shifted emission than the red-shifted emission. The wide separation of the two peaks (~ 3 km/s) is probably due to the higher masses.

Gas infall is also suggested by fitting the core's SED with a radiative-transfer model in the companion paper (Paper II). The radiative-transfer modeling indicates that cores 3 and 1 could be an accreting stellar source with the central stellar mass of $\sim 5\,M_{\odot}$ surrounded by an envelope with a mass of order of $10\,M_{\odot}$ (mass estimates in this paper for core 3: $11\,M_{\odot}$ (dust mass), $17\,M_{\odot}$ (LTE mass) and core 1: 4 $M_{\odot}$ (LTE mass), 18 $M_{\odot}$ (dust mass)).

Although, the virial masses (20 and 50 $M_{\odot}$ for core 1 and 3, respectively) are large compared to the LTE masses (4 and 20 $M_{\odot}$), indicating that the cores may be gravitationally unbound, the cores can still be bound through the support of the external pressure. Therefore, core 3 and 1 are possibly accreting the envelope to form a star and potentially becoming a massive star ($M_{*} > 8\,M_{\odot}$).

According to the classification of evolutionary stages of individual high-mass stars in Beuther et al. (2007a), the formation of massive stars start with High-Mass Starless Cores (HMSCs) and then form High-Mass Protostellar Objects (HMPOs) via harboring or accreting low/intermediate-mass protostars. HMPOs are accreting high-mass protostars with masses larger than 8 $M_{\odot}$, and consist of Hot Molecular Core (HMC), Hypercompact HII regions (HCHIIs, size ≤ 0.01 pc) and Ultracompact HII regions (UCHII regions, size ≤ 0.1 pc) at their early phases. Given the sizes of core 1 and core 3 (0.06 pc $\sim$ 0.08 pc) and the fact that the spectra of core 1 and 3 still peak in the far-infrared and have not approached near-infrared regimes, we suggest that these two cores are possibly on their way to become HMPOs.

Also, our cores are consistent with the massive star formation model proposed by McKee & Tan (2003). The theory states that turbulent cores in massive star-forming regions with pressure P_{ex} $\simeq 10^{8} \sim 10^{9}$ K cm^{-3} can be gravitationally bound and form stars with high accretion rates (10^{-3} $M_{\odot}$ yr^{-1}) in a short time scale (several times the free-fall time). Our cores appear to be turbulent and non-thermal with line widths ranging from 1.5 km/s to 3.9 km/s. However, while the positive correlation between the line widths and average H_2 density implies that the initial turbulence may also influence the formation of these cores, such correlation is not obvious in our data considering the uncertainties. For core 3 and 4, the broad line widths may be also contributed by the outflow driven by core 3. With the exception of core 6, the cores have a larger virial mass than LTE mass.

With the help of external pressure in the parent cloud, these turbulent cores can be bound and have the potential to become seeds for collapse in the future.

3.5 Summary

Identifying protocluster members and understanding their dynamics are the first step to study the initial conditions preserved in the parental clouds and further unveil the process of star formation. In this paper, we present observations of the intermediate/high mass star forming region IRAS 05345+3157. The observations have been performed in the line transition CS$(2-1)$ with CARMA D array. At this line frequency, we also observed the continuum emission at $\lambda = 2.7$ mm. With our observation, our main conclusions are as follows.

1. There are seven CS cores identified in the CS moment map. Both core 1 and core 3 have counterparts in the 2.7 mm continuum data (MM1 and MM3).

2. The LTE mass of all the cores are calculated based on the CS(2-1) data. The LTE masses range from ~ 2 $M_\odot$ to ~ 15 $M_\odot$ for all the cores. The LTE mass for core 1 is 5 ± 1 $M_\odot$ and that for core 3 is 15 ± 7 $M_\odot$. In addition, dust masses are estimated from the continuum data: core 1 has the dust mass of 18 ± 6 $M_\odot$ and core 3 has the dust mass of 11 ± 3 $M_\odot$.

3. Most of the spectra of the seven cores show a single peak. Core 3 shows a double-peaked spectrum with the blue emission stronger than the red emission, suggesting infall motion of gas.

4. Core 1 and 3 are suggested to be intermediate- to high-mass protostellar candidates.

5. The linewidths for the cores are larger than the thermal linewidth at 20 K. The broad linewidth of core 3 and 4 are probably contributed by the outflow driven by core 3 (Fontani et al., 2009). However, the role of the initial turbulence to the formation of the cores is not clear by examining the correlation between the linewidths and average H_2 density with the uncertainties.

6. These cores require an external pressure of $\sim$ 10^8 K cm^{-3} to keep them bound. Such high pressure is common among massive-star forming regions (e.g., McKee & Tan, 2003), suggesting that these cores are possible seeds for future star formation.

Table 3.1: Parameters of the identified cores

Label	R.A. (J2000.0)	Dec. (J2000.0)	a_0 (arcsec)	b_0 (arcsec)	P.A.$_0$ (deg)	a (arcsec)	b (arcsec)	P.A. (deg)	R (10^{-2} pc)
Core 1	05:37:53.03	31:59:34.9	12.0 ± 1.6	6.9 ± 0.6	$+83.5 \pm 5.3$	10.9 ± 1.8	4.9 ± 0.8	78.8	3.2 ± 0.4
Core 2	05:37:51.67	31:59:53.0	8.8 ± 2.2	7.5 ± 1.7	-25.4 ± 55.6	7.2 ± 2.4	5.5 ± 2.3	-3.7	2.7 ± 0.7
Core 3	05:37:52.19	32:00:05.4	12.3 ± 3.9	8.9 ± 1.5	$+63.9 \pm 27.3$	11.4 ± 4.2	7.0 ± 1.9	58.8	3.9 ± 0.9
Core 4	05:37:52.58	32:00:06.5	11.8 ± 4.0	7.4 ± 1.2	-83.6 ± 14.9	10.5 ± 4.5	5.9 ± 1.5	-88.3	3.4 ± 0.9
Core 5	05:37:55.14	31:59:57.0	12.3 ± 2.6	8.1 ± 1.0	$+48.2 \pm 17.2$	11.5 ± 2.8	5.9 ± 1.4	45.6	3.6 ± 0.6
Core 6	05:37:50.39	32:00:01.0	11.8 ± 7.9	6.8 ± 1.3	-14.2 ± 20.7	10.7 ± 8.7	4.6 ± 1.9	-9.3	3.1 ± 1.4
Core 7	05:37:50.64	32:00:06.3	11.1 ± 0.9	7.7 ± 0.4	$+37.2 \pm 7.7$	10.3 ± 1.0	5.1 ± 0.6	36.0	3.2 ± 0.2

a_0, b_0 and P.A.$_0$ are the observed major axis, minor axis and position angle of the cores. a, b and P.A. are the deconvolved major axis, minor axis and position angle. R is the equivalent radius, $\sqrt{ab}/2$.

Table 3.2: Fitting Parameters For Cores

Label	Amplitude Jy/beam	Peak Position km/s	FWHM km/s
Core 1	0.704 ± 0.002	-16.592 ± 0.004	2.626 ± 0.009
Core 2	2.008 ± 0.380	-18.065 ± 0.004	1.987 ± 0.053
	-2.040 ± 0.379	-18.071 ± 0.004	1.480 ± 0.045
Core 3	1.749 ± 0.032	-17.659 ± 0.005	3.237 ± 0.018
	-1.524 ± 0.031	-17.441 ± 0.003	1.735 ± 0.016
Core 4	0.699 ± 0.003	-19.894 ± 0.006	2.983 ± 0.015
Core 5	0.337 ± 0.002	-19.172 ± 0.012	3.940 ± 0.029
Core 6	0.922 ± 0.047	-17.832 ± 0.021	0.849 ± 0.049
Core 7	0.921 ± 0.003	-17.600 ± 0.003	1.584 ± 0.007

Table 3.3: Physical Properties of CS Cores

Label	I_t (Jy/beam km/s)	τ	N_{CS} ($\times 10^{13}$ cm^{-2})	n_{H_2} ($\times 10^{6}$ cm^{-3})	Σ_{H_2} (g cm^{-2})	M_{LTE} ($M_\odot$)	M_{vir} ($M_\odot$)	P_{ex}/k (K cm^{-3})
Core 1	1.94 ± 0.01	0.24	6.12 ± 0.03	1.28±0.47	0.20 ± 0.00	5.3 ± 1.2	26.8 ± 3.4	2.28×10^{8}
Core 2	1.02 ± 1.00	0.21	3.17 ± 3.11	0.59±0.53	0.11 ± 0.10	2.0 ± 2.3	13.2 ± 3.4	0.84×10^{8}
Core 3	3.30 ± 0.13	0.46	11.55 ± 0.46	1.69±1.11	0.39 ± 0.02	14.8 ± 6.8	49.8 ± 11.5	4.97×10^{8}
Core 4	2.19 ± 0.01	0.27	7.01 ± 0.03	1.22±0.81	0.23 ± 0.00	7.0 ± 3.5	37.1 ± 9.7	3.24×10^{8}
Core 5	1.39 ± 0.01	0.20	4.29 ± 0.03	0.74±0.40	0.14 ± 0.00	4.7 ± 1.6	67.9 ± 11.4	3.46×10^{8}
Core 6	0.82 ± 0.06	0.36	2.73 ± 0.20	0.61±0.70	0.09 ± 0.01	2.2 ± 2.0	2.7 ± 1.3	0.06×10^{8}
Core 7	1.53 ± 0.01	0.38	5.15 ± 0.03	1.04±0.26	0.17 ± 0.00	4.4 ± 0.7	9.6 ± 0.6	0.56×10^{8}

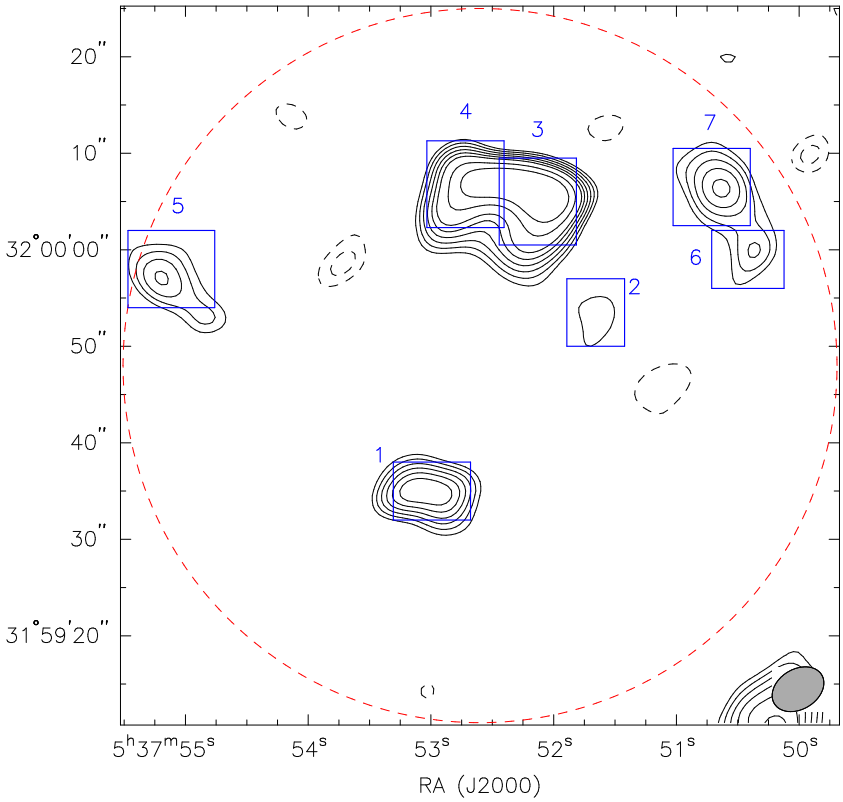

Figure 3.1: Contour map of CS $J = 2 - 1$ integrated intensity with the FWHM beam size shown in the lower right corner. The dashed circle is the size of the primary beam of the 10-meter dishes. The synthesized beam size, shown in the right-bottom corner, is $4.3'' \times 5.9''$with P.A.=-57.5°. The noise is 0.25 Jy beam^{-1} km s^{-1}, and the contours are 5σ, 6σ, 7σ, 8σ, 9σ, 10σ, 12σ, 14σ, positive and negative. The boxes are drawn based on the 3σ detections and are used to define cores.

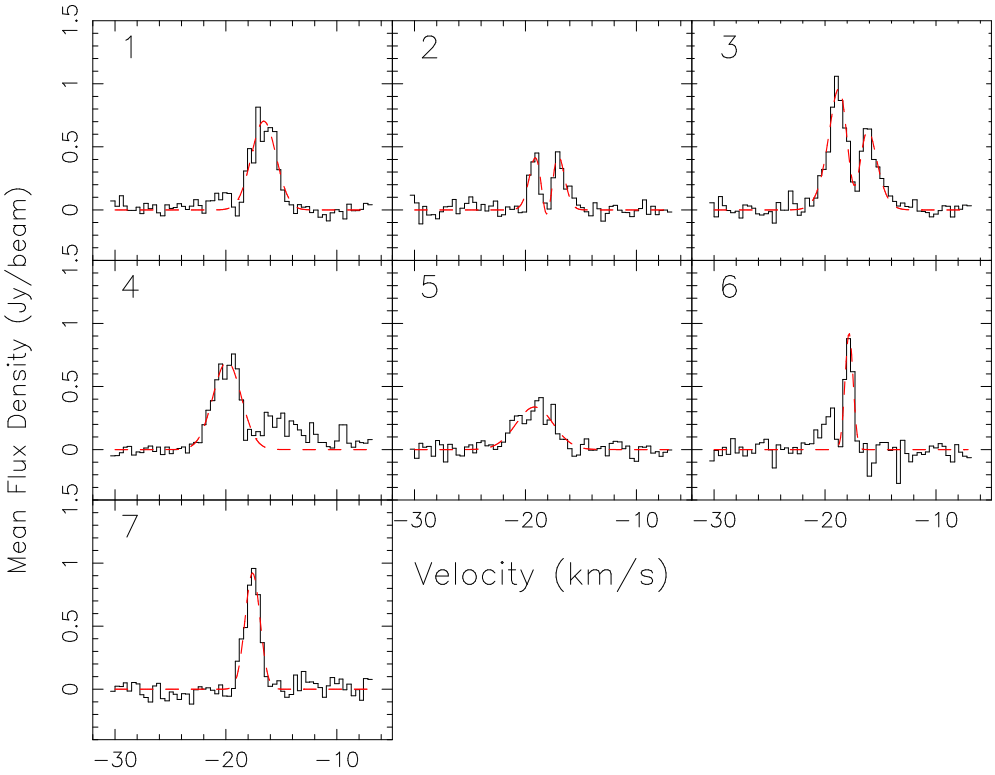

Figure 3.2: Spectra of identified CS cores. V_{LSR} is -18.6 km/s. The dashed lines are the best fit Gaussians.

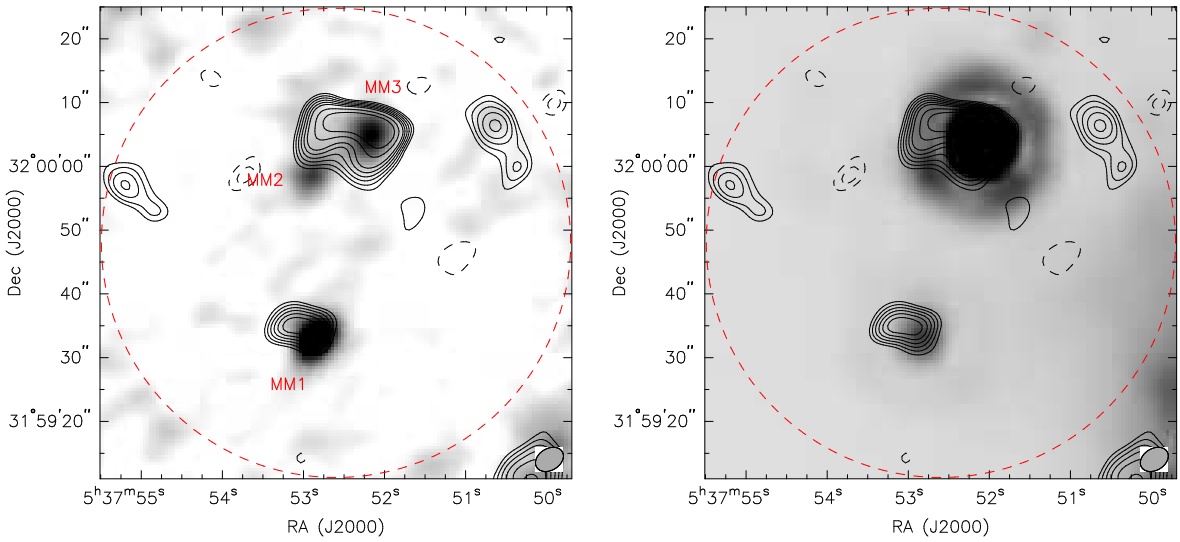

Figure 3.3: Left panel: CS$(2-1)$ emission overlaid on the gray-scale 2.7 mm continuum data. The contours represent the CS integrated intensity with the same contour levels with Fig. 1. Right panel: CS$(2-1)$ emission overlaid on the gray-scale Spitzer 24 μm data. The contours are the same as in the left panel.

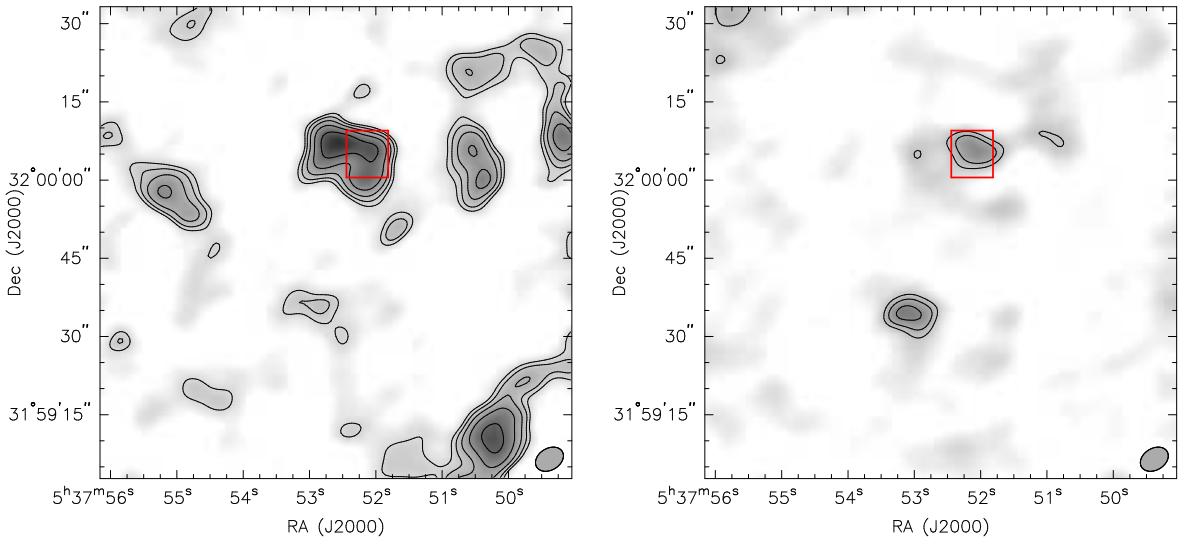

Figure 3.4: Maps of CS $(2-1)$ integrated intensity of the blue and red part of the self-absorbed line of core 3. Left panel: The map of the blue emission peak. The integrated velocities range from -21.6 km s^{-1} to -17.5 km s^{-1}. The contour levels start from 5σ (σ = 0.12 Jy beam^{-1}) and end at 28.3σ with a logarithmic step of $\log(\sqrt{2}\sigma)$. Right panel: The map of the right emission peak. The integrated velocities range from -17.1 km s^{-1} to -14.9 km s^{-1}. The contour levels also start from 5σ (σ=0.18 Jy beam^{-1}) and end at 28.3 σ with a logarithmic step of $\log(\sqrt{2}\sigma)$. The negative contours are not shown for simplicity.

Chapter 4

Earliest Stages of Protocluster Formation: Substructure and Kinematics of Starless Cores in Orion

4.1 Introduction

Star formation involves a complicated interplay between turbulence, magnetic fields, and gravity. While the understanding of low-mass star formation has advanced over decades (e.g., McKee & Ostriker, 2007), that of massive star formation has progressed more slowly. One difficulty is that massive protostars generate a much stronger radiation pressure that can strongly modify the gas accretion in the formation process (see Zinnecker & Yorke, 2007). Another is that massive stars appear to form in crowded environments of clusters (Lada & Lada, 2003). This study aims to understand the conditions for massive star formation and their clustered environment at early stages.

There are two main competing scenarios in massive star formation. One of them is the "turbulent core model" proposed by McKee & Tan (2003). In this model, the core is supported by supersonic turbulence and evolves on several free-fall timescale. The turbulent core is in quasi-static equilibrium and the formation of massive stars is a scaled-up version of low-mass star formation. The final mass of a massive star is determined by the mass of its natal core and the stellar environment is unimportant. The high pressure caused by supersonic turbulence results in high accretion rate ($> 10^{-3}$ $M_\odot$ yr^{-1}), overcoming the radiation pressure and continuing accretion process. In this model, the collapse is envisioned to be more or less monolithic, with a relatively low level of fragmentation.

Alternatively, Bonnell et al. (2004) and Bonnell & Bate (2006) proposed that massive star formation is a dynamical process that involves competitive accretion. In a core that is dominated by supersonic turbulent motions, significant density fluctuations are generated due to turbulent support, with gravity taking over in the densest regions. Stellar seeds are created through this

"turbulent fragmentation" and eventually lead to clusters. Massive stars form from the seeds located near the center of the cluster where the gravitational potential is deepest; these seeds win the competition for the reservoir of gas to grow to the highest masses. In this scenario, the final mass of a massive star is strongly influenced by their environment and has little correlation with the initial mass of the natal core.

A major difference of the two scenarios, which can be tested observationally, is the level of fragmentation. The turbulent core scenario envisions the existence of one massive starless core, while the competitive accretion scenario requires a higher level of fragmentation in massive starless cores. Therefore, our goal is to study the fragmentation in starless cores, the earliest stage of star formation where the initial conditions for massive star formation are still kept, and to provide insight to the formation of massive stars.

Due to angular resolution limitations, only recently has the study of fragmentation in starless/prestellar cores made significant progress. Lately, a number of studies toward massive star-forming regions with high angular resolutions using interferometers have begun to reveal fragmentation in massive starless cores on 0.1 pc scale (Bontemps et al., 2010; Palau et al., 2013). These studies mostly focus on the massive star-forming sites associated with Infrared Dark Clouds (IRDCs), which are typically at a distance of few kilo-parsecs. We chose Orion as our target region. At a distance of 414 pc (Menten et al., 2007), Orion is the closest active star-forming region that contains massive stars (e.g., Hillenbrand, 1997; Hillenbrand & Hartmann, 1998; Johnstone & Bally, 1999) as well as massive starless cores (e.g., Nutter & Ward-Thompson, 2007; Di Francesco et al., 2008; Sadavoy et al., 2010). It provides an excellent opportunity to study the initial conditions for massive star formation.

4.2 Observations and Data Reduction

To fully investigate the substructure and kinematics of starless cores, we carried out both single-dish and interferometric observations with the molecular line CS(2-1), an extensively used tracer for high-density gas. Although previous studies indicated that C-bearing species may be depleted during the prestellar phase (e.g., Taylor et al., 1998), several studies have also suggested that associated C-bearing molecules have not been frozen out at the very early stage of star formation.

The single-dish observations were performed with the IRAM 30 m telescope, and the interferometric observations were carried out with the Combined Array for Research in Millimeter-wavelength (CARMA).

4.2.1 The sample

Our sample of starless cores were chosen from Nutter & Ward-Thompson (2007). They conducted a large survey in Orion at 850 μm dust continuum with the Submillimetre Common User Bolometer Array (SCUBA). By comparing the survey with the *Spitzer IRAC* catalog, the study provided a complete catalog of prestellar cores and protostellar cores down to the lower completeness limit at $\sim$ 0.3 $M_\odot$ in the Orion A North, A South, Orion B North and B South regions. We randomly chose sixteen prestellar cores from the catalog with the dust-derived masses[1] ranging from 1 $M_\odot$ and 50 $M_\odot$ to be observed with the IRAM 30 m telescope. The reason to include a few cores with low dust-derived masses was to compare them with massive cores; nevertheless, some cores with low dust-derived masses turn out to be massive from our observations (see Sect. 4.3.1). Figure 4.1 shows the positions of the detected cores with the IRAM 30m telescope. Table 4.1 lists the coordinates of the sources, and the masses calculated from the 850 μm observations. The CARMA observations were performed toward eight of the nine starless cores that had been detected with the IRAM observations.

The cores are mostly located in the filamentary structures around the periphery of the central Orion Molecular Cloud 1 (OMC-1). Core 1 and Core 3 are in the Orion Bar photon-dominated (PDR) region (e.g., Lis & Schilke, 2003). Core 2 and Core 4 are associated with the "radiating filaments" (Johnstone & Bally, 1999) from OMC-1 of which the formation mechanisms are still unclear (Myers, 2009). In particular, Core 4 is close to the Orion BN/KL region which is observed with powerful outflows and "H_2 fingers" (Zapata et al., 2009; Peng et al., 2012); however, the location of Core 4 is in a larger spatial scale and not associated with the HH bullets or H_2 fingers (Buckle et al., 2012). Core 7 and Core 9 are associated with a filament north-east to OMC-1 which is suggested as a region associated with PDR (Shimajiri et al. 2013, in prep).

[1]The term "dust-derived mass" used in this paper refers to a total mass from dust and gas derived from dust emission by assuming a gas-to-dust ratio (typically 100).

4.2.2 IRAM 30-m observations

The observations were performed in August 2010 toward sixteen starless cores in Orion chosen from the catalog in Nutter & Ward-Thompson (2007). The hetrodyne receiver EMIR was used. The bands E090, E150 and E230 in combination captured various lines. The bands E090 and E150 were used to perform the molecular line observations with CS(2-1) at 97.980968 GHz, $C^{34}S$(2-1) at 96.41298 GHz and CS(3-2) at 146.96905 GHz. We used VESPA as the spectral back-end with a spectral resolution of 40 kHz (~ 0.06 km s^{-1} at 3 mm) and a total bandwidth of 80 MHz. On-the-fly mapping was performed with both horizontal and vertical scanning to span an area of about $2'$ by $2'$ for each source. The observations were performed in position-switching mode with off-position at $05^h36^m15.0^s$, $-05\,\mathrm{deg}\,02'34''$ (Ikeda et al., 2007). Calibration scans were taken about every fifteen minutes. The pointing was checked every two hours. The beam size (full-width half-power) is $\sim$25.5″at the frequency of CS(2-1) and $C^{34}S$(2-1), and 17″ at the frequency of CS(3-2). The beam efficiency[2] (Beff) is 81% for CS(2-1) and $C^{34}S$(2-1), and 74% for CS(3-2).

The data reduction was done with the CLASS package from the GILDAS[3] software. All the data are re-gridded to have at least three pixels in one beam size. All sixteen sources were observed with CS(2-1) and ^{12}CO(2-1); only nine of which showed detections. Table 4.2 lists the molecular lines observed towards these nine cores.

4.2.3 CARMA observations

CARMA is a heterogeneous array combining three types of antenna: six 10-meter antennas, nine 6-meter antennas and eight 3.5-meter antennas. The data presented in this paper used the cross-correlated data from the 10-meter antennas and the 6-meter antennas. The CARMA observations were performed toward eight starless cores out of the nine sources detected by the IRAM 30-m telescope between May 2010 and November 2011. Only one source (core 8) out of the eight observed sources was observed with both the D and E array configuration, and the remaining seven cores were observed with only the D array. The data presented in this paper focus on CS(2-1) at 97.98096 GHz, with one band for the continuum observation. The projected baselines of the D array range from 11 m to 150 m, providing sensitivity to spatial scales up to $\sim 28''$ and a synthesized

[2]See http://www.iram.es/IRAMES/mainWiki/Iram30mEfficiencies
[3]See http://www.iram.fr/IRAMFR/GILDAS/

beam of $\sim$ 5″ at 3 mm. The E array has projected baselines ranging from 8 m to 66 m, providing sensitivity to spatial scales up to $\sim$ 40″ and a synthesized beam of $\sim$ 7″ at 3 mm. The spectral resolutions are 0.15 km s^{-1} for core 1, 2, 4, 5 and 0.06 km s^{-1} for core 3, 6, 7, 8. The amplitude calibration is estimated to be 10%, and the uncertainties discussed afterwards are only statistical, not systematic. All the data reduction were done with the MIRIAD software (Sault et al., 1995).

4.2.4 Herschel and JCMT archival data

We also present the 500 μm image of the Orion A-North region from the *Herschel* archival data as well as the 850 μm image from the JCMT archival data. The *Herschel* 500 μm image is downloaded from the Herschel Science Archive[4] (HSA). The data were taken in September, 2009 with the Spectral and Photometric Imaging Receiver (SPIRE). The observation identifier number is 1342184386, and the data presented in this paper is calibrated to level 2. The 850 μm image from JCMT is downloaded from the site of public processed data in the JCMT science archive[5]Ṫhe project number is M09BI121 and the data were taken in Feb, 2010.

4.3 Results and Data Analysis I: Morphology and Properties

4.3.1 IRAM maps

CS(2-1), CS(3-2) and C^{34}S

As described in Sect. 4.2.1, we chose sixteen cores from the SCUBA survey to perform observations with the IRAM 30-m telescope, and only nine cores out of the sixteen cores were detected. We examined the *Spitzer* 8.0 μm maps and the IRAM CO data (^{12}CO(2-1), ^{18}CO(2-1)) to confirm that these are indeed starless cores that lack infrared counterparts and outflows.

Table 4.2 shows that H^{13}CO$^+$(1-0) and N_2D^+(2-1) are not detected towards any core. A classification between "early-time" and "late-time" molecules have been suggested by several studies based on the time at which these molecules reached their peak abundance (e.g., Taylor et al., 1998; Morata et al., 2003). CS(2-1) is in general classified as an "early-time" tracer while H^{13}CO$^+$(1-0) and nitrogen-bearing species are "late-time" tracers (e.g., Morata et al., 2005). Therefore, the

[4]See http://herschel.esac.esa.int/Science_Archive.shtml
[5]See http://www.cadc.hia.nrc.gc.ca/jcmt/search/product/

detection of CS(2-1) and the non-detections of $H^{13}CO^+$(1-0) and N_2D^+(2-1) in core 1, 2, 3, 5 suggest that the cores are in the very early stage of the evolution and are chemically young, before the depletion of CS(2-1) becomes significant (e.g., Tafalla et al., 2002). However, the detail of the chemistry depends on various models (e.g., Vasyunina et al., 2012).

Figure 4.2 shows the 0^{th} moment maps from the IRAM CS(2-1) observations for the nine cores and compares the CS(2-1) emission with the deconvolved core sizes derived from the 850 μm dust emission from the SCUBA survey (Nutter & Ward-Thompson, 2007). The color scale and contours show the CS(2-1) data from IRAM, and the green dashed lines indicate the definitions of cores from the 850 μm survey. The 850 μm dust-derived masses reported in Table 4.1 are calculated based on the 850 integrated flux density within the green ellipses (Nutter & Ward-Thompson, 2007). As shown in the figure, the CS(2-1) emission is detected near the positions of the cores defined by the 850 μm observations. However, several of the 850 μm cores mismatch the morphologies traced by CS(2-1) (core 1, 4, 5, 7), and several show discrepancies in the areas of emission (core 2, 8). The inconsistency suggests that dust and gas traced by CS(2-1) are not well correlated in the early stage of star formation (Morata et al., 2012).

Figure 4.2 shows that the IRAM CS(2-1) sources are mostly single-peaked emission, and are usually associated with non-spherical, elongated structures. The non-spherical morphologies agree with previous studies of dense cores, which showed that the majority of dense cores are tri-axial including prolate or oblate (e.g., Tassis, 2007). Figure 4.3 shows the 0^{th} moment maps from the IRAM CS(3-2) and $C^{34}S$(2-1) data compared with the CS(2-1) data for the five cores which are detected. CS(3-2) and $C^{34}S$(2-1) are in general optically thinner than CS(2-1). These three lines show consistent morphologies, and the CS(3-2) peaks coincide well with the CS(2-1) peaks. There are a few differences; for example, the $C^{34}S$(2-1) emission shows more than one peak for core 2, but shows only one peak for core 8. Both CS(3-2) and $C^{34}S$ show more spherical shape of the core than the CS(2-1) emission.

CS(2-1) column densities

We estimate the optical depths and peak column densities of CS(2-1) based on the CS(2-1) and $C^{34}S$(2-1) emission. We first estimate the optical depths of CS(2-1) and $C^{34}S$(2-1) by

$$\frac{T_{MB}(C^{34}S)}{T_{MB}(CS)} = \frac{1 - exp(-\tau)}{1 - exp(-\tau f)}, \tag{4.1}$$

where T_{MB} is the main beam temperature of the molecular line, and f is the CS to $C^{34}S$ ratio. T_{MB} is calculated from the observed antenna temperature divided by the main beam efficiency (0.8 as reported in Sect. 4.2.2). T_{MB}(CS) and T_{MB}($C^{34}S$) are measured from the flux within the beam size centered at the CS(2-1) peak emission. The measured values for T_{MB}(CS) and T_{MB}($C^{34}S$) are listed in Table 4.3. We use 22.5 for the the CS to $C^{34}S$ ratio, assumed to be the terrestrial value (e.g., Kameya et al., 1986). We further estimate the excitation temperature from the radiative transfer equation

$$T_{ex} = \frac{h\nu}{k}\left[ln\left(\frac{h\nu/k}{\frac{T_{MB}}{1-e^{-\tau}} + J_\nu(T_{bg})} + 1\right)\right]^{-1},$$

where $J_v(T) = \frac{h\nu/k}{e^{h\nu/kT} - 1}$, ν is the frequency of the molecular transition, and T_{bg} is the background temperature assumed to be 2.73 K. With the assumption of LTE, the column density then can be calculated from

$$\begin{aligned}\left[\frac{N}{\mathrm{cm^{-2}}}\right] =& 1.67\times10^{14}\frac{Q_{rot}}{g_k g_I}\left[\frac{S_{JKI}}{\mathrm{erg\ cm^3\ statC^{-2}\ cm^{-2}}}\right]^{-1} \\ &\times\left[\frac{\mu}{\mathrm{D}}\right]^{-2} e^{Eu/T_{ex}}\left[\frac{\nu}{\mathrm{GHz}}\right]^{-1}\frac{J_v(T_{ex})}{J_v(T_{ex}) - J_v(T_{bg})} \\ &\times\frac{\tau}{1-e^{-\tau}}\left[\frac{\int T_{MB}dv}{\mathrm{K\ kms^{-1}}}\right].\end{aligned}$$

The parameters and their values used in the equation are listed in Table 4.4 (Rohlfs & Wilson, 2000). We assume an abundance ratio between CS(2-1) and H_2 at the center of a core to be 2×10^{-10} (the result from modeling in a later section) in converting the CS column densities to H_2 column densities. Using a constant abundance ratio instead of a profile with central depletion is justified since the cores are chemically less evolved (see Sect. 4.3.1). Frau et al. (2010) reported similar CS-to-H_2 abundance ratio (few times 10^{-10}) in the chemically young starless cores in the Pipe Nebula.

We further estimate the masses and number densities within the beam size ($25''$) for the cores

assuming sphericity:

$$M_{H_2} = \mu m_H D^2 \int N_{H_2} d\Omega,$$

$$n_{H_2} = \frac{M_{H_2}}{4\pi r^3/3},$$

where m_H is the hydrogen mass, D is the distance to Orion (414 pc from Menten et al. (2007)), and r is the radius of the beam. The derived values for the optical depths, excitation temperatures, column densities, and LTE masses at the peak positions are listed in Table 4.3.

The results show that the optical depths of CS(2-1) are between 2 to 5; similar optical depths for CS(2-1) are reported in other star-forming cores (Frau et al., 2010; Morata et al., 2003). The excitation temperatures range from 6.5 K to 19 K with the average temperature of 11.3 K, in agreement with the kinetic temperature of 10 K (to 15 K) for starless cores (e.g., Schnee et al., 2009). This suggests that the cores are thermalized; the thermalization is also suggested by the high number density (several times 10^6 cm^{-3}) compared to the critical density for CS ($\sim 10^5$ cm^{-3}; see Evans (1999)). The LTE masses indicate that these cores are massive star-forming regions. The LTE masses are not consistent with the dust-derived masses from the 850 μm observations, possibly due to the higher temperature (20 K) used in the dust-derived masses calculation, the assumed dust opacity, the imperfect coupling between dust and gas, and optical depth effects.

The derived column densities ($\geq 10^{23}$ cm^{-2}) are comparable to several massive star-forming regions (e.g., Beuther et al., 2007b) and are slightly higher than some intermediate mass-star forming regions (e.g., Lee et al., 2011). The number densities range from 4.7×10^6 to 3.7×10^7 cm^{-3}. The simulation performed by Keto & Field (2005) which includes hydrodynamics, radiative cooling, variable molecular abundance, and radiative transfer concludes that starless cores with central densities larger than a few times 10^5 cm^{-3} are dynamically unstable and may proceed to gravitational collapse, suggesting that our cores are gravitationally bound.

4.3.2 CARMA maps

CARMA CS(2-1) maps

Figure 4.4 shows the CARMA observations of CS(2-1) (red contours) overlaid on the CS(2-1) observations from the IRAM 30-m telescope (grey scale in the left panel), JCMT 850 μm dust

emission (grey scale in the middle panel), and the Herschel 500 μm dust emission (grey scale in the right panel). As seen in the figure, most of the cores (except core 5) show multiple intensity peaks in the CARMA CS(2-1) emission within the IRAM cores with single peaks, suggesting fragmentation. These fragments are not in spherical morphologies and are spatially connected to each other. The number of fragments range from three to five in each core. Core 5 is associated with one single object in spherical shape and does not show signs for fragmentation.

The CARMA CS(2-1) emission well traces the small-scale filamentary structures probed by the JCMT 850 μm observations and Herschel 500 μm observations. For example, core 1 is associated with the filamentary structure in the North-East and South-West direction as clearly seen in the 850 μm and 500 μm images. The tight connection between the structures probed by CS(2-1) and dust emission is reminiscent of the star formation activities along filamentary structures at large scales (see Lee et al., 2012), suggesting the importance of filamentary structures to star formation at small scales.

Figure 4.5 shows the comparison between the CS(2-1) fluxes from the IRAM observations and CARMA observations for the eight cores. The black lines indicate the IRAM fluxes and the red lines present the CARMA fluxes. To do this comparison, the CARMA maps are convolved with the beam size of the IRAM 30-m telescope (25″). For both IRAM and CARMA fluxes, the spectra are then extracted from the averaged flux within the lowest contour level for each core shown in Figure 4.3. Some of the cores (Core 1, 2, 4, 7 and 8) show that the CARMA fluxes are largely resolved out while the other cores (Core 3, 5 and 6) show comparable CARMA and IRAM fluxes. The largely resolved out fluxes with Core 1, 2, 4, and 8 may be associated with converging flows at larger scales (see Sect. 4.4.1).

CARMA N_2H^+(1-0) maps

N_2H^+(1-0) is detected only in core 4 and core 8 with CARMA while the other cores show no detections. Figure 4.6 shows the comparison between CARMA CS(2-1) and N_2H^+(1-0) for these two cores. The red contours are the N_2H^+(1-0) 0^{th} moment maps and the cyan contours are the CS(2-1) 0^{th} moment maps. The blue dashed lines indicate the IRAM CS(2-1) emission. For core 4, N_2H^+(1-0) shows multiple peaks with the strongest emission outside the IRAM contour. For core 8, N_2H^+(1-0) also shows two major peaks. Although the positions of N_2H^+(1-0) peaks do not well

coincide with the CS(2-1) peaks for both cores, N_2H^+(1-0) still shows the clumpy nature for these cores, suggesting that the fragmentation detected by optically thicker tracer CS(2-1) is not due to the chemical effect from depletion.

CARMA continuum maps at 3 mm

CARMA continuum observations at 3 mm showed no detections. The non-detection is reminiscent of the lack of 3 mm continuum emission in CARMA D array maps towards 9 starless cores in the Perseus molecular cloud Schnee et al. (2010). Lee et al. (2012) suggested that the non-detections are probably due to CARMA's sensitivity. Future observations with better sensitivity are required for further characterization on dust properties at millimeter-wavelengths. We calculated the mass sensitivity from the 3σ upper limit using the equation:

$$M = \frac{d^2 S_{3mm}}{B_\nu(T_D)\kappa_{3mm}} \tag{4.2}$$

where d is distance to Orion, S_{3mm} is three times the noise level, B_ν is the Planck function as a function of dust temperature T_D, and κ_{3mm} is the dust opacity. We use a typical dust temperature of 10 K for starless cores and 0.00169 cm^2 g^{-1} for κ_{3mm} (an extrapolated value from (Ossenkopf & Henning, 1994)) by assuming a gas-to-dust ratio of 100 and $\beta = 2$. The noise levels for the cores and the mass upper limits corresponding to 3σ are presented in Table 4.5. These mass limits are only for substructures and the large-scale emission is not detected.

4.4 Results and Data Analysis II: Kinematics

4.4.1 Large-scale Kinematics with IRAM

Velocity Gradients Fitting

Figure 4.7 shows the first moment maps from the IRAM CS(2-1) data for the nine cores. The maps are masked based on the CS(2-1) contours. As shown in the figure, velocity gradients are observed in several cores (core 1, 2, 4, 7, 8, and 9). To derive the magnitudes of the velocity gradients, we assume that the gradients are linear in both right ascension and declination direction. Using the first-moment maps, the velocity gradients are computed based on the method described in

Goodman et al. (1993), but with the MPFIT function (Markwardt, 2009) implemented in IDL performing the least-square fitting:

$$v_{LSR} = v_0 + a\Delta\alpha + b\Delta\delta, \tag{4.3}$$

where v_0 is the systematic velocity, a and b are the velocity gradients along the right ascension and declination, and $\Delta\alpha$ and $\Delta\delta$ are the position offsets in the right ascension and declination direction. The total velocity gradients are defined as

$$g = \frac{\sqrt{a^2 + b^2}}{D},$$

where D is the distance (414 pc for Orion). The direction of the velocity gradients is then defined as $\theta_g = tan^{-1}(\frac{b}{a})$.

The fitting results of the velocity gradients for all the nine cores are listed in Table 4.6. The total velocity gradients range from 1.4 to 12.1 km s^{-1} pc^{-1}, with the average value of 6.2 km s^{-1} pc^{-1}. Most of the velocity gradients are large compared to dense cores including starless cores and protostars (0.3 to 4 km s^{-1} pc^{-1} from Goodman et al. (1993) and 0.5 to 6 km s^{-1} pc^{-1} in Caselli et al. (2002)). Recent observations with higher resolutions have found larger velocity gradients. For example, Curtis & Richer (2011) found the velocity gradients of $\sim$ 5.5 km s^{-1} pc^{-1} for starless cores and $\sim$ 6 km s^{-1} pc^{-1} for protostars in Perseus. Also, Tobin et al. (2011b) found a median velocity gradient of 10.7 km s^{-1} pc^{-1} with several Class 0 objects from interferometric data.

These velocity gradients are often interpreted as rotation. However, the common interpretation of rotation needs to be treated with caution since an inflowing filament can also produce the velocity patterns that mimic rotation (Tobin et al., 2012a). Infall and rotation in spherical objects are easy to distinguish since spherical infall exhibits blue-skewed spectra with optically thick lines across the object (e.g., Lee et al., 1999; Pavlyuchenkov et al., 2008). However, infall and rotation in filaments are more difficult to disentangle as both generate velocity gradients. The spectral maps and position-velocity diagrams need to be examined carefully to correctly interpret the kinematics.

Spectral Maps

Figure 4.8 shows the IRAM 30-m spectral maps overlaid on the first-moment maps for core 1, core 2, core 4 and core 8. We chose these four cores to present because they have the most prominent velocity gradients. The separation between each spectral panel is $10''$. Shifts in the velocity peaks across the maps from blue-shifted to red-shifted velocity components are observed for each core. Figure 4.9 shows the spectral maps along the white lines shown in Figure 4.8 and present the shift more clearly. The white lines are determined by connecting the minimum and maximum velocities in the maps. The white star indicates the central position in the white lines.

In Figure 4.9, we notice two main features of the spectra across the cores. First, a gradual shift from blue to red in the peak velocities is observed across the cores as mentioned above. The separations between the blue-shifted and red-shifted peak velocities are ~ 0.8 km s^{-1} (core 1), 2.5 km s^{-1} (core 2), 1.6 km s^{-1} (core 4), and 1.7 km s^{-1} (core 8). The blue peaks and red peaks do not vary significantly across the cores, suggesting that the gas flows at a nearly constant speed. Second, the blue components have stronger intensities than the red components. These two features are observed for all four cores. To explain these two features, we performed a radiative transfer modeling with one of the cores, core 2.

Radiative Transfer Modeling

We compare the CS(2-1) spectra from core 2 with radiative transfer calculations performed with the code *LIME* (Line Modeling Engine; Brinch & Hogerheijde (2010)). The code calculates the emergent spectra by solving the molecular line excitation with 3D Delaunay grids for photon transport and accelerated Lambda Iteration for population calculations. The inputs to the code, which are based on 3D structures, are the density, temperature, chemical abundance, velocity, and linewidth profiles. Users also control parameters such as molecular lines, inclination angles, dust properties, and image resolutions.

To be consistent with the flattened morphologies of the cores observed with IRAM, we consider a cylindrically symmetric filament that contains inflowing[1]gas from the two sides to the center with an inclination angle. The model is illustrated in Figure 4.10. The density is considered to vary with the cylindrical R and Z to describe a flattened, filamentary structure. The density profile has the

form of $n(R,Z) = n_0/[1+(\frac{R}{R_0})^{\alpha}]/[1+(\frac{Z}{Z_0})^{\alpha}]$, where n_0, R_0 and Z_0 are constant. The power-law index α is taken to be 2.5 in the modeling, consistent with other starless cores (Tafalla et al., 2002, 2004). We varied n_0 with 3.0×10^6, 4.0×10^6, and 5.0×10^6 cm^{-3}; R_0 and Z_0 were varied with four sets of numbers respectively: (4180 AU, 17333 AU), (5513 AU, 30000 AU), (6180 AU, 35066 AU), and (10000 AU, 43333 AU).

The temperature is assumed to be a typical temperature of 10 K for starless cores (e.g., Schnee et al., 2009). For the CS(2-1) abundance, we have considered constant abundance ratios ([CS]/[H_2] = 10^{-9}, 3×10^{-10}, 2×10^{-10}) and a centrally depleted profile that has the abundance ratio of 10^{-11} in the center and 10^{-9} in the outer envelope. For the velocity field, we have considered two profiles in both the velocity fields that are along the Z-axis only. First, we considered constant velocities including 1.3 km s^{-1} and 1.5 km s^{-1}. Second, we considered a profile that has the form of Keplerian rotation: $v(Z) = v_0(Z/Z_c)^{-0.5}$, where Z_c is a constant to modulate the profile. v_0 was varied with 2.0 km s^{-1}, 3.0 km s^{-1}, and 4.0 km s^{-1}; Z_c was varied with 500 AU and 2000 AU. The line dispersion was considered with 0.5 km s^{-1} and 0.8 km s^{-1}. The inclination angles were tested with 18 degree, 45 degree, and 60 degree.

The best-fit gives a density profile of $n(R,Z) = 3.0 \times 10^6/[1+(\frac{R}{10000AU})^{2.5}]/[1+(\frac{Z}{43333AU})^{2.5}]$, a constant temperature of 10 K, a constant [CS]/[H_2] abundance ratio of 2.0×10^{-10}, a constant linewidth of 0.8 km s^{-1}, a constant inflow velocity of 1.5 km s^{-1}, and an inclination angle of 45 degree. The total reduced χ^2 is calculated to be 1.58. The red line in the spectra of Core 2 in Figure 4.11 shows the best-fit from the radiative transfer modeling. The top figure shows the result from the inflow model. The model has been convolved with the same beam size as the observational data.

The model successfully explains the two features we observed in the spectral maps. With an inclination angle, the gas flow further from observers becomes blue-shifted and the side closer to observers becomes red-shifted. Therefore, shifts of peak velocities between blue components to red components are observed. For an optically thick line such as CS(2-1), the emission produced in the blue-shifted side is closer to the symmetrical center (P1 in Figure 4.10) than the emission produced in the red-shifted side due to the projection (P2 in Figure 4.10). The spectral intensity is higher closer to the symmetric center since the excitation temperature is higher due to the density profile. As as result, we see the intensities in the blue-shifted side always larger than the red-shifted side.

The reason for this asymmetry is similar to the blue-skewed spectra for spherical infall (e.g., Evans, 1999). However, we stress that the central dip seen in the model shown at the center of the core is not caused by self-absorption. Instead, the dip is due to the overlapping between the two Gaussian velocity components. Self-absorption would occur at the inflow velocity for each of the velocity component; however, although CS(2-1) is optically thick ($\tau \sim 3$) for our cores, we do not observe self-absorptions.

As mentioned above, it is considerably challenging to distinguish between 2D inflow or rotation on a filament from observations (Tobin et al., 2012a). To examine the differences between the two compared with our data, we also performed the radiative transfer modeling on a cylindrically symmetric filament with rotation on the R- axis. All the profiles and parameters are the same as the best-fit model for filamentary inflow except for the velocity field. The velocity field we adopted is a constant velocity field along the line-of-sight since the two peaks of the red and blue components nearly stay constant and the best-fit for the inflow model gives a constant velocity. Therefore, the velocity field shows a profile of differential rotation where $\omega(z) \propto \frac{1}{z}$.

Figure 4.11 shows the spectra from the rotation model. The black lines are from the data of Core 2 and the red lines indicate the radiative transfer model. As shown in the figure, the model fails to describe not only the broad linewidth in the central position but also the "wing" features in the off-center positions. The χ^2 for the model is 1.8, larger than the inflow model.

In addition, we compare the position-velocity diagrams (PV diagrams) between the observational data, inflow model, and rotation model as shown in Figure 4.12. With the same angular resolution, the inflow model better demonstrates the observed discontinuity between the two velocity components. The data shows an encounter of two velocity components at the position of zero offset. Such a feature is clearly seen in the inflow model but not in the rotation model at all. In summary, we suggest that the inflow model describes the data much better than the rotation model as the dominating mechanism for the kinematics.

4.4.2 Small-scale Kinematics with CARMA

Figure 4.13 shows the first moment-maps with the CARMA CS(2-1) data. The maps are masked based on the 5σ contours in the zeroth moment maps (10σ for core 6 and core 8 to avoid too

[1]To distinguish from 1D spherical infall, we use the term "inflow" to describe gas infall on a 2D filament.

extended structures). The magenta contours indicate the IRAM CS(2-1) cores. Most of the cores, including core 1, 2, 3, 4, and 8, show similar behavior in the velocity patterns as the IRAM CS(2-1) results. For example, the global velocity gradients in core 1, 2, 4, and 8 are also observed in the CARMA data. However, the CARMA data show more complex structure in the velocity fields as CARMA is more sensitive to smaller scales. For some cores (Core 1, 3, 6, 7, and 8), the fragments are more obviously identified in the channel maps and have their own velocity components. In comparison, the fragments associated with Core 2 and 4 are more blended with each other in the channel maps.

4.5 Discussion

4.5.1 Hierarchical Fragmentation

Hierarchical fragmentation from large-scale molecular clouds (few parsecs) to star-forming cores (0.1 pc) have been observed by previous observations. At parsec-scales, molecular clouds have been extensively observed to fragment into clumps of sub-parsecs (e.g., Onishi et al., 1998; Ikeda et al., 2007; André et al., 2010; Schneider et al., 2010; Hill et al., 2011; Liu et al., 2012). Several studies on the earliest stage of massive to intermediate star formation with high angular resolution (PdBI and SMA) have revealed fragmentation inside sub-parsec clumps to 0.1 pc cores (e.g., Peretto et al., 2006; Zhang et al., 2009; Pillai et al., 2011) at millimeter wavelengths. These studies have important implications to massive star and cluster formation.

Limited by angular resolution and large distance to massive star-forming sites, the study of fragmentation inside 0.1 pc cores did not progress much until recently. With the angular resolution of $5''$ provided by CARMA and the relatively small distance to Orion (414 pc) in this study, the CARMA observations reach a spatial resolution of $\sim$ 2000 AU. Our observations revealed that multiple fragments are associated with each massive starless core of 0.1 pc (Sect. 4.3.2), suggesting that hierarchical fragmentation continues to occur at 0.1 pc scales and 0.1 pc cores fragment to even smaller condensations. Recent observations with comparable angular resolutions have reported similar results of fragmentation inside 0.1 pc massive cores at millimeter wavelengths. For example, Bontemps et al. (2010) observed a total of 23 fragments inside 5 massive dense cores in Cygnus X. Wang et al. (2011) revealed 3 condensations of 0.01 pc inside two of the 0.1 pc cores in IRDC

G28.34-P1. Among the 18 massive dense cores ($\sim$ 0.1 pc) that Palau et al. (2013) studied, $\geq$50% showed $\geq$ 4 fragments and 30% showed no signs for fragmentation. Furthermore, using an even higher angular resolution of few hundred AUs and targeting nearby star-forming region Ophiuchus, Nakamura et al. (2012) and Bourke et al. (2012) unveiled the fragmentation inside low-mass 0.1 pc prestellar cores, suggesting a scenario beyond single collapse even for low-mass stars. Some of these condensations are prestellar in nature (Bontemps et al., 2010; Nakamura et al., 2012), and some of them are protostellar evidenced by outflows (Wang et al., 2011; Naranjo-Romero et al., 2012).

4.5.2 Mechanism for Fragmentation: Turbulence + Magnetic Fields

The results from the radiative transfer modeling (Sect. 4.4.1) suggest a highly supersonic linewidth (0.8 km s^{-1}) for Core 2, implying that the environment is highly turbulent and turbulence is playing an important role in fragmentation. Our modeling also showed that signs for fragmentation occur at the colliding point of the convergent flows. This is broadly consistent with the "turbulent fragmentation" scenario (e.g., Klessen et al., 2005; Padoan & Nordlund, 2002), in which density fluctuations are generated at small-scales (0.1 pc) when large-scale shocks dissipate, which lead to star-forming cores.

Our results suggest the number of fragments associated with each massive starless core to be $\sim$ 3 - 5. This level of fragmentation is consistent with the recent studies of fragmentation inside massive dense cores in Cygnus-X (Bontemps et al., 2010) and the two prestellar cores in ρ-Ophiuchus (Nakamura et al., 2012). However, this number of fragments is not quite consistent with the prediction from several turbulent fragmentation models (e.g., Bonnell et al., 2004; Dobbs et al., 2005; Jappsen et al., 2005) since these models predict a much higher number of fragments. For example, Dobbs et al. (2005) performed purely hydrodynamical numerical simulations of a turbulent core of density structure $\rho \propto r^{-1.5}$ with a initial mass of 30 M$_{\odot}$ (comparable to that of our Core 2) and a radius of 0.06 pc. The study found that the core fragments into $\sim$ 20 objects.

The number of fragments can in principle be reduced by radiation feedback (Krumholz et al., 2007) or magnetic fields (Hennebelle et al., 2011). The combination of the two effects work more efficiently in suppressing fragmentation (Commerçon et al., 2011; Myers et al., 2012), with the radiation feedback effectively suppressing the fragmentation in high-density regions (the center of the core) and magnetic fields effectively suppressing the fragmentation in low-density regions (the

outer part of the core). However, since the cores we studied are starless, the radiation feedback is expected to be weak. On the other hand, large-scale magnetic fields are observed in the main region of OMC-1 that is close to our cores (e.g., Houde et al., 2004), supporting the argument that magnetic fields may play a role in the fragmentation process. Measurements of magnetic fields on small-scales at the position of the starless cores are needed to further determine the precise role of magnetic fields.

4.5.3 Role of Supersonic Converging Flows

We obtained a dynamical velocity pattern in the supersonic converging flows (Sect. 4.4.1) associated with Core 2 from the radiative transfer modeling. Other cores including Core 1, 4 and 8 all showed similar spectral features as Core 2 (see Sect 4.4.1) which can be explained by converging flows. Only a few studies have detected the sign for such supersonic convergent flows at 0.1 pc scale (Csengeri et al., 2011a,b). The origin of the supersonic flows is difficult to identify; however, it is natural to speculate the origin being the large-scale flows at few parsecs scale since the prominent large-scale filamentary structures may be due to large-scale turbulent flows (e.g., Mac Low & Klessen, 2004).

Is the converging flow dynamically important in the star formation process? We calculated the flow crossing time as: $t_{cross} = R(0.05pc)/v_{inf}(1.5km/s) = 3.0 \times 10^4$ yr, where v_{inf} is the inflow velocity derived from the radiative transfer modeling. The free-fall time is $t_{ff} = \sqrt{\frac{3\pi}{32G\rho}} = 1.5 \times 10^4$ yr, where we use the derived central density for ρ in the calculation and therefore the derived free-fall time is an upper limit. The flow-crossing time is the timescale that the flows at 0.1 pc scale bring material down to the center, and the free-fall time is the timescale for the material to collapse gravitationally. The flow crossing time is comparable to the free-fall time, suggesting that the flow is dynamically important in forming the density condensations. However, the crossing time is slightly larger than the free-fall time, suggesting that gravity takes over at small-scale in driving the dynamical process of star formation. All together, we suggest that large-scale flows initiate the density condensations, and gravity becomes dominant at small-scales which enhances the converging flows.

We also estimated the mass inflow rate along an filament: $\dot{M}_{inf} = 2 \times \pi R_{fil}^2 \times n_{mean} \times \mu \times m \times v_{inf} = 2.35 \times 10^{-3}$ $M_\odot$ yr^{-1}, where $R_{fil} = 0.025$ pc is the radius of the cylinder (estimated from the model; see Fig. 4.10), n_{mean} is the mean number density of the cylinder, μ is the mean

molecular weight, and m is the mass of hydrogen. The LTE mass of Core 2 is estimated to be 36.6 $M_\odot$ (Sect. 4.3), and therefore the formation timescale for Core 2 is $\sim 1.5 \times 10^4$ yrs. The inflow velocity and mass inflow rate appear to be large compared to low-mass stars which typically have infall velocities ~ 0.1 km s^{-1} (e.g., Lee et al., 2004). However, higher inflow velocities and mass inflow rates are not surprising for massive star-forming regions. For example, several high infrared extinction clouds with massive star formation in Rygl et al. (2013) have the spherical infall velocities in the order of 0.3 - 7 km s^{-1} and mass infall rates on the order of 1.4 - 22.0$\times 10^{-3}$ $M_\odot$ yr^{-1}. Peretto et al. (2006) reported a similar mass inflow rate in a protocluster NGC 2264-C with intermediate- to high- mass star formation. The study found a mass inflow velocity of 1.3 km s^{-1} along a cylinder-like, filamentary structure on a spatial scale of 0.5 pc. We are probably seeing the continuation of the 0.5 pc - scale flow down to the scale of 0.1 pc. However, the underlying physical reason for such highly supersonic velocities is still unclear.

4.5.4 Implications for Massive Star and Cluster Formation

Our result does not fully support either the turbulent core scenario or the competitive accretion scenario. The discovery of fragments in our study makes it harder to form massive stars in these cores via the turbulent core model proposed by McKee & Tan (2003), since the core mass will eventually go to a number of objects rather than a single star. McKee & Tan (2003) suggests a minimum mass accretion rate of 10^{-3} $M_\odot$ yr^{-1} to overcome the radiation pressure and form a massive star. By this criterion, our Core 2 has a high enough inflow rate to form massive stars; however, the inflow may not feed just one single object since the core contains multiple fragments. Krumholz & McKee (2008) suggests that a minimum column density of 1 g cm^{-2} can avoid fragmentation through radiative feedback. We suggest that this is a necessary but not sufficient condition for massive star formation: all cores in this study have column densities larger than that threshold (see Table 4.3), and yet they have already fragmented before the radiative feedback kicks in.

Our result is broadly consistent with a scenario of turbulent fragmentation, with the number of fragments perhaps reduced by magnetic fields. However, while it is possible that the fragmentation continues to occur during the later stages of evolution and/or future massive stars could form via competitive accretion (Bonnell et al., 2004; Bonnell & Bate, 2006), our observations highlighted a

feature that is not present in the standard competitive accretion scenario: rapid converging flows along dense filaments that feed matter into the central region. This feature is similar in spirit to the model proposed by Wang et al. (2010) where the mass accretion rate onto a massive star is set mainly by the large-scale converging or collapsing flow, rather than the gravitational pull of the star itself.

As each fragment has the potential to collapse individually and form protostars, it is suggestive that we are witnessing the formation of clusters at the very early stages and multiplicity occurs already in the prestellar phase. Given a 30% core formation efficiency (Bontemps et al., 2010) for a 30 $M_{\odot}$ core (Sect. 4.3), each individual fragment inside a core will be forming low- to intermediate-mass stars. Therefore, we suggest that these cores are in the dynamical state of forming low- to intermediate- mass protoclusters (e.g., Lee et al., 2011).

Although our study is unique in observing massive starless cores at a distance $\leq$ 500 pc with high spatial resolution, the number of observed fragments may increase with higher resolution and more sensitivity. Follow-up studies of dust continuum with higher resolution are necessary to compliment this study and accurately constrain the properties of these cores, including the masses and the dynamical states of these cores.

4.6 Conclusion

We observed nine starless cores in the Orion-A North region with the IRAM 30-m telescope and eight cores out of the nine cores with the CARMA D-array using CS(2-1). Our main conclusions are as follows:

1. The IRAM 30-m observations showed no detection of N_2D^+(2-1) for all the nine cores, and the CARMA observations showed N_2H^+(1-0) for only two cores (Core 4 and Core 8). As CS(2-1) is regarded as an "early-time tracer" and N-bearing species (N_2D^+(2-1), N_2H^+(1-0)) as "late-time tracers", this result suggests that most of our cores are at the very early stage of star formation.

2. The CS(2-1) observations with the IRAM 30-m telescope showed that majority of the starless cores are single-peaked, and the morphologies traced by CS(2-1), $C^{34}S$(2-1) and CS(3-2) are

mostly consistent with each other. The column densities estimated from CS(2-1) range from $7 - 42 \times 10^{23}$ cm^{-2} and the LTE masses range from 20 M$_\odot$ to 154 M$_\odot$.

3. The comparison between the CARMA CS(2-1) data, the IRAM CS(2-1) data, JCMT 850 μm dust continuum, Herschel 500 μm data shows that gas structures probed by CS(2-1) are forming along small-scale filamentary structures traced by dust continuum, suggesting the importance of filamentary structures to star formation even at small scales.

4. The CARMA CS(2-1) observations show fragmentation inside all the cores except for Core 5. The number of fragments associated with each core ranges from 3 to 5.

5. Five cores showed obvious velocity gradients across the cores in the IRAM CS(2-1) data. We performed a two-dimensional fitting to the velocity gradients by assuming the velocity gradients are linear. The fitting results showed that the velocity gradients range from 1.7 - 14.3 km s^{-1} pc^{-1}.

6. Four cores (Core 1, Core 2, Core 4, Core 8) showed two common features in their spectra along the direction of the velocity gradients. First, the velocity peak changes from blue-shifted to red-shifted across the cores. Second, the intensity of the blue peak is always stronger than the red peak.

7. We propose a model of a cylindrically symmetric filament with converging inflows from the two sides toward the center to explain the two spectral features. We modeled Core 2 with this proposed kinematic model with the radiative transfer code LIME (Brinch & Hogerheijde, 2010), and verified that the kinematic model successfully explains the two features. The best-fit gives a constant supersonic speed of 1.5 km s^{-1} for the flow velocity and a supersonic linewidth of 0.8 km s^{-1}. A mass inflow rate of 2.35×10^{-3} M$_\odot$ yr^{-1} is inferred from the inflow velocity.

8. The supersonic linewidth from the modeling suggests that the core environment is highly turbulent and the fragmentation revealed by the CARMA observations may be due to turbulent fragmentation. However, the number of fragments is much less than the predictions from turbulent fragmentation models (e.g., Dobbs et al., 2005), indicating that magnetic fields may be playing an important role in reducing the level of fragmentation (Hennebelle et al., 2011).

9. The small-scale converging flow is dynamically important to the formation of the cores and their substructures. We suggest that large-scale flows initiate the density condensations, and gravity becomes dominant at small-scales which enhances the converging flows. Due to the high mass inflow rate, each fragment is likely to collapse individually and form seeds for future protoclusters. Given a core formation efficiency of 30%, we suggest that these cores are in the dynamical state of forming low- to intermediate- mass protoclusters.

10. The fragmentation observed in our cores makes massive star formation via the turbulent core model proposed by McKee & Tan (2003) more difficult. Our result does not fully support the standard competitive accretion model either, since it does not account for our inferred rapid inflow along filaments, which may be an important way of feeding massive protostars.

Table 4.1: Coordinates of the detected sources

Source	R.A.(2000)	Dec.(2000)	850 μm dust mass[a]
Core 1	05:35:22.2	-05:25:10	47.4 $M_\odot$
Core 2	05:35:02.2	-05:24:53	1.4 $M_\odot$
Core 3	05:35:25.4	-05:24:33	54.6 $M_\odot$
Core 4	05:35:05.6	-05:22:53	8.5 $M_\odot$
Core 5	05:35:31.9	-05:22:33	5.3 $M_\odot$
Core 6	05:35:25.6	-05:20:15	14.0 $M_\odot$
Core 7	05:35:37.6	-05:18:22	5.8 $M_\odot$
Core 8	05:35:20.0	-05:18:10	12.5 $M_\odot$
Core 9	05:35:38.5	-05:17:18	3.0 $M_\odot$

[a]The 850 μm dust masses were calculated assuming a temperature of 20 K, a mass opacity of 0.01 cm^2 g^{-1}, and a distance of 414 pc to Orion. See Nutter & Ward-Thompson (2007) for more details.

Table 4.2: Molecular Line Observations with the IRAM 30-m Telescope

Line transition	Frequency	Signal-to-Noise Ratio (from the peak intensity)								
	(GHz)	Core 1	Core 2	Core 3	Core 4	Core 5	Core 6	Core 7	Core 8	Core 9
$H^{13}CO^+$(1-0)	86.754330	×	×	×	···	×	···	···	···	···
$C^{34}S$(2-1)	96.412982	8.0	5.3	13.4	···	4.7	···	×	10.6	×
CS(2-1)	97.980968	28.0	13.1	43.3	96.2	37.0	5.6	70.2	137.9	28.7
^{18}CO(1-0)	109.782182	7.7	6.5	10.9	···	···	···	···	18.5	···
CS(3-2)	146.969049	20.0	8.0	36.0	···	12.3	···	7.1	20.8	×
N_2D^+(2-1)	154.217206	×	×	×	···	×	···	···	···	···
^{18}CO(2-1)	219.560319	5.7	3.3	9.8	···	···	···	···	6.8	···
^{12}CO(2-1)	230.537990	13.7	×	11.5	20.8	4.7	52.3	55.6	92.8	50.0

× means no detection (below the 3σ level) with the molecular line. ··· means the molecular line was not observed.

Table 4.3: Properties of CS Cores

Source	Transition	T_A (K)	τ	$\int T_A dv$ (K km s^{-1})	$T_{ex,CS(2-1)}$ (K)	N_{H_2} ($\times 10^{23}$ cm^{-2})	Σ_{H_2} (g cm^{-2})	M_{H_2} ($M_\odot$)	n_{H_2} ($\times 10^6$ cm^{-3})
Core 1	CS(2-1)	6.81	2.24	12.46	12.76	7.28	1.81	26.60	5.44
	$C^{34}S$(2-1)	0.72	0.10						
Core 2	CS(2-1)	3.90	2.69	15.74	8.38	10.02	2.48	36.60	7.47
	$C^{34}S$(2-1)	0.47	0.12						
Core 3	CS(2-1)	5.32	3.66	10.67	10.02	8.85	2.19	32.34	6.61
	$C^{34}S$(2-1)	0.82	0.16						
Core 5	CS(2-1)	2.64	4.78	4.63	6.42	5.32	1.32	19.40	3.97
	$C^{34}S$(2-1)	0.51	0.21						
Core 8	CS(2-1)	12.47	4.69	31.88	19.01	42.14	10.45	154.00	31.46
	$C^{34}S$(2-1)	2.37	0.21						

Table 4.4: CS(2-1) Properties

Parameter	Description	Value
Q_{rot}	rotational partition function	$0.86T_{ex}$
g_I, g_k	degeneration of the quantum number	g_I=1, g_k=1
$S\mu^2$	S: line strength, μ^2: dipole moment	7.71 debye
E_u	energy in the upper state	7.0 K
ν	frequency of the molecular line	97.980968 GHz

Table 4.5: Noise Level for 3 mm continuum observations and Mass Sensitivity

Source	Noise (mJy beam^{-1})	Mass[a] ($M_\odot$)
Core 1	4.7	< 2.85
Core 2	1.3	< 0.79
Core 3	7.7	< 4.67
Core 4	1.9	< 1.15
Core 5	2.2	< 1.33
Core 6	2.4	< 1.42
Core 7	15.0	< 9.09
Core 8	1.9	< 1.15

[a]The mass corresponds to the 3σ upper limit for detection.

Table 4.6: 2D fitting of velocity gradients

Source	v_0 (km s^{-1})	a (km s^{-1} pc^{-1})	b (km s^{-1} pc^{-1})	g (km s^{-1} pc^{-1})	θ_g (degree)
Core 1	10.49±0.20	3.43±0.35	1.17±0.43	4.28±0.42	71.9±5.7
Core 2	9.91±0.16	-9.96±0.51	-6.91±0.76	14.31±0.71	55.2±2.8
Core 3	10.25±0.20	0.87±0.45	-1.11±0.41	1.66±0.51	321.7±17.3
Core 4	7.98±0.19	-8.87±0.52	-1.76±0.92	10.67±0.64	78.79±3.4
Core 5	7.28±0.19	-4.31±0.84	-8.07±1.40	10.81±1.52	28.10±8.1
Core 6	7.07±0.12	-0.43±0.45	-1.36±0.58	1.69±0.61	17.42±22.9
Core 7	9.77±0.20	2.67±0.46	6.73±0.48	8.54±0.55	21.63±3.8
Core 8	9.45±0.10	-6.01±0.34	0.18±0.31	7.09±0.40	271.8±3.2
Core 9	9.29±0.28	3.68±0.80	3.77±0.58	6.22±0.83	44.3±7.6

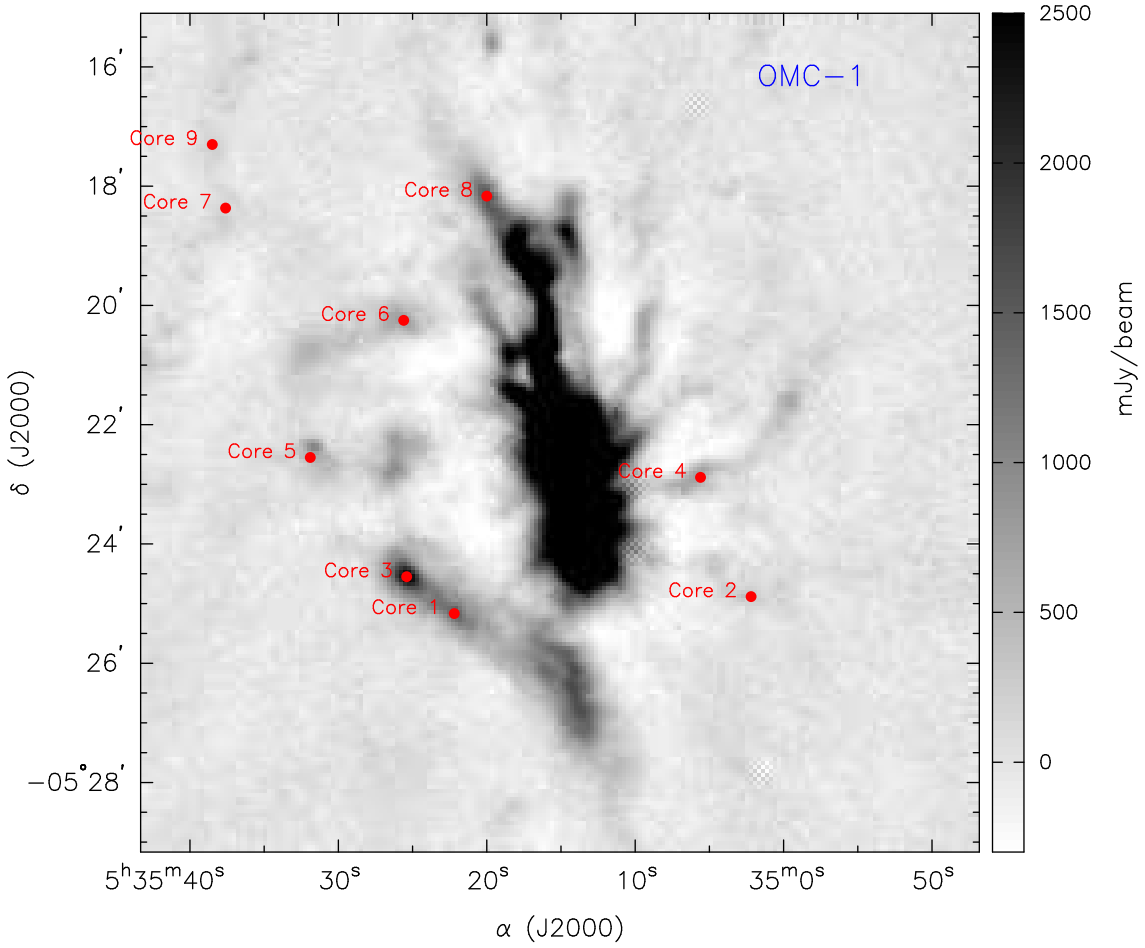

Figure 4.1: The 850 μm dust continuum image of Orion A-North from the JCMT SCUBA archive. The positions of the nine cores observed with the IRAM 30-meter telescope are plotted with red circles.

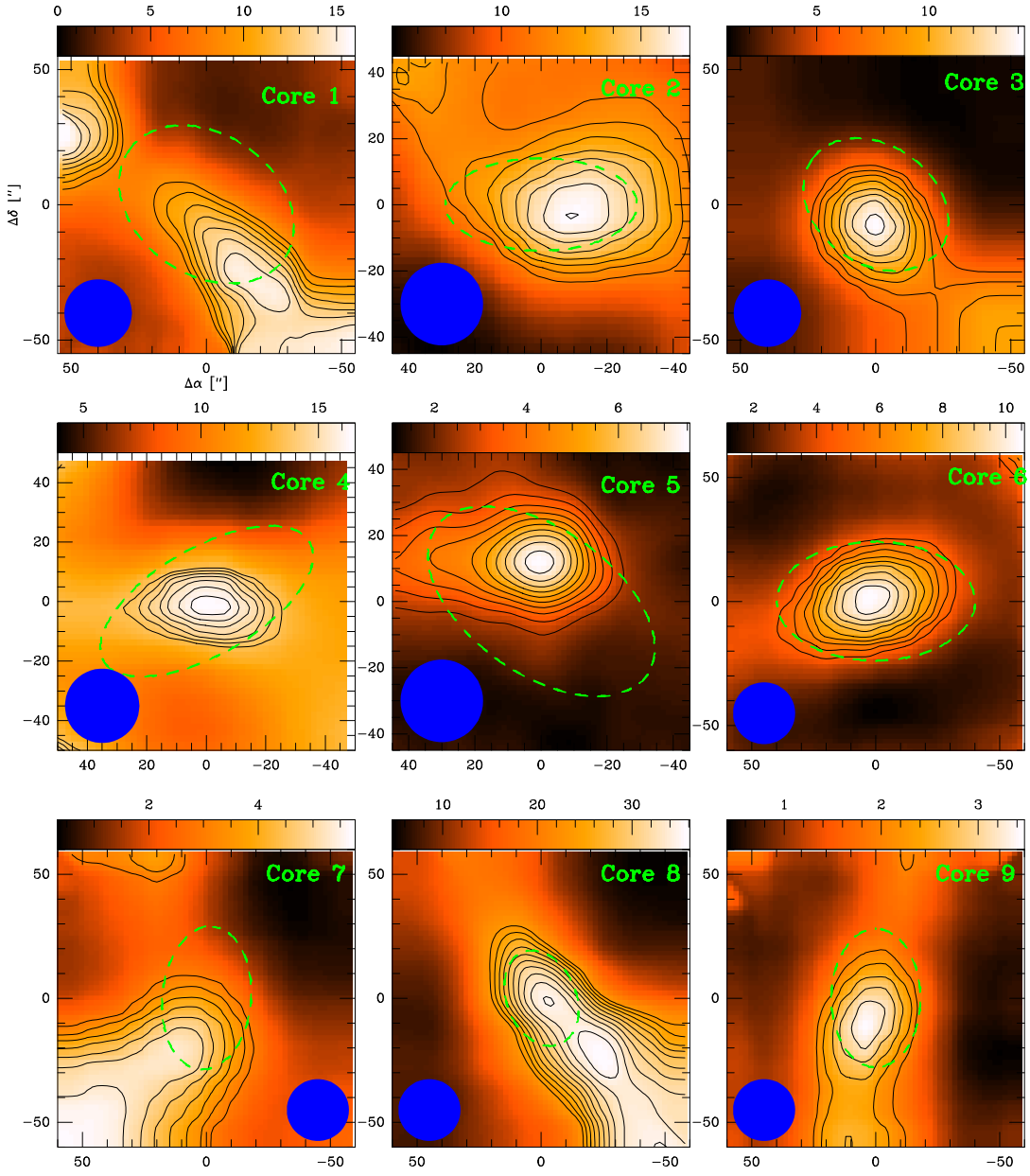

Figure 4.2: The 0^{th} moment maps from the IRAM CS(2-1) observations toward the nine starless cores. The blue circle in each panel indicates the beam size (25″) of the IRAM 30-m telescope. The green dashed ellipses are the definitions of 850 μm dust cores from Nutter & Ward-Thompson (2007). Most of the cores show single peaks and are associated with elongated structures. The 0^{th} moment maps are generated from these velocity ranges: Core 1: (11.91, 9.16) km s^{-1}; Core 2: (13.23, 6.77) km s^{-1}; Core 3: (11.73, 8.57) km s^{-1}; Core 4: (12.03, 5.58) km s^{-1}; Core 5: (8.57, 4.38) km s^{-1}; Core 6: (8.39, 5.04) km s^{-1}; Core 7: (15.74, 3.79) km s^{-1}; Core 8: (11.91, 7.49) km s^{-1}; Core 9: (12.15, 7.37) km s^{-1}. The contour levels (σ, starting level, interval) are as following. Core 1: σ=0.6 K km s^{-1}, 15σ, 1.5σ. Core 2: σ=0.38 K km s^{-1}, 30σ, 2σ. Core 3: σ=0.26 K km s^{-1}, 25σ, 4σ. Core 4: σ=0.62 K km s^{-1}, 62σ, 2σ. Core 5: σ=0.26 K km s^{-1}, 10σ, 2σ. Core 6: σ=0.23 K km s^{-1}, 20σ, 3σ. Core 7: σ=0.2 K km s^{-1}, 15σ, 2σ. Core 8: σ=0.26 K km s^{-1}, 90σ, 5σ. Core 9: σ=0.2 K km s^{-1}, 10σ, 1.5σ.

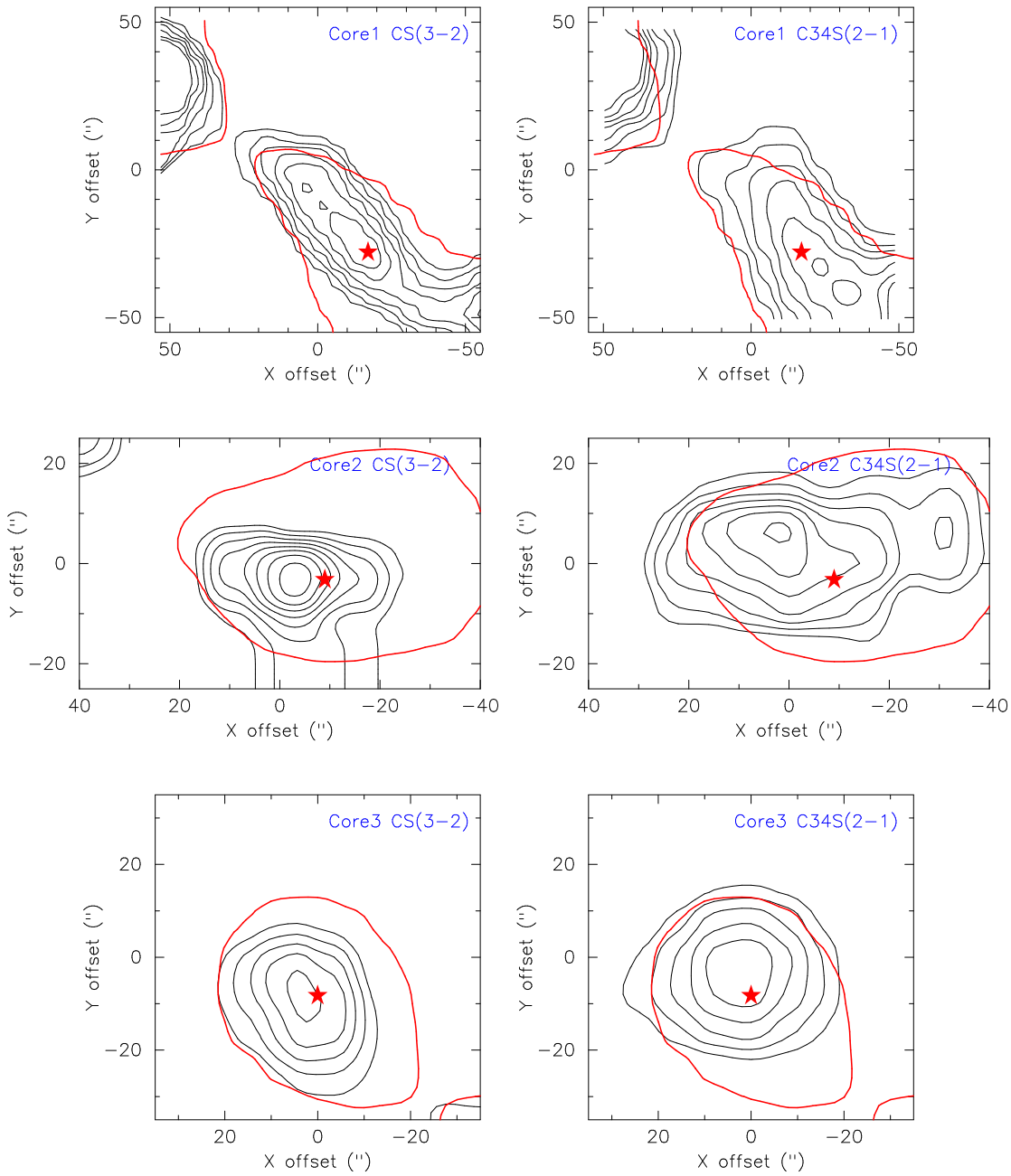

Figure 4.3: 0^{th} moment maps from the IRAM CS(3-2) and $C^{34}S$(2-1) observations for the five starless cores. The black contours in the left panels show CS(3-2) and the black contours in the right panels show $C^{34}S$(2-1). The red contours are the IRAM CS(2-1) emission (lowest contours in Fig. 4.2) and the red stars are where the CS(2-1) emission peak. The contour levels (σ, starting level, interval) for CS(3-2) are: Core 1: $\sigma = 0.38$ K km s^{-1}, 25σ, 5σ; Core 2: $\sigma = 0.56$ K km s^{-1}, 19σ, 1σ; Core 3: $\sigma = 0.33$ K km s^{-1}, 35σ, 10σ; Core 5: $\sigma = 0.23$ K km s^{-1}, 15σ, 5σ; Core 8: $\sigma = 0.52$ K km s^{-1}, 35σ, 10σ. The contour levels (σ, starting level, interval) for $C^{34}S$(2-1) are: Core 1: $\sigma = 0.07$ K km s^{-1}, 8σ, 2σ; Core 2: $\sigma = 0.29$ K km s^{-1}, 5σ, 0.5σ; Core 3: $\sigma = 0.1$ K km s^{-1}, 10σ, 2σ; Core 5: $\sigma = 0.06$ K km s^{-1}, 5σ, 2σ; Core 8: $\sigma = 0.16$ K km s^{-1}, 15σ, 5σ.

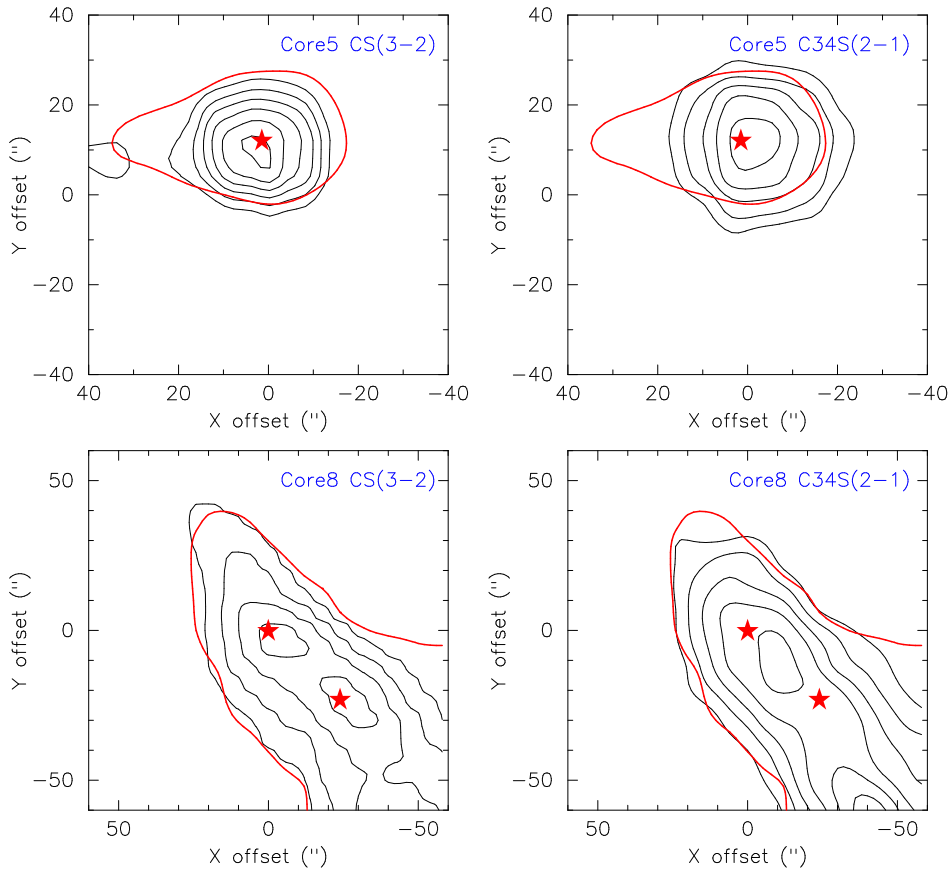

Figure 4.3: continued.

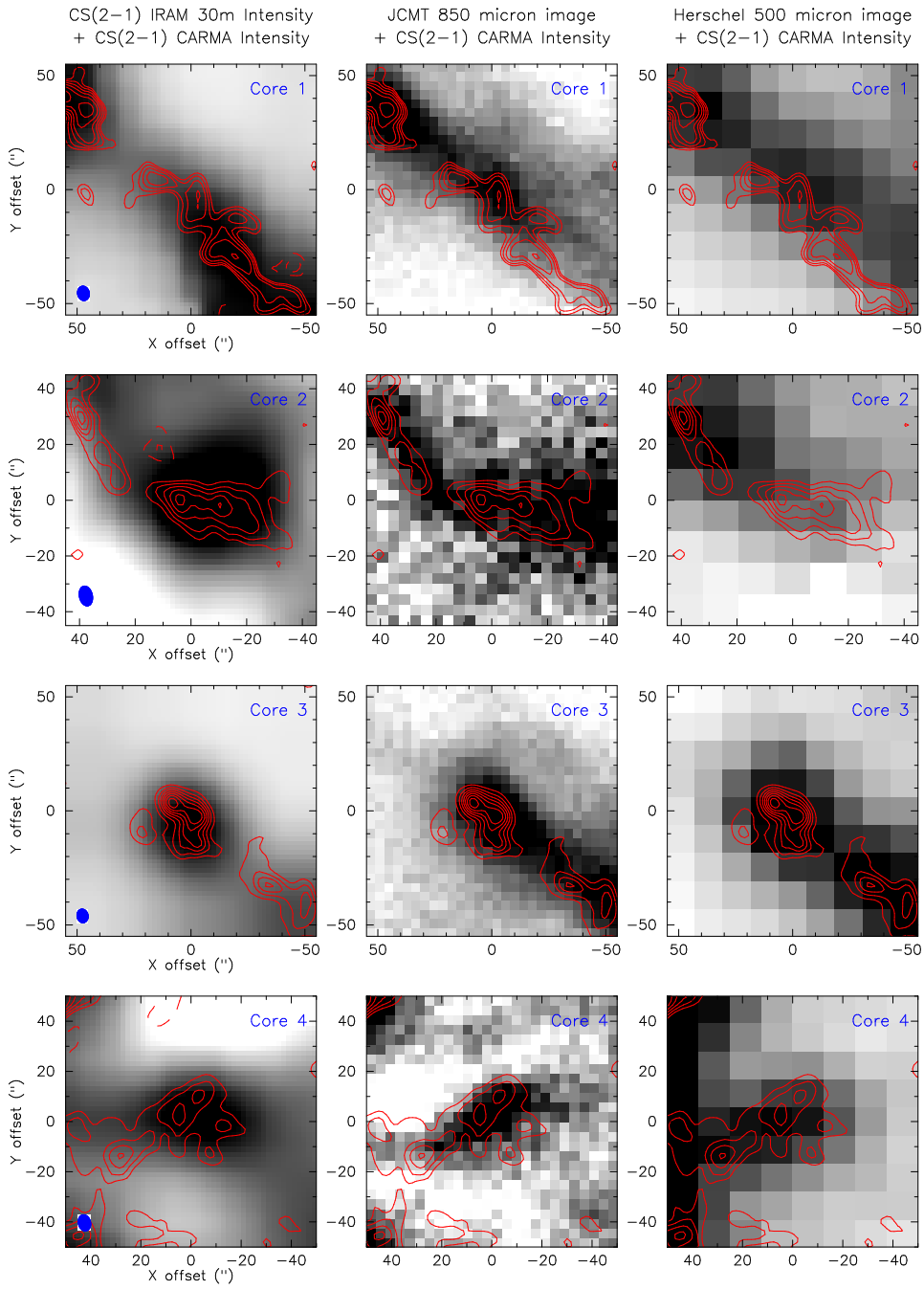

Figure 4.4: The 0^{th} moment maps from the CARMA CS(2-1) observations (red contours) overlaid on the IRAM CS(2-1) observations (first column), JCMT 850 μm dust continuum (second column), and the *Herschel* 500 μm dust continuum (third column). The contour levels (σ, starting level, interval) are: Core 1: $\sigma = 0.32$ Jy beam^{-1} km s^{-1}, $\pm5\sigma$, $\times\sqrt{2}\sigma$; Core 2: $\sigma = 0.32$ Jy beam^{-1} km s^{-1}, $\pm5\sigma$, $\pm2\sigma$; Core 3: $\sigma = 0.45$ Jy beam^{-1} km s^{-1}, $\pm5\sigma$, $\pm5\sigma$; Core 4: $\sigma = 0.4$ Jy beam^{-1} km s^{-1}, $\pm5\sigma$, $\pm3\sigma$; Core 5: $\sigma = 0.18$ Jy beam^{-1} km s^{-1}, $\pm5\sigma$, $\pm5\sigma$; Core 6: $\sigma = 0.16$ Jy beam^{-1} km s^{-1}, $\pm10\sigma$, $\pm10\sigma$; Core 7: $\sigma = 0.2$ Jy beam^{-1} km s^{-1}, $\pm5\sigma$, $\pm2\sigma$; Core 8: $\sigma = 0.6$ Jy beam^{-1} km s^{-1}, $\pm10\sigma$, $\pm3\sigma$.

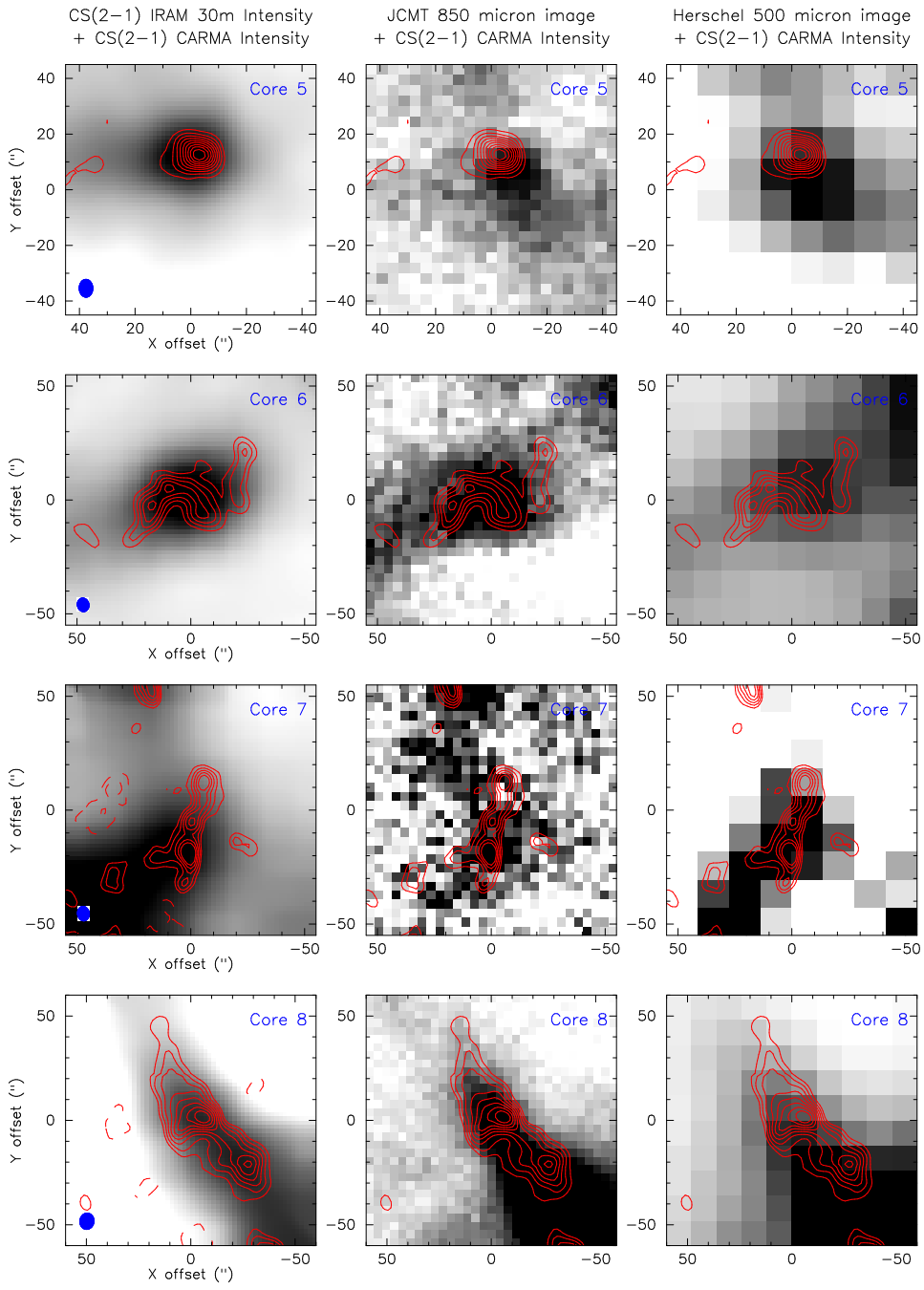

Figure 4.4: Continued.

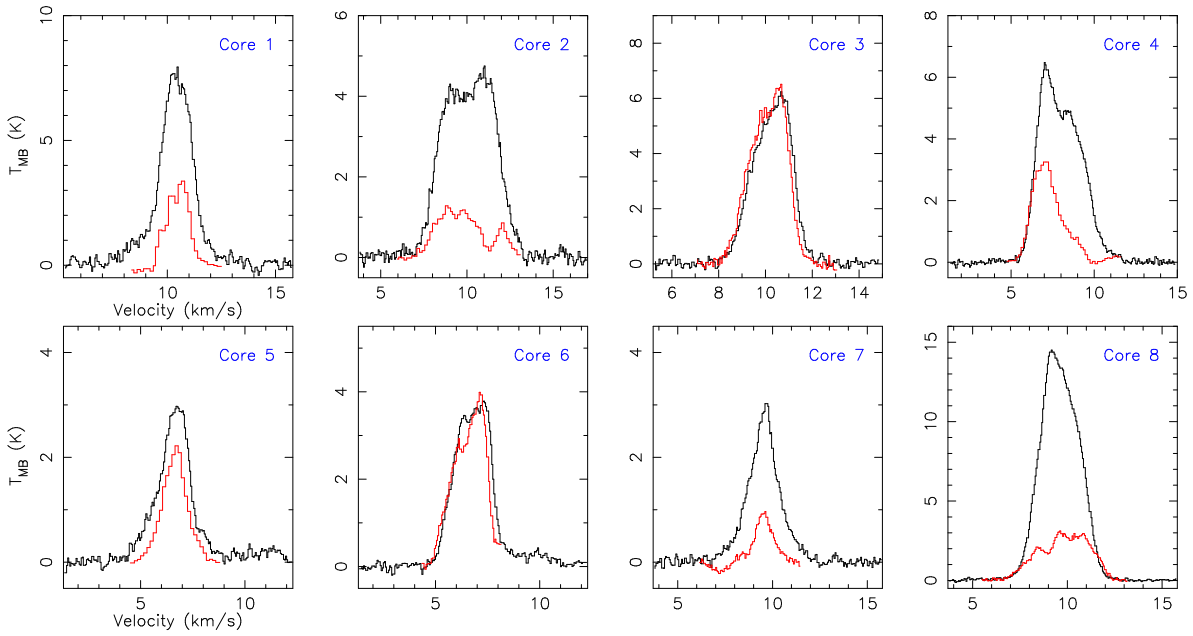

Figure 4.5: Comparison between the IRAM CS(2-1) flux density (black lines) and the CARMA CS(2-1) flux (red lines). The rms noises for the IRAM data are: 0.24 K (Core 1), 0.15 K (Core 2), 0.1 K (Core 3), 0.085 K (Core 4), 0.1 K (Core 5), 0.09 K (Core 6), 0.075 K (Core 7), and 0.075 K (Core 8). The rms noises for the convolved CARMA data are: 0.096 K (Core 1), 0.17 K (Core 2), 0.17 (Core 3), 0.094 K (Core 4), 0.087 K (Core 5), 0.093 (Core 6), 0.116 K (Core 7), 0.122 K (Core 8).

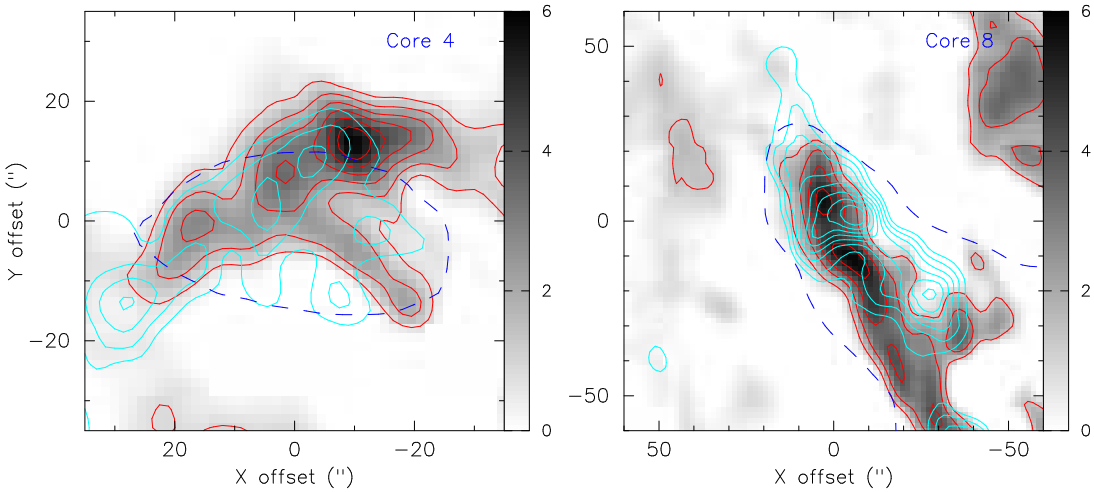

Figure 4.6: The 0^{th} moment maps from the CARMA N_2H^+(1-0) observation (red contours and grey scale) in comparison with the 0^{th} moment maps from the CARMA CS(2-1) observations (cyan contours). The blue dashed lines are the JCMT 850 μm definition. The contour levels for the N_2H^+(1-0) emission are 10%, 20%, 30%, 40%, 50%, 60%, 70%, 80%, 90%, and 100% of the peak intensities (in Jy beam^{-1} km s^{-1}).

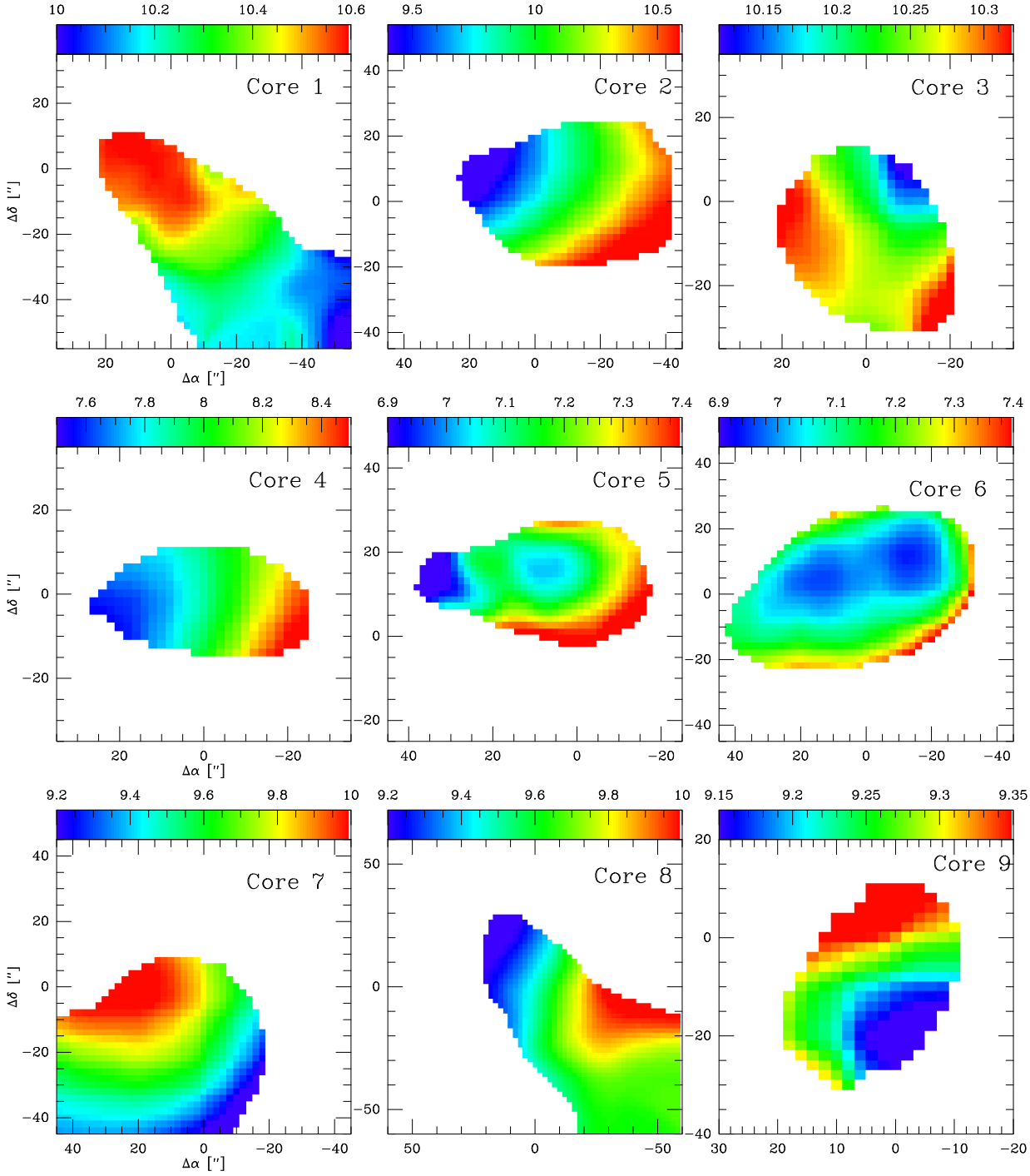

Figure 4.7: First moment maps from the IRAM CS(2-1) data. The color scale indicates velocity in km s^{-1}.

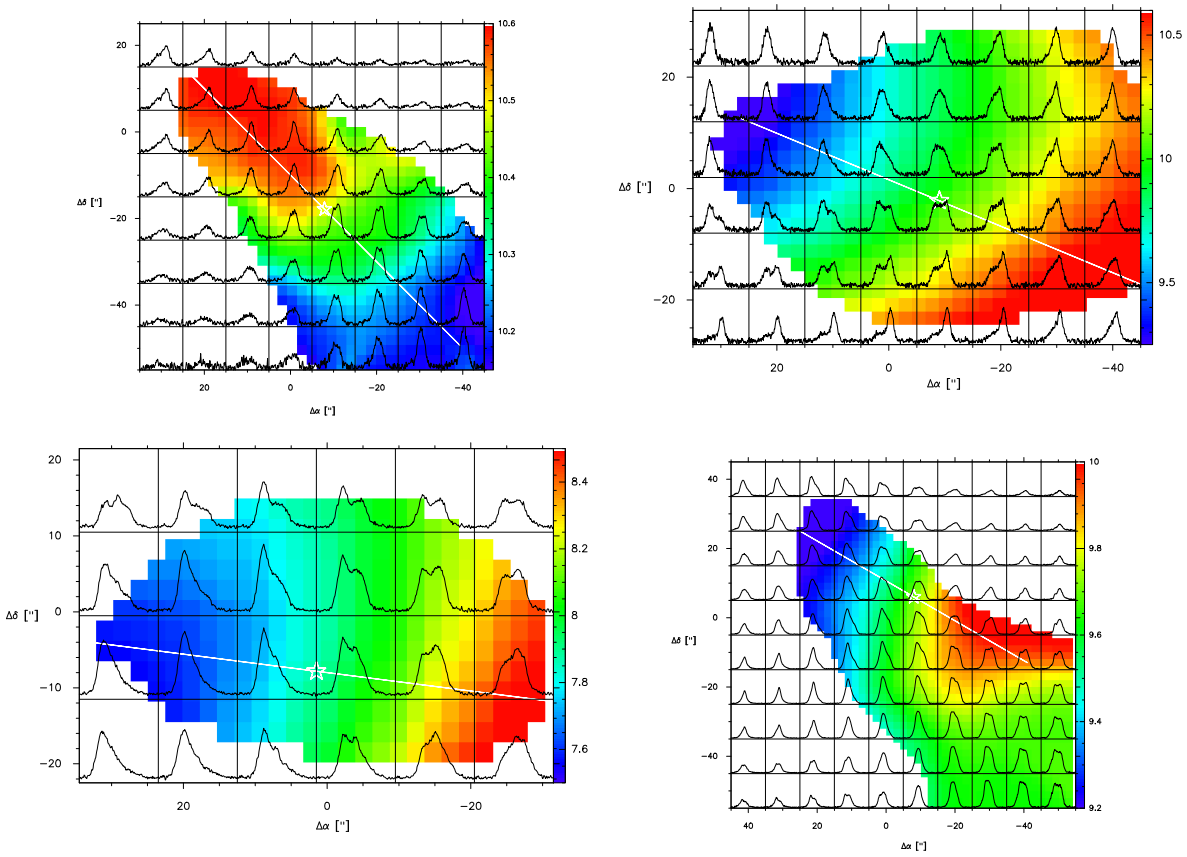

Figure 4.8: Spectral maps overlaid on the first moment maps (from Fig. 4.7) from the IRAM CS(2-1) observations. Upper left: Core 1. Upper right: Core 2. Bottom left: Core 4. Bottom right: Core 8.

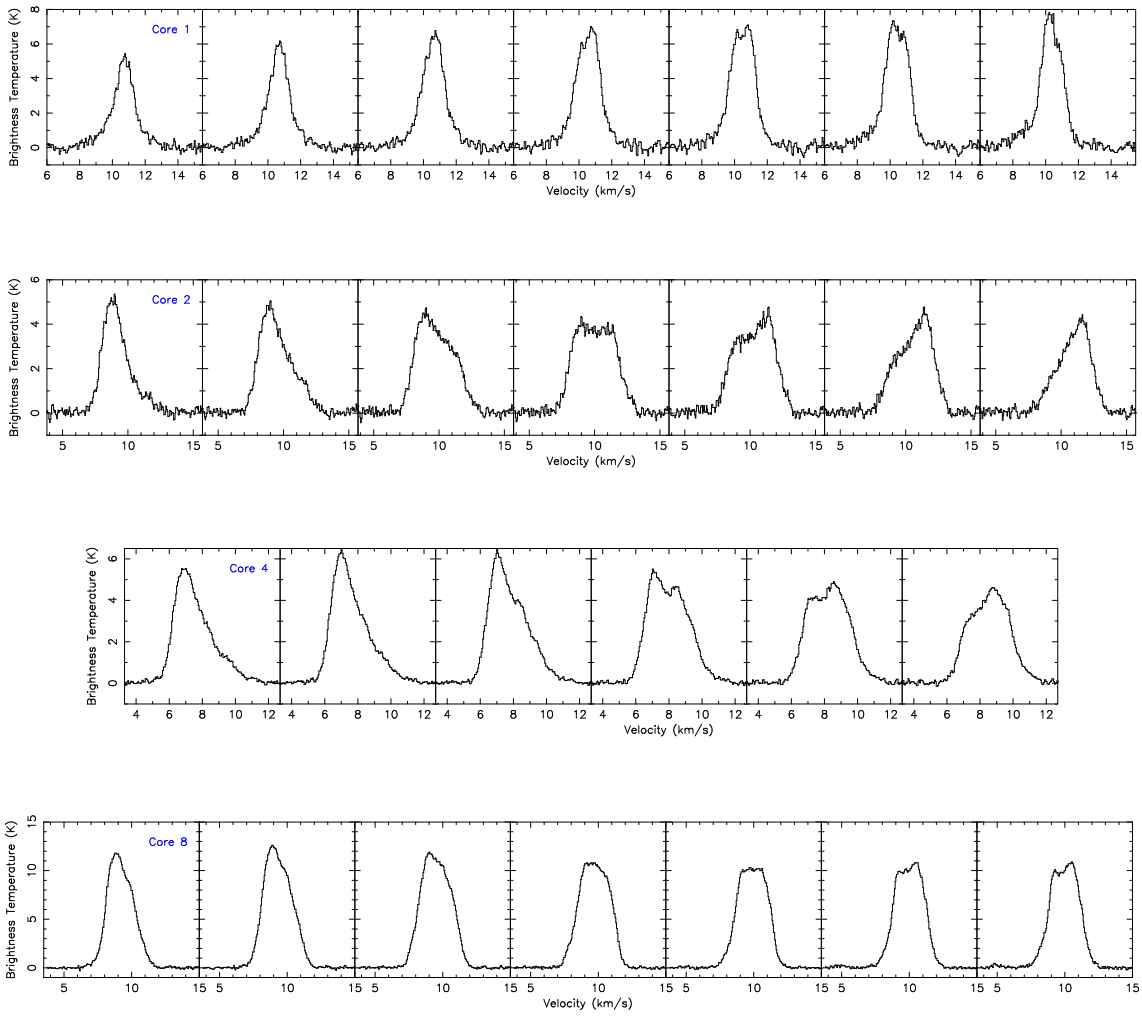

Figure 4.9: Spectra of the four cores along the white lines in Figure 4.8.

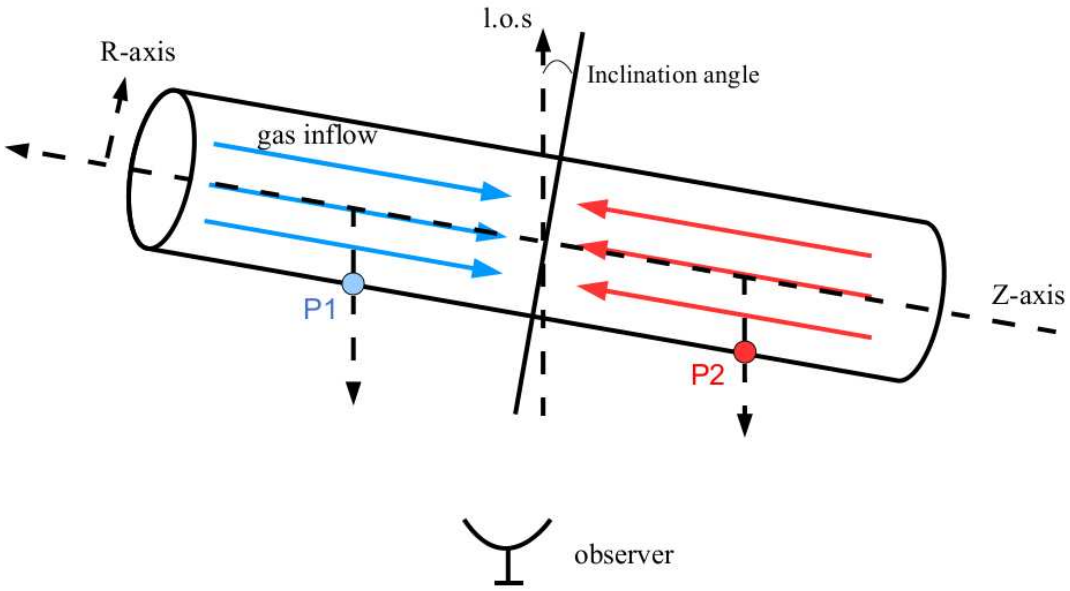

Figure 4.10: The model for the radiative transfer modeling.

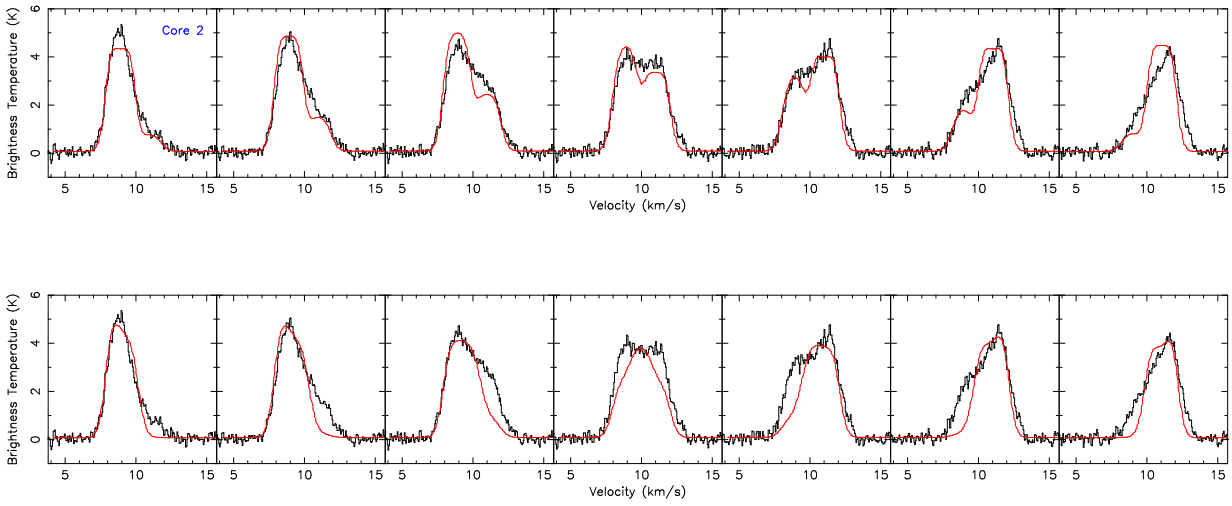

Figure 4.11: The inflow model (top) and the rotation model (bottom). The black lines are from the data of Core 2 and the red lines indicate the radiative transfer model.

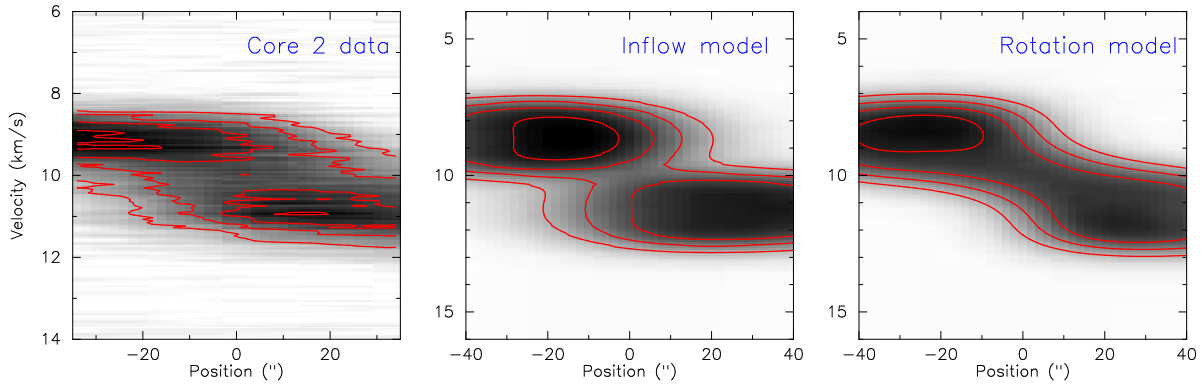

Figure 4.12: The PV diagrams of the data (left panel), inflow model (central panel), and rotation model (right panel). The PV diagrams are from the cut shown in Fig. 4.9. The contours are 30%, 50%, 70%, and 90% of the peak values in all three panels.

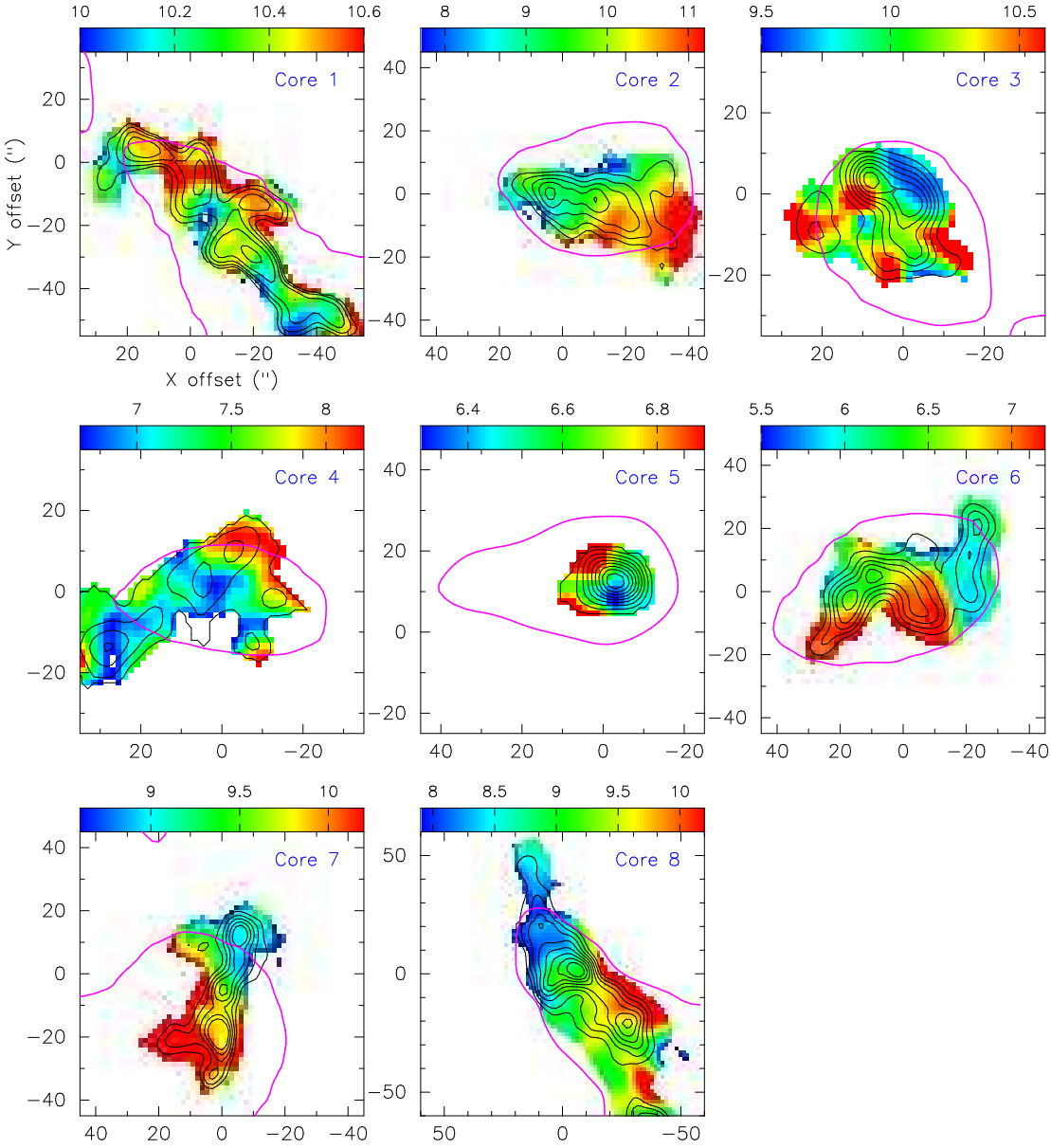

Figure 4.13: First moment maps from the CARMA CS(2-1) data. The magneta lines are the IRAM CS(2-1) cores. The color indicates velocity in km s^{-1}.

Chapter 5

CARMA Large Area Star Formation Survey: First Look at Serpens Main, NGC1333 SVS-13, and Barnard 1

The work presented in this chapter is done by a large collaboration from several institutes and has been presented in the 221st AAS meeting, 2013 by Looney et al. (2013), Mundy et al. (2013), and Storm et al. (2013). All the figures are used with the permission of the authors.

5.1 Introduction

The star formation process spans a wide range of spatial scales from molecular clouds at parsecs to young stellar objects at few thousand AUs. Low-density gas ($\sim$ 10^2 cm^{-2}) in the ISM forms denser structures in molecular clouds ($\sim$ 10^3 cm^{-3}) which evolve to higher density structures at small scales to the formation of stars and clusters. This general picture presents a broad consensus in the study of star formation; however, a comprehensive understanding toward star formation involving turbulence, magnetic fields, and gravity at all spatial scales is not yet achieved. While several theoretical scenarios have been proposed to address this question (Mouschovias & Spitzer, 1976; Basu & Mouschovias, 1995; Mac Low & Klessen, 2004; McKee & Ostriker, 2007), observational tests have been insufficient to directly probe the conditions for star formation from 1000 AU to parsecs. Previous surveys of the nearby star forming regions have been carried out with the *Herschel* Goult Belt Survey (e.g., André et al., 2010), *Spitzer* Legacy c2d project (e.g., Evans et al., 2003; Harvey et al., 2006), and the *JCMT* Legacy Survey (e.g., Buckle et al., 2010). These surveys have provided important views into star formation; nevertheless, we have lack the perspective from observations at millimeter wavelengths covering 1000 AU to parsecs scales with required sensitivity and resolution.

The CARMA Large Area Star-forming Survey (CLASSy), a large survey toward star-forming regions in the nearby Goult Belt, addresses this gap. By combining the cross-correlation and auto-correlation data with the full CARMA 23 antennas, the CLASSy project aims to reconstruct the

emission over a broad range of spatial scales (from few parsecs to few thousand AUs) to study star formation. The goals of this on-going project are (1) to characterize the internal structure and dynamics of star-forming cores, (2) to investigate the relation between dense cores and their natal molecular clouds, and (3) to test existing star formation theories. The target regions are NGC1333 SVS-13, Barnard 1 (B1) and L1451 in Perseus, the Serpens Main, and Serpens South clouds, presenting a wide level of star formation activities from relatively quiescent regions to massive star-forming clusters. The observations for L1451 and Serpens South are currently being performed. In this chapter, I will present the first results of the project from Serpens Main, NGC 1333 SVS-13, and B1.

5.2 Observations

The CLASSy project observes three molecular lines, N_2H^+(1-0) at 93.173505 GHz, HCO^+(1-0) at 89.188518 GHz, and HCN(1-0) at 88.63185 GHz, with the CARMA D and E array. All the observations are performed with 23 elements including six 10-m dishes, nine 8-m dishes, and eight 3.5-m dishes. The single-dish mode and interferometric mode are both used in every region, and the final maps we present in this chapter are the combined data from these two modes.

The observations of Serpens Main were carried out in March, April, July, and August, 2012. The observations of Serpens Main span a total area of $12'$ by $17'$ with 531 mosaic pointings and a total observing time of 100 hours. The synthesized beam is $7.0''$ by $7.7''$; the spectral resolution is 0.16 km s^{-1} with the 8 MHz bandwidth. The sensitivity per channel for line observations is $\sim$ 200 mJy beam^{-1}, and the sensitivity for continuum observations is 1.6 mJy beam^{-1}.

For NGC 1333 SVS-13, the data were taken in January, February, and March, 2011. The total observing area is $8'$ by $13'$ with 527 pointings for mosaic. The synthesized beam is $8.1''$ by $6.3''$; the spectral resolution is 0.62 km s^{-1} with the 32 MHz bandwidth. The sensitivity per channel for line observations is $\sim$ 85 mJy beam^{-1}, and the sensitivity for continuum observations is 1.5 mJy beam^{-1}.

The observations of B1 were performed in April, May, July, September, and October, 2012. The observing area covers $8'$ by $18'$ with 743 pointings for mosaic and a total observing time of 150 hours. The synthesized beam is $6.5''$ by $7.5''$; the spectral resolution is 0.16 km s^{-1} with the 8

MHz bandwidth. The sensitivity per channel for line observations is $\sim$ 100 mJy beam^{-1}, and the sensitivity for continuum observations is 1.5 mJy beam^{-1}.

5.3 Results and Discussions

5.3.1 Serpens Main

The Serpens Main region is an active star-forming site for low-mass stars. Located at a distance of 415 pc (Loinard et al., 2011) (previously measured to be $\sim$ 260 pc; see Eiroa et al. (2008) and references therein), Serpens Main consists of two main sub-clusters in NW and SE. The *Spitzer c2d* survey has detected numerous YSOs at different Class 0/I/II stages (Harvey et al., 2006, 2007). Davis et al. (1999) mapped 11 continuum sources with SCUBA bolometer observations at 850 μm (SMM1 to SMM11); four of the continuum sources are in the NW sub-cluster and six are in the SE sub-cluster. SMM2, 3, and 4 have been observed associated with infall motions (Gregersen et al., 1997), indicating that these submillimeter cores are undergoing star formation activities. Various outflows have also been detected in these two sub-clusters (Davis et al., 1999; Graves et al., 2010). The core mass functions in Serpens Main measured at millimeter wavelengths (at 3mm and 1.1mm) have been derived and compared with the stellar initial mass function (Testi & Sargent, 1998; Enoch et al., 2007).

The left panel in Figure 5.1 shows the integrated intensity map from the CARMA N_2H^+(1-0) observations. The CARMA image shows two main features. First, prominent filamentary structures are observed in the region, especially in the SE sub-cluster. In particular, two thin filaments in the south are resolved for the first time. The filaments associated with the SE cub-cluster "radiate-out" from the central cluster, as one clear example of "hub-filament" systems proposed by Myers (2009). Second, dense gas ($\geq 10^5$ cm^{-3}) traced by N_2H^+(1-0) show peaks that are well coincided with the SCUBA SMM cores (white triangles in the right panel, Fig. 5.1). The right panel in Figure 5.1 shows the N_2H^+(1-0) emission overlaid on the *Herschel* 350 μm image. These two emissions are in good agreement with each other. Figure 5.2 shows the integrated intensity maps from HCO^+(1-0) and HCN(1-0). These two molecular lines are extensively used in tracing outflow activities, and the maps from the two lines resemble with each other. Filamentary structures from these two lines are not as bright as traced by N_2H^+.

Figure 5.3 shows the velocity centroids and velocity dispersions fitted with the strongest N_2H^+ line. As seen in the left panel, the velocity fields in the two sub-clusters are distinct. The NW cluster presents relatively uniform velocity fields, while the SE cluster is associated with more complicated velocity fields. There appears to be a global velocity gradient from the NW cluster to the SE cluster; however, the southern filaments disrupt this global gradient feature and display a discontinuity in velocity from the center of the SE cluster. While the mechanism to the formation of the filaments and the velocity fields is not yet clear, Duarte-Cabral et al. (2011) suggests a scenario of cloud-cloud collision that triggers the star formation activities and produces the observed velocity fields in the SE cluster. The velocity dispersion map (right panel in Figure 5.3) shows that most of the filamentary structures are quiescent. Positions associated with SMM cores appear to have larger linewidths possibly due to local turbulence generated by outflows.

5.3.2 NGC 1333 SVS-13

Located in Perseus at $\sim$ 250 pc (see Enoch et al., 2006, and references therein), NGC 1333 is one of the two main clusters (the other one is IC 348) in Perseus which is often cited as a low-to-intermediate star-forming region between massive star-forming Orion and low-mass, quiescent Taurus (Ladd et al., 1993, 1994). NGC 1333 is a very young cluster with an age less than 1 Myr (Lada et al., 1996; Wilking et al., 2004). Nearly 100 YSOs have been identified from the *Spitzer c2d* survey (Jørgensen et al., 2006) and $\sim$ 30 submillimeter cores are revealed by *JCMT* SCUBA observations (Hatchell et al., 2005). Outflows have been identified with associated submillimeter cores and the estimated energy from outflows is greater than the estimated turbulent energy (Curtis et al., 2010). Our mapping area includes IRAS 4, IRAS 2, and SVS-13 (right panel, Fig. 5.4), and contains $\sim$ 75 YSOs as well as $\sim$ 20 submillimeter cores.

The left panel in Figure 5.4 and Figure 5.5 show the integrated intensity maps from the CARMA N_2H^+(1-0), HCO^+(1-0), and HCN(1-0) observations. The emissions from these three molecular lines show complementary views in tracing filamentary and clumpy structures. N_2H^+(1-0) favors dense gas and the peaks are matched well with the bright sources at *Herschel* 100 μm observations, while HCO^+ and HCN trace more extended, lower density gas. Figure 5.6 presents the fitted velocity centroid map from N_2H^+(1-0). The most noticeable feature is the velocity gradient ($\sim$ 0.8 km s^{-1}) at the bottom third of the map in the SE direction (the blue-green-yellow transition).

This sharp ridge of velocity shift is revealed for the first time. This ridge contains several bright YSOs including IRAS 4. Core formation regulated by supersonic turbulent flows provides a possible explanation for the correlation between the velocity field and dense cores (Gong & Ostriker, 2011).

5.3.3 B1

B1 is located 3.5 pc east of NGC 1333. Compared to NGC 1333, B1 is a smaller group with ~ 10 YSOs (Jørgensen et al., 2006) and 11 submillimeter cores (Hatchell et al., 2005). The distribution of these cores follows a gradient from Class 0/I sources at the main core in the north, to mostly starless cores in the filament SW to the main core, and to the more diffuse gas in the south. The main core is associated with outflow and shock activities (Hiramatsu et al., 2010; Walawender et al., 2005). The main core is observed with a relatively strong magnetic fields of 27 μG (Goodman et al., 1989) and organized grain alignment (Matthews & Wilson, 2002), which are suggested to have influences on the star formation in the region.

The upper panel in Figure 5.7 shows the integrated intensity maps from the CARMA N_2H^+(1-0) observations. Dense, cool gas is present in the whole region, and the main core has the strongest emission. There are about five YSOs and six submillimeter cores in the B1 main core; however, the correlation between the locations of YSOs and dense gas peaks is weak, except for the Class 0 source B1-c. The bottom panel in Figure 5.7 shows the N_2H^+ emission overlaid on the *Herschel* 350 μm image from Storm et al. (2013). The cool dust and dense gas coincide well in the main core. Figure 5.8 shows the integrated intensity maps from the HCO^+(1-0) and HCN(1-0) observations. HCO^+(1-0) and HCN(1-0) appear to trace more diffuse gas and outflows, a similar result as seen in NGC 1333 and Serpens Main.

Figure 5.9 shows the fitted velocity centroid map from N_2H^+ (Storm et al., 2013). The main B1-core can be approximately divided into two clumps in the north (containing B1-c) and south (containing B1-a, B1-b, and B1-d) according to the kinematics. Both the north and south clumps have velocity gradient of ~ 6 km s^{-1} pc^{-1} with the directions of gradients nearly perpendicular to each other. The filament in the southwest of the main core appears to be coherent in velocity, and a shift in velocity occurs toward the southest region.

5.4 Summary and Future Work

This chapter presents the first results of Serpens Main, NGC 1333, and Barnard 1 from the CARMA Large Area Star-forming Survey (CLASSy). Observations of three molecular lines (N_2H^+(1-0), HCO^+(1-0), HCN(1-0)) have been carried out using the full 23 elements in D and E array with the combination of the single-dish and interferometric mode. These first results show the global properties in these regions, including the distribution of dense gas revealed by N_2H^+(1-0), outflow activities traced by HCO^+(1-0) and HCN(1-0), and the kinematic structures from velocity centroid maps. Comparison with the *Spitzer c2d* survey, *JCMT* SCUBA survey, and *Herschel* results have been discussed. As the CLASSy project is unique in probing star formation on scales from 1 pc to 1500 AU, these data will provide the unprecedented opportunity to study star formation in many ways, including the role of magnetic fields and turbulence in star formation, the relation between dense cores and ambient clouds, and the formation mechanisms for these star-forming regions. In particular, in the future I plan to study the gas kinematics in these regions at all spatial scales. Studying large-scale kinemaitcs will allow us to test the role of turbulence since non-isotropic turbulence/velocity fields are expected in filamentary structures with dynamical patterns due to supersonic converging flows (Mac Low & Klessen, 2004). Studying small-scale kinematics will provide insight into core formation by identifying signatures of the external convergent motion and core-forming flows (Hacar & Tafalla, 2011; Tobin et al., 2012a).

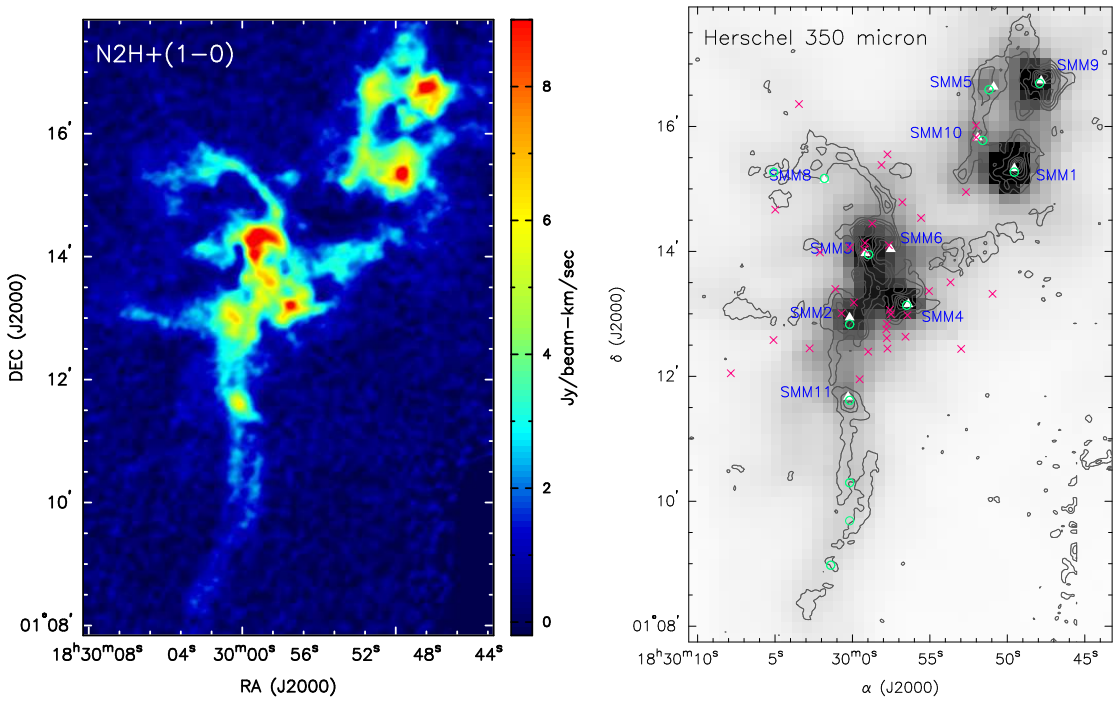

Figure 5.1: *Left panel*: The integrated intensity map of N_2H^+(1-0) in Serpens Main. The image is mapped using the strongest hyperfine line with a velocity range 10.83 km s^{-1} to 5.52 km s^{-1}. *Right panel*: N_2H^+(1-0) integrated intensity map overlaid on the *Herschel* 350 μm image. The contour levels are 3, 8, 13, 18, 23, 28, 33, 38 times the σ level (σ = 0.224 Jy $beam^{-1}$ km s^{-1}). White triangles: SCUBA 850 μm cores (Davis et al., 1999). Green circles: SCUBA 850 m cores (Di Francesco et al., 2008). Red crosses: Spitzer c2d YSOs candidates (Evans et al., 2009).

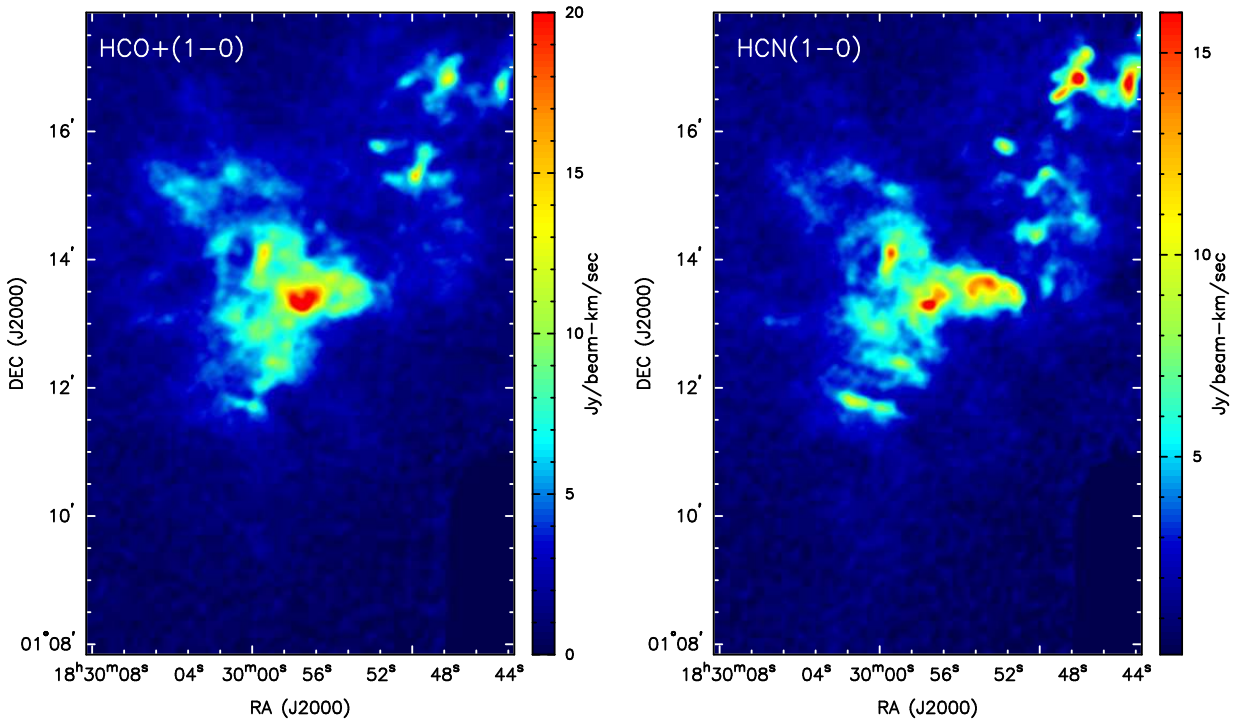

Figure 5.2: The integrated intensity maps of HCO^+(1-0) (left panel) and HCN(1-0) (right panel) in Serpens Main. The maps are generated in a velocity range of 12.87 km s^{-1} to 2.51 km s^{-1} for HCO^+(1-0) and 13.19 km s^{-1} to 2.98 km s^{-1} for HCN(1-0).

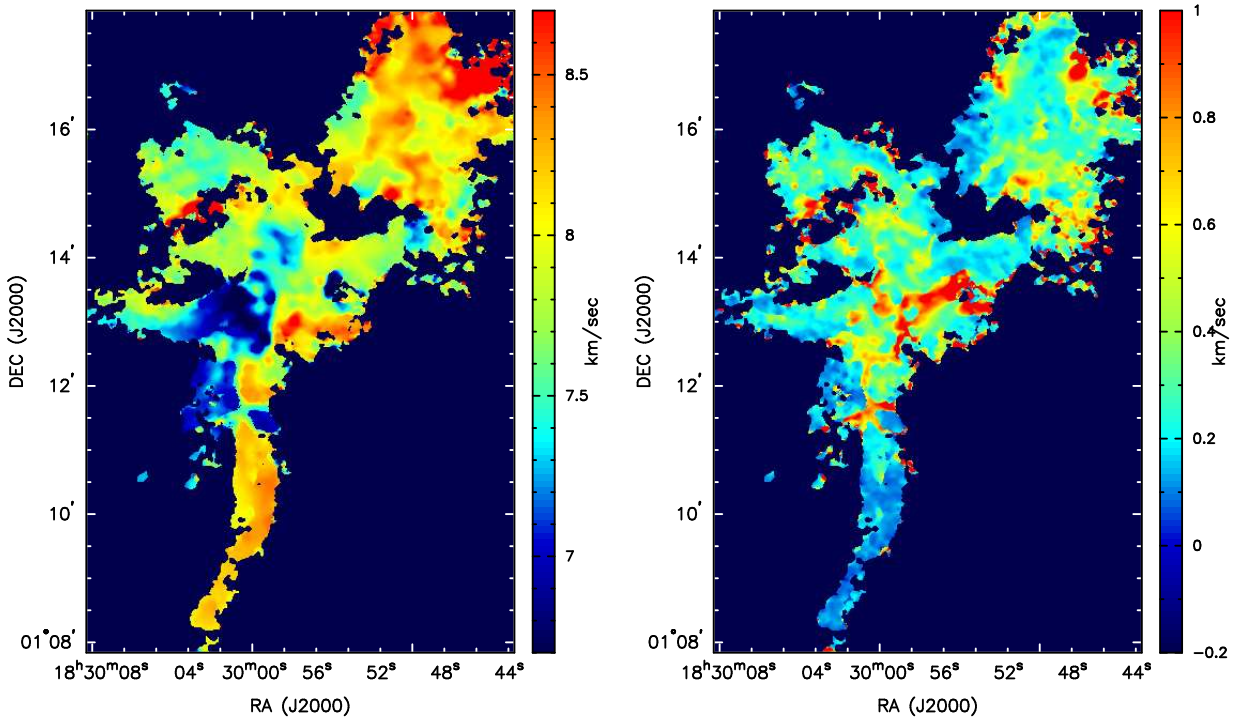

Figure 5.3: The velocity centroid map (left panel) and velocity dispersion map (right panel) in Serpens Main. The maps are obtained from the fitting to the strongest N_2H^+(1-0) line.

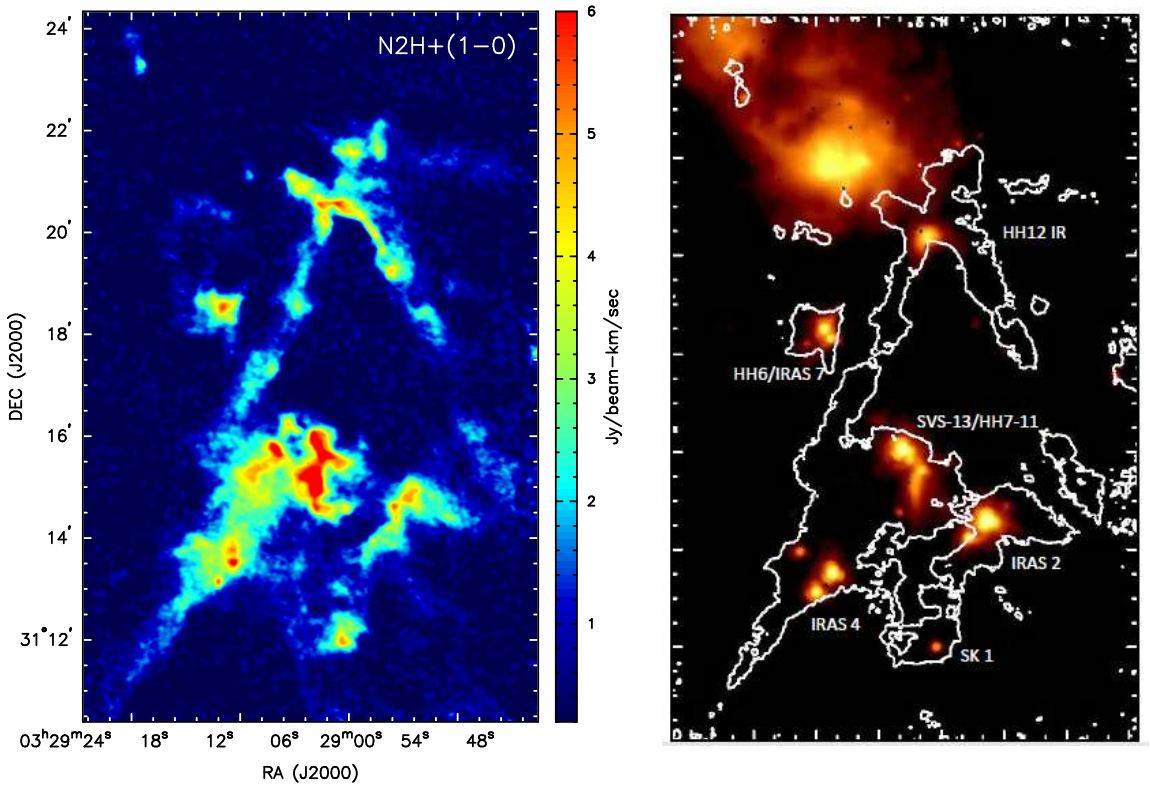

Figure 5.4: *Left panel*: The integrated intensity map of N_2H^+(1-0) in NGC 1333. The image is mapped using the strongest hyperfine line with a velocity range of 9.23 km s^{-1} to 2.95 km s^{-1}. *Right panel*: The 1.5 Jy $beam^{-1}$ km s^{-1} emission from the N_2H^+(1-0) emission overlaid on the *Herschel* 100 μm image. The image is from Mundy et al. (2013).

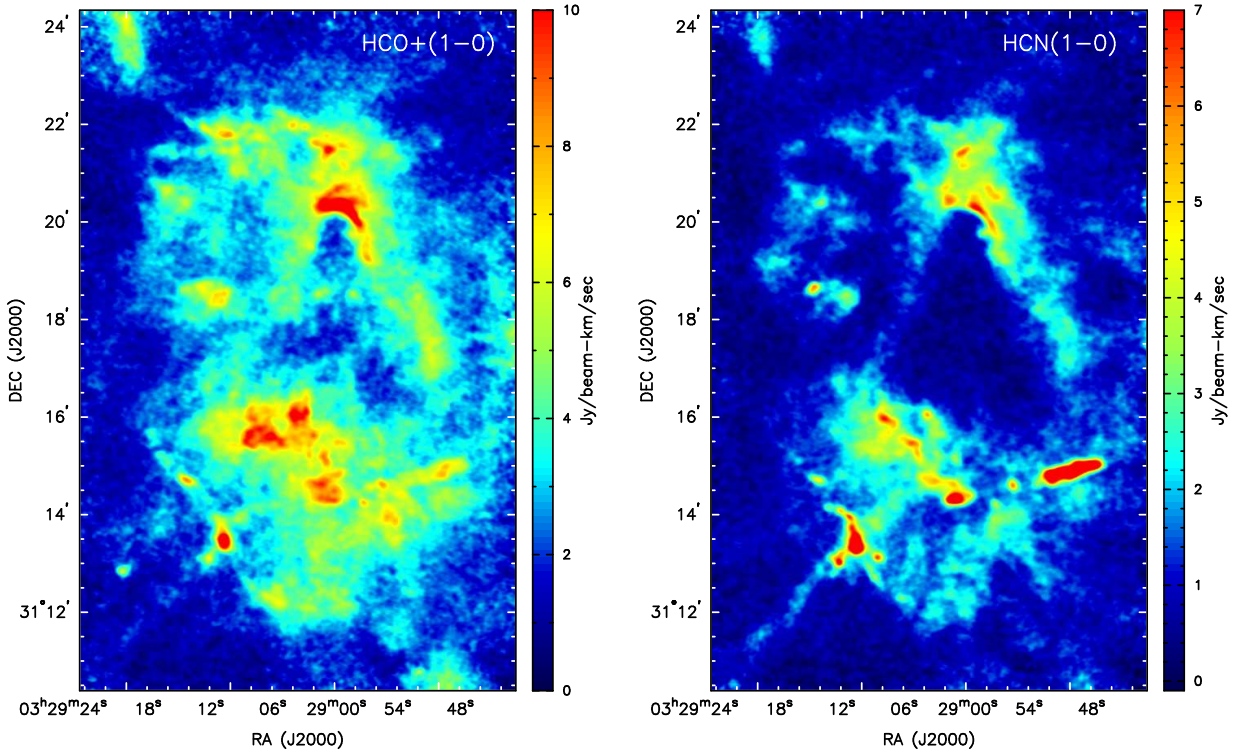

Figure 5.5: The integrated intensity maps of HCO^+(1-0) (left panel) and HCN(1-0) (right panel) in NGC 1333. The maps are generated in a velocity range of 13.63 km s^{-1} to -0.20 km s^{-1} for HCO^+(1-0) and 10.49 km s^{-1} to 4.20 km s^{-1} for HCN(1-0).

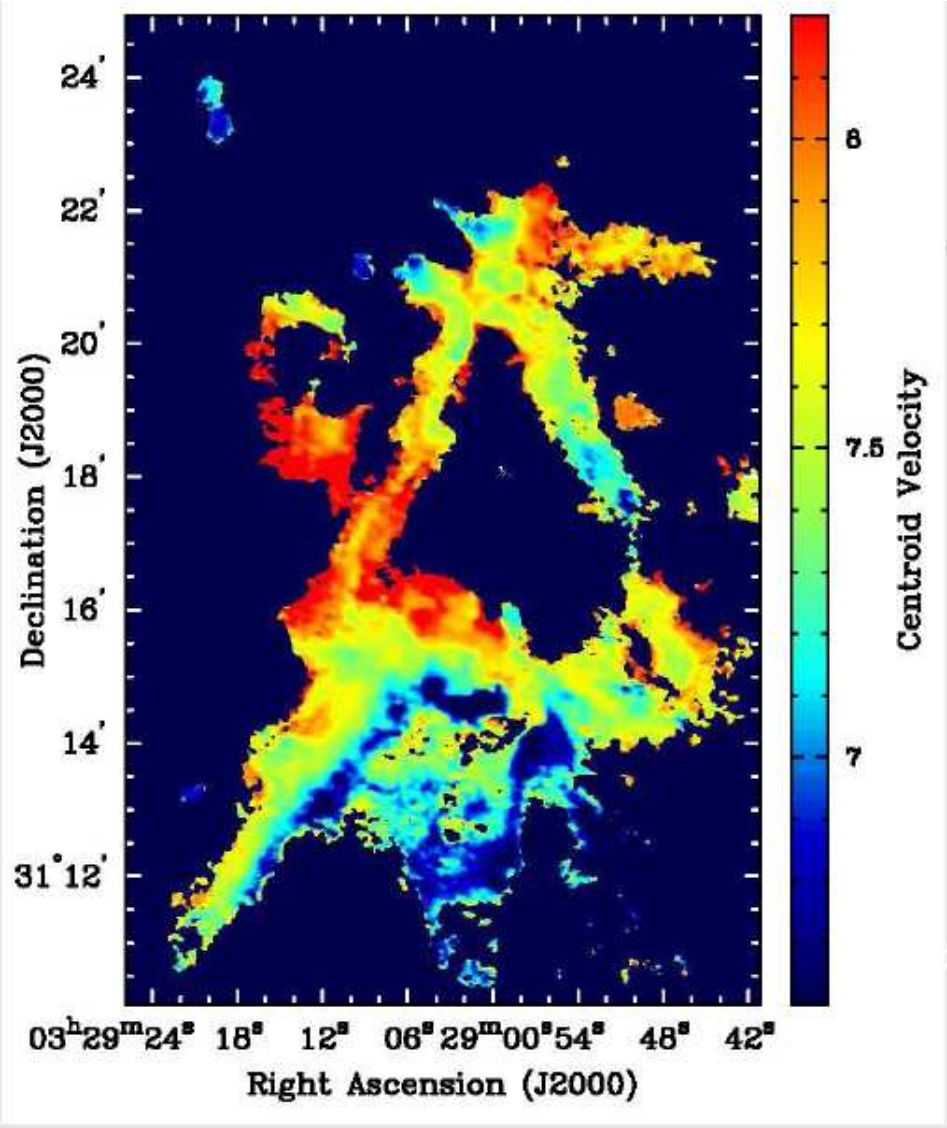

Figure 5.6: The velocity centroid map in NGC 1333 (Mundy et al., 2013). The maps are obtained from the fitting to the strongest N_2H^+(1-0) line.

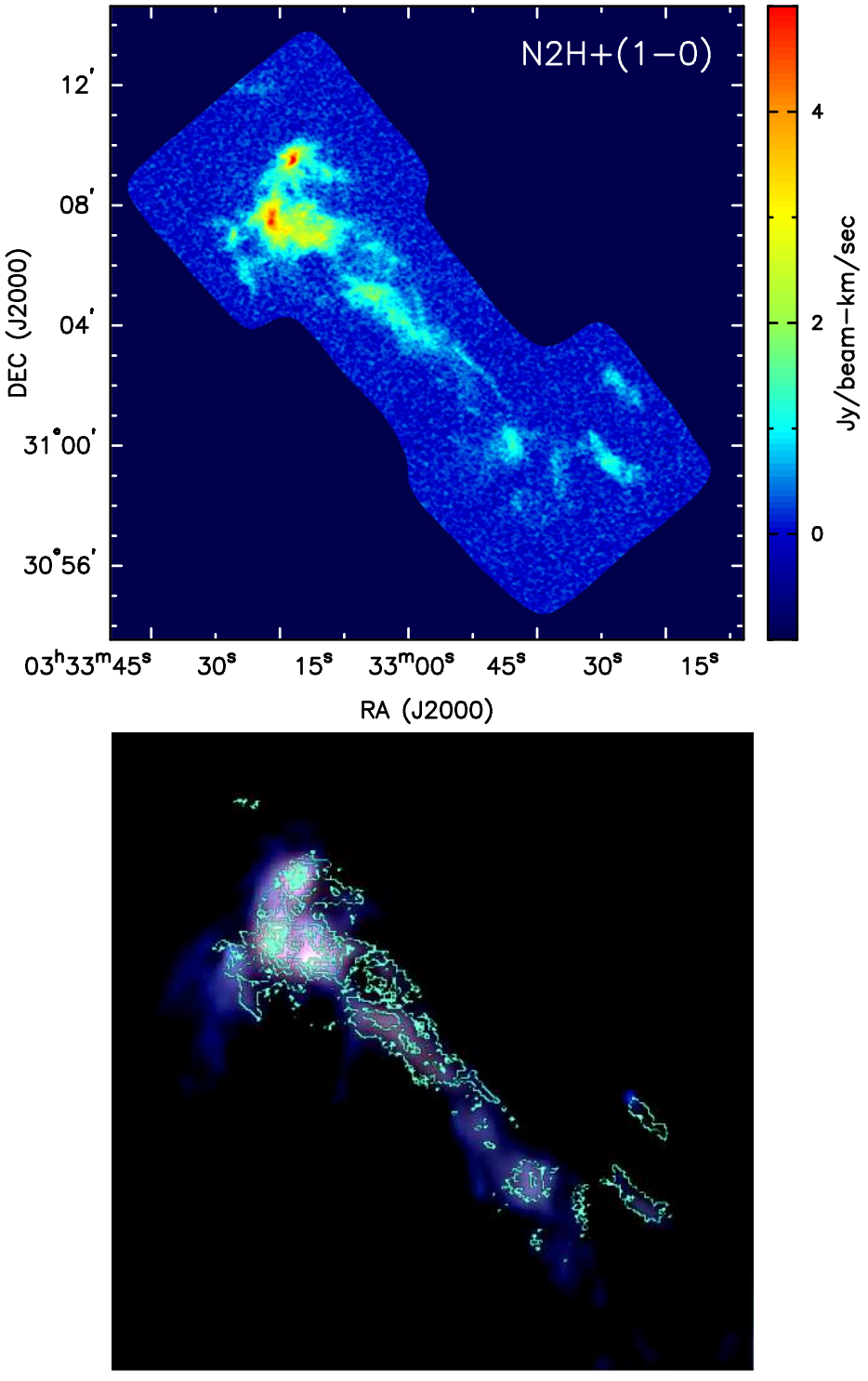

Figure 5.7: *Upper panel*: The integrated intensity map of N_2H^+(1-0) in B1. The image is mapped using the strongest hyperfine line with a velocity range of 8.86 km s^{-1} to 4.15 km s^{-1}. *Bottom panel*: The *Herschel* 350 μm image with the N_2H^+(1-0) emission overlaid from Storm et al. (2013).

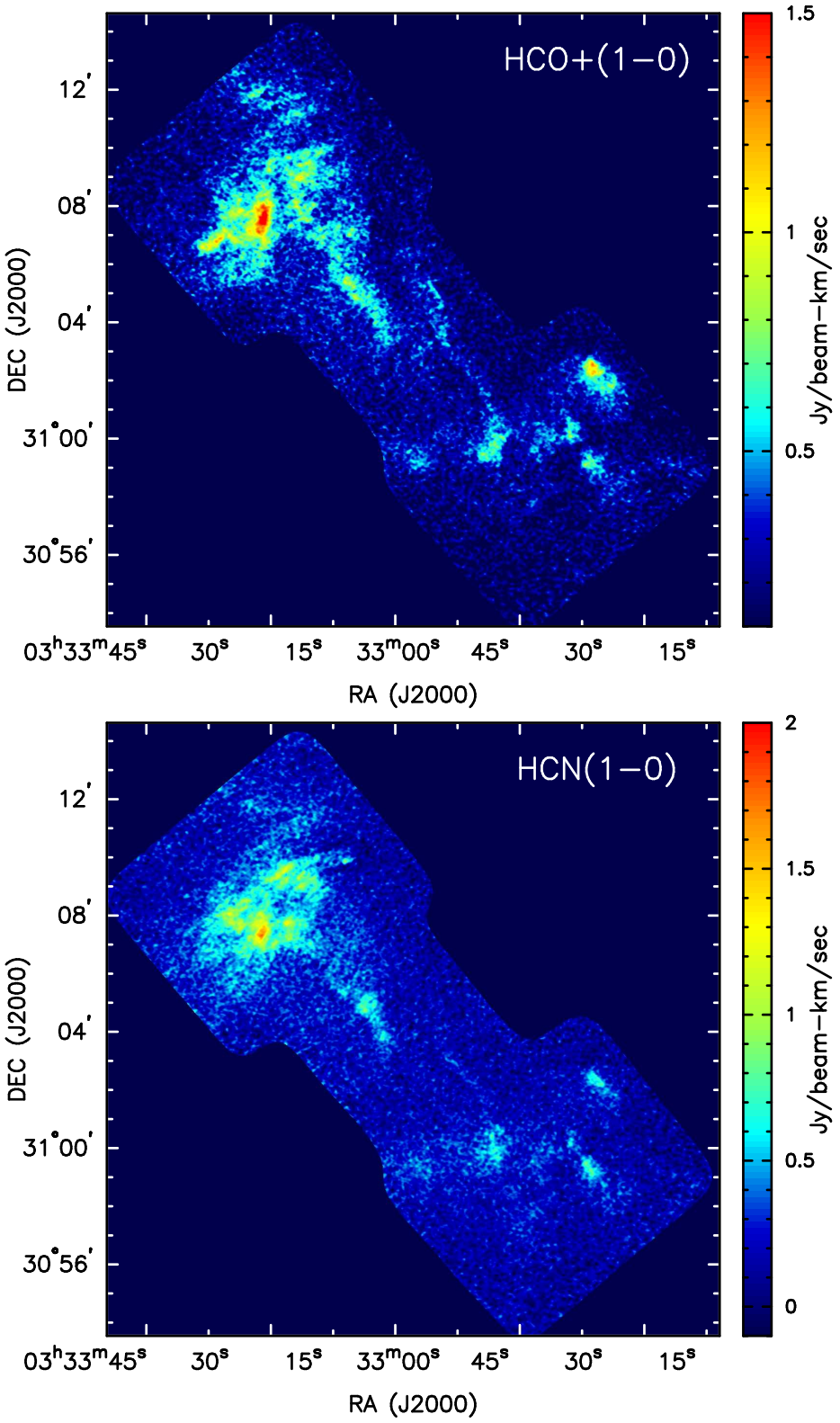

Figure 5.8: The integrated intensity maps of HCO^+(1-0) (upper panel) and HCN(1-0) (bottom panel) in B1. The maps are generated in a velocity range of 7.76 km s^{-1} to 5.56 km s^{-1} for both molecular lines.

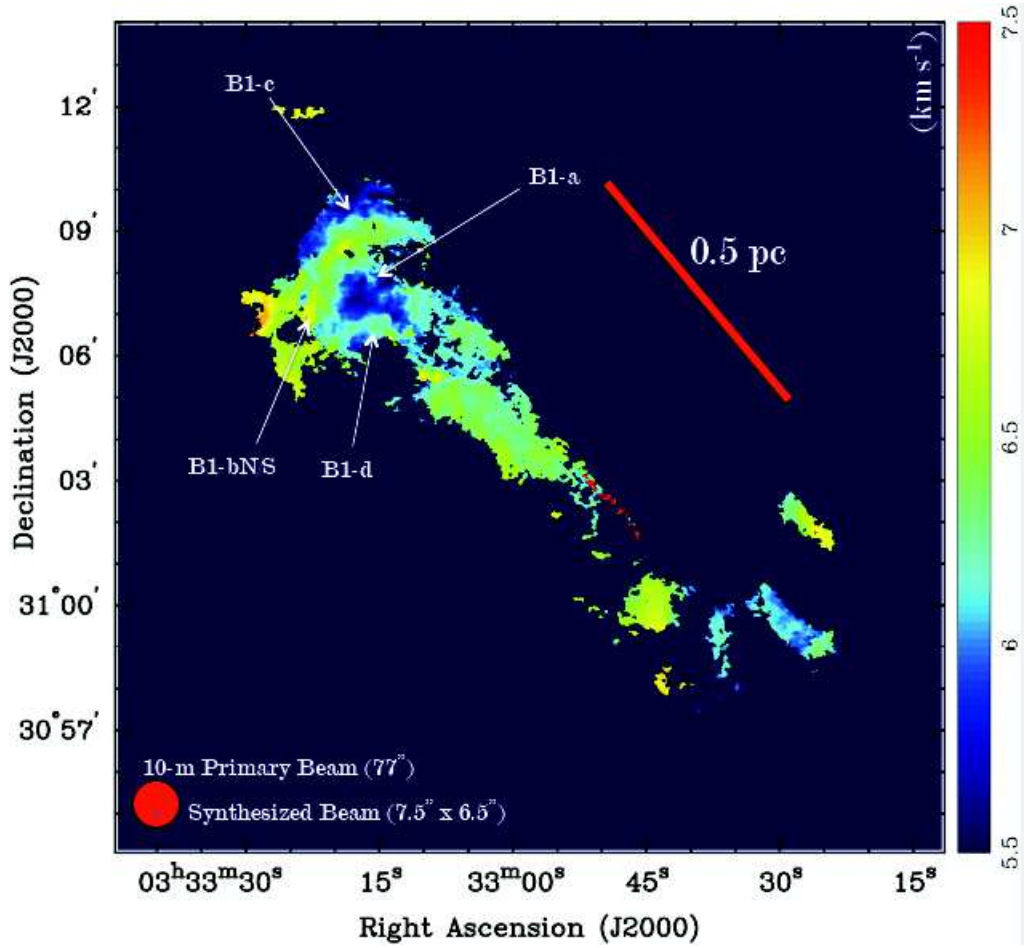

Figure 5.9: The velocity centroid map in B1 (Storm et al., 2013) with submillimeter cores B1-a, B1-b, B1-c, and B1-d indicated in the map. The maps are obtained from the fitting to the strongest N_2H^+(1-0) line.

Chapter 6

Conclusions

In this thesis, the studies of filamentary structures in the prestellar phase, the protocluster IRAS 05345+3157, nine starless cores in Orion, and the CARMA Large Area Star-formation Survey have been presented.

Filamentary structures are ubiquitous from large-scale molecular clouds (few parsecs) to small-scale circumstellar envelopes around Class 0 sources (∼1000 AU to ∼0.1 pc). In particular, recent observations with the *Herschel Space Observatory* emphasize the importance of large-scale filaments (few parsecs) and star formation. The small-scale flattened envelopes around Class 0 sources are reminiscent of the large-scale filaments. In Chapter 2, we propose an observationally derived scenario for filamentary star formation that describes the evolution of filaments as part of the process for formation of cores and circumstellar envelopes. If such a scenario is correct, small-scale filamentary structures (0.1 pc in length) with higher densities embedded in starless cores should exist, although to date almost all the interferometers have failed to observe such structures. We perform synthetic observations of filaments at the prestellar stage by modeling the known Class 0 flattened envelope in L1157 using both the Combined Array for Research in Millimeter-wave Astronomy (CARMA) and the Atacama Large Millimeter/Submillimeter Array (ALMA). We show that with reasonable estimates for the column density through the flattened envelope, the CARMA D-array at 3mm wavelengths is not able to detect such filamentary structure, so previous studies would not have detected them. However, the substructures may be detected with CARMA D+E array at 3 mm and CARMA E array at 1 mm as a result of more appropriate resolution and sensitivity. ALMA is also capable of detecting the substructures and showing the structures in detail compared to the CARMA results with its unprecedented sensitivity. Such detection will confirm the new proposed paradigm of non-spherical star formation.

In Chapter 3, we present observations of the intermediate to massive star-forming region

I05345+3157 using the molecular line tracer CS($2-1$) with CARMA to reveal the properties of the dense gas cores. Seven gas cores are identified in the integrated intensity map of CS($2-1$). Among these, core 1 and core 3 have counterparts in the $\lambda = 2.7$ mm continuum data. We suggest that core 1 and core 3 are star-forming cores that may already or will very soon harbor young massive protostars. The total masses of core 1 estimated from the LTE method and dust emission by assuming a gas-to-dust ratio are 5 ± 1 $M_\odot$ and 18 ± 6 $M_\odot$, and that of core 3 are 15 ± 7 $M_\odot$ and 11 ± 3 $M_\odot$. The spectrum of core 3 shows blue-skewed self-absorption, which suggests gas infall – a collapsing core. The observed broad linewidths of the seven gas cores indicate non-thermal motions. These non-thermal motions can be interactions with nearby outflows or due to the initial turbulence; the former is observed, while the role of initial turbulence is less certain. Finally, the virial masses of the gas cores are larger than the LTE masses, which for a bound core implies a requirement on the external pressure of $\sim 10^8$ K cm^{-3}. The cores have the potential to further form massive stars.

In Chapter 4, we study the structure and kinematics of nine 0.1 pc-scale cores in Orion with the IRAM 30-m telescope and the CARMA D-array using CS(2-1) as the main tracer. The single-dish moment zero maps of the starless cores show single structures, with central column densities ranging from 7 to 42×10^{23} cm^{-2} and LTE masses from 20 $M_\odot$ to 154 $M_\odot$. However, at the higher CARMA resolution ($5''$), all of the cores except one fragment into 3 - 5 components. The number of fragments is small compared to that found in some turbulent fragmentation models, although inclusion of magnetic fields may reduce the predicted fragment number and improve the model agreement. This result demonstrates that hierarchical fragmentation from parsec-scale molecular clouds to sub-parsec cores continues to take place inside the starless cores. The starless cores and their fragments are embedded in larger filamentary structures, which likely played a role in the core formation and fragmentation. Most cores show clear velocity gradients, with magnitudes ranging from 1.7 to 14.3 km s^{-1} pc^{-1}. We modeled one of them in detail, and found that its spectra are best explained by a converging flow along a filament toward the core center; the gradients in other cores may be modelled similarly. We infer a mass inflow rate of $\sim 2 \times 10^{-3}$ $M_\odot$ yr^{-1}, which is in principle high enough to overcome radiation pressure and allow for massive star formation. However, the core contains multiple fragments, and it is unclear whether the inflow would feed the growth of primarily a single massive star or a cluster of lower mass objects. We conclude that fast,

supersonic converging flow along filaments may play an important role in massive star and cluster formation.

In Chapter 5, the first results in Serpens Main, NGC 1333, and B1 from the CARMA Large Area Star-formation Survey (CLASSy) have been presented. These data open an exciting era to study star formation from 1500 AU to 1 pc at millimeter wavelengths. In the future, I plan to continue to work with the CLASSy project, with a specific focus on kinematics from large to small scales to test star formation theories and core formation mechanisms.

References

André, P., Men'shchikov, A., Bontemps, S., Könyves, V., Motte, F., Schneider, N., Didelon, P., Minier, V., Saraceno, P., Ward-Thompson, D., di Francesco, J., White, G., Molinari, S., Testi, L., Abergel, A., Griffin, M., Henning, T., Royer, P., Merín, B., Vavrek, R., Attard, M., Arzoumanian, D., Wilson, C. D., Ade, P., Aussel, H., Baluteau, J.-P., Benedettini, M., Bernard, J.-P., Blommaert, J. A. D. L., Cambrésy, L., Cox, P., di Giorgio, A., Hargrave, P., Hennemann, M., Huang, M., Kirk, J., Krause, O., Launhardt, R., Leeks, S., Le Pennec, J., Li, J. Z., Martin, P. G., Maury, A., Olofsson, G., Omont, A., Peretto, N., Pezzuto, S., Prusti, T., Roussel, H., Russeil, D., Sauvage, M., Sibthorpe, B., Sicilia-Aguilar, A., Spinoglio, L., Waelkens, C., Woodcraft, A., & Zavagno, A. 2010, A&A, 518, L102

Arzoumanian, D., André, P., Didelon, P., Könyves, V., Schneider, N., Men'shchikov, A., Sousbie, T., Zavagno, A., Bontemps, S., di Francesco, J., Griffin, M., Hennemann, M., Hill, T., Kirk, J., Martin, P., Minier, V., Molinari, S., Motte, F., Peretto, N., Pezzuto, S., Spinoglio, L., Ward-Thompson, D., White, G., & Wilson, C. D. 2011, A&A, 529, L6

Aso, Y., Tatematsu, K., Sekimoto, Y., Nakano, T., Umemoto, T., Koyama, K., & Yamamoto, S. 2000, ApJS, 131, 465

Ballesteros-Paredes, J., Hartmann, L., & Vázquez-Semadeni, E. 1999, ApJ, 527, 285

Bally, J., Lanber, W. D., Stark, A. A., & Wilson, R. W. 1987, ApJL, 312, L45

Basu, S. & Mouschovias, T. C. 1995, ApJ, 453, 271

Bate, M. R. & Bonnell, I. A. 2005, MNRAS, 356, 1201

Belloche, A., André, P., Despois, D., & Blinder, S. 2002, A&A, 393, 927

Benjamin, R. A., Churchwell, E., Babler, B. L., Bania, T. M., Clemens, D. P., Cohen, M., Dickey, J. M., Indebetouw, R., Jackson, J. M., Kobulnicky, H. A., Lazarian, A., Marston, A. P., Mathis, J. S., Meade, M. R., Seager, S., Stolovy, S. R., Watson, C., Whitney, B. A., Wolff, M. J., & Wolfire, M. G. 2003, PASP, 115, 953

Bergin, E. A., Alves, J., Huard, T., & Lada, C. J. 2002, ApJL, 570, L101

Beuther, H., Churchwell, E. B., McKee, C. F., & Tan, J. C. 2007a, in Protostars and Planets V, ed. B. Reipurth, D. Jewitt, & K. Keil, 165–180

Beuther, H., Leurini, S., Schilke, P., Wyrowski, F., Menten, K. M., & Zhang, Q. 2007b, A&A, 466, 1065

Beuther, H., Schilke, P., Menten, K. M., Motte, F., Sridharan, T. K., & Wyrowski, F. 2002, ApJ, 566, 945

Blitz, L. & Shu, F. H. 1980, ApJ, 238, 148

Bonnell, I. A. & Bate, M. R. 2006, MNRAS, 370, 488

Bonnell, I. A., Bate, M. R., Clarke, C. J., & Pringle, J. E. 2001, MNRAS, 323, 785

Bonnell, I. A., Vine, S. G., & Bate, M. R. 2004, MNRAS, 349, 735

Bontemps, S., Motte, F., Csengeri, T., & Schneider, N. 2010, A&A, 524, A18

Bourke, T. L., Myers, P. C., Caselli, P., Di Francesco, J., Belloche, A., Plume, R., & Wilner, D. J. 2012, ApJ, 745, 117

Brinch, C. & Hogerheijde, M. R. 2010, A&A, 523, A25

Buckle, J. V., Curtis, E. I., Roberts, J. F., White, G. J., Hatchell, J., Brunt, C., Butner, H. M., Cavanagh, B., Chrysostomou, A., Davis, C. J., Duarte-Cabral, A., Etxaluze, M., di Francesco, J., Friberg, P., Friesen, R., Fuller, G. A., Graves, S., Greaves, J. S., Hogerheijde, M. R., Johnstone, D., Matthews, B., Matthews, H., Nutter, D., Rawlings, J. M. C., Richer, J. S., Sadavoy, S., Simpson, R. J., Tothill, N. F. H., Tsamis, Y. G., Viti, S., Ward-Thompson, D., Wouterloot, J. G. A., & Yates, J. 2010, MNRAS, 401, 204

Buckle, J. V., Davis, C. J., Francesco, J. D., Graves, S. F., Nutter, D., Richer, J. S., Roberts, J. F., Ward-Thompson, D., White, G. J., Brunt, C., Butner, H. M., Cavanagh, B., Chrysostomou, A., Curtis, E. I., Duarte-Cabral, A., Etxaluze, M., Fich, M., Friberg, P., Friesen, R., Fuller, G. A., Greaves, J. S., Hatchell, J., Hogerheijde, M. R., Johnstone, D., Matthews, B., Matthews, H., Rawlings, J. M. C., Sadavoy, S., Simpson, R. J., Tothill, N. F. H., Tsamis, Y. G., Viti, S., Wouterloot, J. G. A., & Yates, J. 2012, MNRAS, 422, 521

Butler, M. J. & Tan, J. C. 2009, ApJ, 696, 484

Carey, S. J., Clark, F. O., Egan, M. P., Price, S. D., Shipman, R. F., & Kuchar, T. A. 1998, ApJ, 508, 721

Carey, S. J., Feldman, P. A., Redman, R. O., Egan, M. P., MacLeod, J. M., & Price, S. D. 2000, ApJL, 543, L157

Caselli, P., Benson, P. J., Myers, P. C., & Tafalla, M. 2002, ApJ, 572, 238

Caulet, A., Gruendl, R. A., & Chu, Y.-H. 2008, ApJ, 678, 200

Cesaroni, R., Olmi, L., Walmsley, C. M., Churchwell, E., & Hofner, P. 1994, ApJL, 435, L137

Cesaroni, R., Walmsley, C. M., Koempe, C., & Churchwell, E. 1991, A&A, 252, 278

Chiang, H.-F., Looney, L. W., & Tobin, J. J. 2012, ApJ, 756, 168

Chiang, H.-F., Looney, L. W., Tobin, J. J., & Hartmann, L. 2010, ApJ, 709, 470

Chini, R., Reipurth, B., Ward-Thompson, D., Bally, J., Nyman, L.-A., Sievers, A., & Billawala, Y. 1997, ApJL, 474, L135

Choi, M., Evans, II, N. J., Gregersen, E. M., & Wang, Y. 1995, ApJ, 448, 742

Churchwell, E., Walmsley, C. M., & Cesaroni, R. 1990, A&A Supp., 83, 119

Commerçon, B., Hennebelle, P., & Henning, T. 2011, ApJL, 742, L9

Crutcher, R. M. 2012, ARA&A, 50, 29

Csengeri, T., Bontemps, S., Schneider, N., Motte, F., & Dib, S. 2011a, A&A, 527, A135

Csengeri, T., Bontemps, S., Schneider, N., Motte, F., Gueth, F., & Hora, J. L. 2011b, ApJL, 740, L5

Curry, C. L. 2002, ApJ, 576, 849

Curtis, E. I. & Richer, J. S. 2011, MNRAS, 410, 75

Curtis, E. I., Richer, J. S., Swift, J. J., & Williams, J. P. 2010, MNRAS, 408, 1516

Davis, C. J., Matthews, H. E., Ray, T. P., Dent, W. R. F., & Richer, J. S. 1999, MNRAS, 309, 141

Di Francesco, J., Johnstone, D., Kirk, H., MacKenzie, T., & Ledwosinska, E. 2008, ApJS, 175, 277

Dobbs, C. L., Bonnell, I. A., & Clark, P. C. 2005, MNRAS, 360, 2

Duarte-Cabral, A., Dobbs, C. L., Peretto, N., & Fuller, G. A. 2011, A&A, 528, A50

Eiroa, C., Djupvik, A. A., & Casali, M. M. 2008, The Serpens Molecular Cloud, ed. B. Reipurth, 693

Elmegreen, B. G. 2000, ApJ, 530, 277

Enoch, M. L., Glenn, J., Evans, II, N. J., Sargent, A. I., Young, K. E., & Huard, T. L. 2007, ApJ, 666, 982

Enoch, M. L., Lee, J.-E., Harvey, P., Dunham, M. M., & Schnee, S. 2010, ApJL, 722, L33

Enoch, M. L., Young, K. E., Glenn, J., Evans, II, N. J., Golwala, S., Sargent, A. I., Harvey, P., Aguirre, J., Goldin, A., Haig, D., Huard, T. L., Lange, A., Laurent, G., Maloney, P., Mauskopf, P., Rossinot, P., & Sayers, J. 2006, ApJ, 638, 293

Evans, II, N. J. 1999, ARA&A, 37, 311

Evans, II, N. J., Allen, L. E., Blake, G. A., Boogert, A. C. A., Bourke, T., Harvey, P. M., Kessler, J. E., Koerner, D. W., Lee, C. W., Mundy, L. G., Myers, P. C., Padgett, D. L., Pontoppidan, K., Sargent, A. I., Stapelfeldt, K. R., van Dishoeck, E. F., Young, C. H., & Young, K. E. 2003, PASP, 115, 965

Evans, II, N. J., Dunham, M. M., Jørgensen, J. K., Enoch, M. L., Merín, B., van Dishoeck, E. F., Alcalá, J. M., Myers, P. C., Stapelfeldt, K. R., Huard, T. L., Allen, L. E., Harvey, P. M., van Kempen, T., Blake, G. A., Koerner, D. W., Mundy, L. G., Padgett, D. L., & Sargent, A. I. 2009, ApJS, 181, 321

Fazio, G. G., Hora, J. L., Allen, L. E., Ashby, M. L. N., Barmby, P., Deutsch, L. K., Huang, J.-S., Kleiner, S., Marengo, M., Megeath, S. T., Melnick, G. J., Pahre, M. A., Patten, B. M., Polizotti, J., Smith, H. A., Taylor, R. S., Wang, Z., Willner, S. P., Hoffmann, W. F., Pipher, J. L., Forrest, W. J., McMurty, C. W., McCreight, C. R., McKelvey, M. E., McMurray, R. E., Koch, D. G., Moseley, S. H., Arendt, R. G., Mentzell, J. E., Marx, C. T., Losch, P., Mayman, P., Eichhorn, W., Krebs, D., Jhabvala, M., Gezari, D. Y., Fixsen, D. J., Flores, J., Shakoorzadeh, K., Jungo, R., Hakun, C., Workman, L., Karpati, G., Kichak, R., Whitley, R., Mann, S., Tollestrup, E. V., Eisenhardt, P., Stern, D., Gorjian, V., Bhattacharya, B., Carey, S., Nelson, B. O., Glaccum, W. J., Lacy, M., Lowrance, P. J., Laine, S., Reach, W. T., Stauffer, J. A., Surace, J. A., Wilson, G., Wright, E. L., Hoffman, A., Domingo, G., & Cohen, M. 2004, ApJS, 154, 10

Fontani, F., Caselli, P., Bourke, T. L., Cesaroni, R., & Brand, J. 2008, A&A, 477, L45

Fontani, F., Zhang, Q., Caselli, P., & Bourke, T. L. 2009, A&A, 499, 233

Frau, P., Girart, J. M., Beltrán, M. T., Morata, O., Masqué, J. M., Busquet, G., Alves, F. O., Sánchez-Monge, Á., Estalella, R., & Franco, G. A. P. 2010, ApJ, 723, 1665

Galli, D. & Shu, F. H. 1993, ApJ, 417, 243

Garay, G., Brooks, K. J., Mardones, D., & Norris, R. P. 2003, ApJ, 587, 739

Garay, G., Faúndez, S., Mardones, D., Bronfman, L., Chini, R., & Nyman, L.-Å. 2004, ApJ, 610, 313

Goldsmith, P. F. & Langer, W. D. 1999, ApJ, 517, 209

Gong, H. & Ostriker, E. C. 2011, ApJ, 729, 120

Goodman, A. A., Benson, P. J., Fuller, G. A., & Myers, P. C. 1993, ApJ, 406, 528

Goodman, A. A., Crutcher, R. M., Heiles, C., Myers, P. C., & Troland, T. H. 1989, ApJL, 338, L61

Graves, S. F., Richer, J. S., Buckle, J. V., Duarte-Cabral, A., Fuller, G. A., Hogerheijde, M. R., Owen, J. E., Brunt, C., Butner, H. M., Cavanagh, B., Chrysostomou, A., Curtis, E. I., Davis, C. J., Etxaluze, M., Francesco, J. D., Friberg, P., Friesen, R. K., Greaves, J. S., Hatchell, J., Johnstone, D., Matthews, B., Matthews, H., Matzner, C. D., Nutter, D., Rawlings, J. M. C., Roberts, J. F., Sadavoy, S., Simpson, R. J., Tothill, N. F. H., Tsamis, Y. G., Viti, S., Ward-Thompson, D., White, G. J., Wouterloot, J. G. A., & Yates, J. 2010, MNRAS, 409, 1412

Gregersen, E. M., Evans, II, N. J., Zhou, S., & Choi, M. 1997, ApJ, 484, 256

Gutermuth, R. A., Bourke, T. L., Allen, L. E., Myers, P. C., Megeath, S. T., Matthews, B. C., Jørgensen, J. K., Di Francesco, J., Ward-Thompson, D., Huard, T. L., Brooke, T. Y., Dunham, M. M., Cieza, L. A., Harvey, P. M., & Chapman, N. L. 2008, ApJL, 673, L151

Hacar, A. & Tafalla, M. 2011, A&A, 533, A34

Hartmann, L. 2002, ApJ, 578, 914

Harvey, D. W. A., Wilner, D. J., Myers, P. C., & Tafalla, M. 2003, ApJ, 596, 383

Harvey, P. M., Chapman, N., Lai, S.-P., Evans, II, N. J., Allen, L. E., Jørgensen, J. K., Mundy, L. G., Huard, T. L., Porras, A., Cieza, L., Myers, P. C., Merín, B., van Dishoeck, E. F., Young, K. E., Spiesman, W., Blake, G. A., Koerner, D. W., Padgett, D. L., Sargent, A. I., & Stapelfeldt, K. R. 2006, ApJ, 644, 307

Harvey, P. M., Rebull, L. M., Brooke, T., Spiesman, W. J., Chapman, N., Huard, T. L., Evans, II, N. J., Cieza, L., Lai, S.-P., Allen, L. E., Mundy, L. G., Padgett, D. L., Sargent, A. I., Stapelfeldt, K. R., Myers, P. C., van Dishoeck, E. F., Blake, G. A., & Koerner, D. W. 2007, ApJ, 663, 1139

Hatchell, J., Richer, J. S., Fuller, G. A., Qualtrough, C. J., Ladd, E. F., & Chandler, C. J. 2005, A&A, 440, 151

Hatchell, J., Thompson, M. A., Millar, T. J., & MacDonald, G. H. 1998, A&A Supp., 133, 29

Heitsch, F., Hartmann, L. W., Slyz, A. D., Devriendt, J. E. G., & Burkert, A. 2008, ApJ, 674, 316

Hennebelle, P., Commerçon, B., Joos, M., Klessen, R. S., Krumholz, M., Tan, J. C., & Teyssier, R. 2011, A&A, 528, A72

Hennebelle, P. & Falgarone, E. 2012, A&ARv, 20, 55

Henning, T., Cesaroni, R., Walmsley, M., & Pfau, W. 1992, A&A Supp., 93, 525

Hill, T., Motte, F., Didelon, P., Bontemps, S., Minier, V., Hennemann, M., Schneider, N., André, P., Men'Shchikov, A., Anderson, L. D., Arzoumanian, D., Bernard, J.-P., di Francesco, J., Elia, D., Giannini, T., Griffin, M. J., Könyves, V., Kirk, J., Marston, A. P., Martin, P. G., Molinari, S., Nguyn Lu'O'Ng, Q., Peretto, N., Pezzuto, S., Roussel, H., Sauvage, M., Sousbie, T., Testi, L., Ward-Thompson, D., White, G. J., Wilson, C. D., & Zavagno, A. 2011, A&A, 533, A94

Hillenbrand, L. A. 1997, AJ, 113, 1733

Hillenbrand, L. A. & Hartmann, L. W. 1998, ApJ, 492, 540

Hiramatsu, M., Hirano, N., & Takakuwa, S. 2010, ApJ, 712, 778

Houde, M., Dowell, C. D., Hildebrand, R. H., Dotson, J. L., Vaillancourt, J. E., Phillips, T. G., Peng, R., & Bastien, P. 2004, ApJ, 604, 717

Hunter, T. R., Phillips, T. G., & Menten, K. M. 1997, ApJ, 478, 283

Hunter, T. R., Zhang, Q., & Sridharan, T. K. 2004, ApJ, 606, 929

Ikeda, N., Sunada, K., & Kitamura, Y. 2007, ApJ, 665, 1194

Inutsuka, S.-I. & Miyama, S. M. 1997, ApJ, 480, 681

Jappsen, A.-K., Klessen, R. S., Larson, R. B., Li, Y., & Mac Low, M.-M. 2005, A&A, 435, 611

Jijina, J. & Adams, F. C. 1996, ApJ, 462, 874

Johnstone, D. & Bally, J. 1999, ApJL, 510, L49

Jones, C. E. & Basu, S. 2002, ApJ, 569, 280

Jørgensen, J. K., Harvey, P. M., Evans, II, N. J., Huard, T. L., Allen, L. E., Porras, A., Blake, G. A., Bourke, T. L., Chapman, N., Cieza, L., Koerner, D. W., Lai, S.-P., Mundy, L. G., Myers, P. C., Padgett, D. L., Rebull, L., Sargent, A. I., Spiesman, W., Stapelfeldt, K. R., van Dishoeck, E. F., Wahhaj, Z., & Young, K. E. 2006, ApJ, 645, 1246

Jørgensen, J. K., van Dishoeck, E. F., Visser, R., Bourke, T. L., Wilner, D. J., Lommen, D., Hogerheijde, M. R., & Myers, P. C. 2009, A&A, 507, 861

Kameya, O., Hasegawa, T. I., Hirano, N., Tosa, M., Taniguchi, Y., Takakubo, K., & Seki, M. 1986, PASJ, 38, 793

Keene, J. & Masson, C. R. 1990, ApJ, 355, 635

Kenyon, S. J., Gómez, M., & Whitney, B. A. 2008, Low Mass Star Formation in the Taurus-Auriga Clouds, ed. Reipurth, B., 405

Keto, E. & Field, G. 2005, ApJ, 635, 1151

Kirk, H., Myers, P. C., Bourke, T. L., Gutermuth, R. A., Hedden, A., & Wilson, G. W. 2013, ArXiv e-prints

Kirk, J. M., Ward-Thompson, D., Di Francesco, J., Bourke, T. L., Evans, II, N. J., Merín, B., Allen, L. E., Cieza, L. A., Dunham, M. M., Harvey, P., Huard, T., Jørgensen, J. K., Miller, J. F., Noriega-Crespo, A., Peterson, D., Ray, T. P., & Rebull, L. M. 2009, ApJS, 185, 198

Klein, R., Lee, K. I., Looney, L. W., & Wang, S. 2011, in preparation

Klein, R., Posselt, B., Schreyer, K., Forbrich, J., & Henning, T. 2005, ApJS, 161, 361

Klessen, R. S., Ballesteros-Paredes, J., Vázquez-Semadeni, E., & Durán-Rojas, C. 2005, ApJ, 620, 786

Kroupa, P. 2001, MNRAS, 322, 231

Krumholz, M. R., Klein, R. I., & McKee, C. F. 2005a, in IAU Symposium, Vol. 227, Massive Star Birth: A Crossroads of Astrophysics, ed. R. Cesaroni, M. Felli, E. Churchwell, & M. Walmsley, 231–236

Krumholz, M. R., Klein, R. I., & McKee, C. F. 2007, ApJ, 656, 959

Krumholz, M. R. & McKee, C. F. 2008, Nature, 451, 1082

Krumholz, M. R., McKee, C. F., & Klein, R. I. 2005b, ApJL, 618, L33

Kun, M. 1998, ApJS, 115, 59

Lada, C. J., Alves, J., & Lada, E. A. 1996, AJ, 111, 1964

Lada, C. J. & Lada, E. A. 2003, ARA&A, 41, 57

Ladd, E. F., Lada, E. A., & Myers, P. C. 1993, ApJ, 410, 168

Ladd, E. F., Myers, P. C., & Goodman, A. A. 1994, ApJ, 433, 117

Larson, R. B. 1981, MNRAS, 194, 809

Lee, C. W., Myers, P. C., & Plume, R. 2004, ApJS, 153, 523

Lee, C. W., Myers, P. C., & Tafalla, M. 1999, ApJ, 526, 788

Lee, K., Looney, L., Johnstone, D., & Tobin, J. 2012, ApJ, 761, 171

Lee, K. I., Looney, L. W., Klein, R., & Wang, S. 2011, MNRAS, 415, 2790

Lis, D. C. & Schilke, P. 2003, ApJL, 597, L145

Liu, H. B., Jiménez-Serra, I., Ho, P. T. P., Chen, H.-R., Zhang, Q., & Li, Z.-Y. 2012, ApJ, 756, 10

Loinard, L., Mioduszewski, A. J., Torres, R. M., Dzib, S., Rodríguez, L. F., & Boden, A. F. 2011, in Revista Mexicana de Astronomia y Astrofisica Conference Series, Vol. 40, Revista Mexicana de Astronomia y Astrofisica Conference Series, 205–210

Lombardi, M., Alves, J., & Lada, C. J. 2006, A&A, 454, 781

Looney, L., Lee, K., Fernandez Lopez, M., Arce, H. G., Chen, C., Crutcher, R., Gong, H., Hakobian, N., Isella, A., Kauffmann, J., Kwon, W., Mouschovias, T. C., Mundy, L. G., Ostriker, E. C., Plunkett, A., Pound, M. W., Rosolowsky, E., Salter, D. M., Shirley, Y. L., Storm, S., Tassis, K., Testi, L., Tobin, J. J., Teuben, P. J., & Volgenau, N. H. 2013, in American Astronomical Society Meeting Abstracts, Vol. 221, American Astronomical Society Meeting Abstracts, 251.11

Looney, L. W., Mundy, L. G., & Welch, W. J. 2000, ApJ, 529, 477

—. 2003a, ApJ, 592, 255

—. 2003b, ApJ, 592, 255

Looney, L. W., Tobin, J. J., & Kwon, W. 2007, ApJL, 670, L131

Mac Low, M.-M. & Klessen, R. S. 2004, Reviews of Modern Physics, 76, 125

Markwardt, C. B. 2009, in Astronomical Society of the Pacific Conference Series, Vol. 411, Astronomical Data Analysis Software and Systems XVIII, ed. D. A. Bohlender, D. Durand, & P. Dowler, 251

Matthews, B. C. & Wilson, C. D. 2002, ApJ, 574, 822

McKee, C. F. & Ostriker, E. C. 2007, ARA&A, 45, 565

McKee, C. F. & Tan, J. C. 2003, ApJ, 585, 850

Mehringer, D. M. 1995, ApJ, 454, 782

Men'shchikov, A., André, P., Didelon, P., Könyves, V., Schneider, N., Motte, F., Bontemps, S., Arzoumanian, D., Attard, M., Abergel, A., Baluteau, J.-P., Bernard, J.-P., Cambrésy, L., Cox, P., di Francesco, J., di Giorgio, A. M., Griffin, M., Hargrave, P., Huang, M., Kirk, J., Li, J. Z., Martin, P., Minier, V., Miville-Deschênes, M.-A., Molinari, S., Olofsson, G., Pezzuto, S., Roussel, H., Russeil, D., Saraceno, P., Sauvage, M., Sibthorpe, B., Spinoglio, L., Testi, L., Ward-Thompson, D., White, G., Wilson, C. D., Woodcraft, A., & Zavagno, A. 2010, A&A, 518, L103

Menten, K. M., Reid, M. J., Forbrich, J., & Brunthaler, A. 2007, A&A, 474, 515

Miao, Y., Mehringer, D. M., Kuan, Y.-J., & Snyder, L. E. 1995, ApJL, 445, L59

Mizuno, A., Onishi, T., Yonekura, Y., Nagahama, T., Ogawa, H., & Fukui, Y. 1995, ApJL, 445, L161

Molinari, S., Testi, L., Brand, J., Cesaroni, R., & Palla, F. 1998, ApJL, 505, L39

Molinari, S., Testi, L., Rodríguez, L. F., & Zhang, Q. 2002, ApJ, 570, 758

Morata, O., Girart, J. M., & Estalella, R. 2003, A&A, 397, 181

—. 2005, A&A, 435, 113

Morata, O., Girart, J. M., Estalella, R., & Garrod, R. T. 2012, MNRAS, 425, 1980

Motte, F. & André, P. 2001, A&A, 365, 440

Mouschovias, T. C. & Spitzer, Jr., L. 1976, ApJ, 210, 326

Mundy, L. G., Storm, S., Pound, M. W., Salter, D. M., Arce, H. G., Chen, C., Crutcher, R., Fernandez Lopez, M., Gong, H., Hakobian, N., Isella, A., Kauffmann, J., Kwon, W., Lee, K., Looney, L., Mouschovias, T. C., Ostriker, E. C., Plunkett, A., Rosolowsky, E., Shirley, Y. L., Tassis, K., Testi, L., Teuben, P. J., Tobin, J. J., & Volgenau, N. H. 2013, in American Astronomical Society Meeting Abstracts, Vol. 221, American Astronomical Society Meeting Abstracts, 251.12

Myers, A. T., McKee, C. F., Cunningham, A. J., Klein, R. I., & Krumholz, M. R. 2012, ArXiv e-prints

Myers, P. C. 2009, ApJ, 700, 1609

—. 2011, ApJ, 735, 82

Myers, P. C., Fuller, G. A., Goodman, A. A., & Benson, P. J. 1991, ApJ, 376, 561

Nakamura, F. & Li, Z.-Y. 2008, ApJ, 687, 354

Nakamura, F., Takakuwa, S., & Kawabe, R. 2012, ApJL, 758, L25

Naranjo-Romero, R., Zapata, L. A., Vázquez-Semadeni, E., Takahashi, S., Palau, A., & Schilke, P. 2012, ApJ, 757, 58

Nutter, D. & Ward-Thompson, D. 2007, MNRAS, 374, 1413

Onishi, T., Mizuno, A., Kawamura, A., Ogawa, H., & Fukui, Y. 1998, ApJ, 502, 296

Onishi, T., Mizuno, A., Kawamura, A., Tachihara, K., & Fukui, Y. 2002, ApJ, 575, 950

Ossenkopf, V. & Henning, T. 1994, A&A, 291, 943

Padoan, P., Juvela, M., Goodman, A. A., & Nordlund, Å. 2001, ApJ, 553, 227

Padoan, P. & Nordlund, Å. 2002, ApJ, 576, 870

Palau, A., Fuente, A., Girart, J. M., Estalella, R., Ho, P. T. P., Sánchez-Monge, Á., Fontani, F., Busquet, G., Commerçon, B., Hennebelle, P., Boissier, J., Zhang, Q., Cesaroni, R., & Zapata, L. A. 2013, ApJ, 762, 120

Pavlyuchenkov, Y., Wiebe, D., Shustov, B., Henning, T., Launhardt, R., & Semenov, D. 2008, ApJ, 689, 335

Peng, T.-C., Zapata, L. A., Wyrowski, F., Güsten, R., & Menten, K. M. 2012, A&A, 544, L19

Peretto, N., André, P., & Belloche, A. 2006, A&A, 445, 979

Pillai, T., Kauffmann, J., Wyrowski, F., Hatchell, J., Gibb, A. G., & Thompson, M. A. 2011, A&A, 530, A118

Pineda, J. E., Goodman, A. A., Arce, H. G., Caselli, P., Longmore, S., & Corder, S. 2011, ApJL, 739, L2

Pirogov, L., Zinchenko, I., Caselli, P., & Johansson, L. E. B. 2007, A&A, 461, 523

Pon, A., Johnstone, D., & Heitsch, F. 2011, ApJ, 740, 88

Pon, A., Toalá, J. A., Johnstone, D., Vázquez-Semadeni, E., Heitsch, F., & Gómez, G. C. 2012, ApJ, 756, 145

Rathborne, J. M., Jackson, J. M., & Simon, R. 2006, ApJ, 641, 389

Robitaille, T. P., Whitney, B. A., Indebetouw, R., Wood, K., & Denzmore, P. 2006, ApJS, 167, 256

Rohlfs, K. & Wilson, T. L. 2000, Tools of radio astronomy

Rygl, K. L. J., Wyrowski, F., Schuller, F., & Menten, K. M. 2013, A&A, 549, A5

Sadavoy, S. I., Di Francesco, J., Bontemps, S., Megeath, S. T., Rebull, L. M., Allgaier, E., Carey, S., Gutermuth, R., Hora, J., Huard, T., McCabe, C.-E., Muzerolle, J., Noriega-Crespo, A., Padgett, D., & Terebey, S. 2010, ApJ, 710, 1247

Saito, H., Saito, M., Moriguchi, Y., & Fukui, Y. 2006, PASJ, 58, 343

Sault, R. J., Teuben, P. J., & Wright, M. C. H. 1995, in Astronomical Society of the Pacific Conference Series, Vol. 77, Astronomical Data Analysis Software and Systems IV, ed. R. A. Shaw, H. E. Payne, & J. J. E. Hayes, 433–+

Schnee, S., Di Francesco, J., Enoch, M., Friesen, R., Johnstone, D., & Sadavoy, S. 2012, ApJ, 745, 18

Schnee, S., Enoch, M., Johnstone, D., Culverhouse, T., Leitch, E., Marrone, D. P., & Sargent, A. 2010, ApJ, 718, 306

Schnee, S., Rosolowsky, E., Foster, J., Enoch, M., & Sargent, A. 2009, ApJ, 691, 1754

Schneider, N., Csengeri, T., Bontemps, S., Motte, F., Simon, R., Hennebelle, P., Federrath, C., & Klessen, R. 2010, A&A, 520, A49

Schneider, S. & Elmegreen, B. G. 1979, ApJS, 41, 87

Schreyer, K., Henning, T., Koempe, C., & Harjunpaeae, P. 1996, A&A, 306, 267

Seale, J. P., Looney, L. W., Chu, Y.-H., Gruendl, R. A., Brandl, B., Chen, C.-H. R., Brandner, W., & Blake, G. A. 2009, ApJ, 699, 150

Shirley, Y. L., Evans, II, N. J., Rawlings, J. M. C., & Gregersen, E. M. 2000, ApJS, 131, 249

Shu, F. H. 1977, ApJ, 214, 488

Simon, R., Jackson, J. M., Rathborne, J. M., & Chambers, E. T. 2006, ApJ, 639, 227

Smith, R. J., Glover, S. C. O., Bonnell, I. A., Clark, P. C., & Klessen, R. S. 2011, MNRAS, 411, 1354

Smith, R. J., Shetty, R., Stutz, A. M., & Klessen, R. S. 2012, ApJ, 750, 64

Sridharan, T. K., Beuther, H., Schilke, P., Menten, K. M., & Wyrowski, F. 2002, ApJ, 566, 931

Stahler, S. W. & Yen, J. J. 2010, MNRAS, 407, 2434

Storm, S., Mundy, L. G., Teuben, P. J., Arce, H. G., Chen, C., Crutcher, R., Fernandez Lopez, M., Gong, H., Hakobian, N., Isella, A., Kauffmann, J., Kwon, W., Lee, K., Looney, L., Mouschovias, T. C., Ostriker, E. C., Plunkett, A., Pound, M. W., Rosolowsky, E., Salter, D. M., Shirley, Y. L., Tassis, K., Testi, L., Tobin, J. J., & Volgenau, N. H. 2013, in American Astronomical Society Meeting Abstracts, Vol. 221, American Astronomical Society Meeting Abstracts, 251.10

Swift, J. J. 2009, ApJ, 705, 1456

Tafalla, M., Mardones, D., Myers, P. C., Caselli, P., Bachiller, R., & Benson, P. J. 1998, ApJ, 504, 900

Tafalla, M., Myers, P. C., Caselli, P., & Walmsley, C. M. 2004, A&A, 416, 191

Tafalla, M., Myers, P. C., Caselli, P., Walmsley, C. M., & Comito, C. 2002, ApJ, 569, 815

Takahashi, S., Saito, M., Ohashi, N., Kusakabe, N., Takakuwa, S., Shimajiri, Y., Tamura, M., & Kawabe, R. 2008, ApJ, 688, 344

Tassis, K. 2007, MNRAS, 379, L50

Tassis, K., Dowell, C. D., Hildebrand, R. H., Kirby, L., & Vaillancourt, J. E. 2009, MNRAS, 399, 1681

Taylor, S. D., Morata, O., & Williams, D. A. 1998, A&A, 336, 309

Terebey, S., Shu, F. H., & Cassen, P. 1984, ApJ, 286, 529

Testi, L. & Sargent, A. I. 1998, ApJL, 508, L91

Tobin, J. J., Hartmann, L., Bergin, E., Chiang, H.-F., Looney, L. W., Chandler, C. J., Maret, S., & Heitsch, F. 2012a, ApJ, 748, 16

Tobin, J. J., Hartmann, L., Bergin, E. A., Chiang, H.-F., Looney, L. W., Chandler, C. J., Maret, S., & Heitsch, F. 2012b, ArXiv e-prints

Tobin, J. J., Hartmann, L., Chiang, H.-F., Looney, L. W., Bergin, E. A., Chandler, C. J., Masqué, J. M., Maret, S., & Heitsch, F. 2011a, ApJ, 740, 45

—. 2011b, ApJ, 740, 45

Tobin, J. J., Hartmann, L., Looney, L. W., & Chiang, H.-F. 2010, ApJ, 712, 1010

Turner, B. E. 1991, ApJS, 76, 617

Urquhart, J. S., Morgan, L. K., Figura, C. C., Moore, T. J. T., Lumsden, S. L., Hoare, M. G., Oudmaijer, R. D., Mottram, J. C., Davies, B., & Dunham, M. K. 2011, MNRAS, 418, 1689

Vasyunina, T., Vasyunin, A. I., Herbst, E., & Linz, H. 2012, ApJ, 751, 105

Walawender, J., Bally, J., Kirk, H., & Johnstone, D. 2005, AJ, 130, 1795

Wang, K., Zhang, Q., Wu, Y., & Zhang, H. 2011, ApJ, 735, 64

Wang, P., Li, Z.-Y., Abel, T., & Nakamura, F. 2010, ApJ, 709, 27

Wang, S., Looney, L. W., Brandner, W., & Close, L. M. 2008, ApJ, 673, 315

Whitney, B. A., Wood, K., Bjorkman, J. E., & Wolff, M. J. 2003, ApJ, 591, 1049

Wilking, B. A., Meyer, M. R., Greene, T. P., Mikhail, A., & Carlson, G. 2004, AJ, 127, 1131

Wright, M. C. H. 2010, in Society of Photo-Optical Instrumentation Engineers (SPIE) Conference Series, Vol. 7733, Society of Photo-Optical Instrumentation Engineers (SPIE) Conference Series

Xue, R. & Wu, Y. 2008, ApJ, 680, 446

Yorke, H. W. & Sonnhalter, C. 2002, ApJ, 569, 846

Zapata, L. A., Schmid-Burgk, J., Ho, P. T. P., Rodríguez, L. F., & Menten, K. M. 2009, ApJL, 704, L45

Zhang, Q., Hunter, T. R., Brand, J., Sridharan, T. K., Cesaroni, R., Molinari, S., Wang, J., & Kramer, M. 2005, ApJ, 625, 864

Zhang, Q., Wang, Y., Pillai, T., & Rathborne, J. 2009, ApJ, 696, 268

Zhou, S., Evans, II, N. J., Koempe, C., & Walmsley, C. M. 1993, ApJ, 404, 232

Zinnecker, H. & Yorke, H. W. 2007, ARA&A, 45, 481